Title

An Experimental Investigation of the Heat Exchanger and Combustion Characteristics of a Fuel-Integrated Energy Recuperative Aircraft Engine

Author

Robertson, Garrett

Publication Date

2022

An Experimental Investigation of the Heat Exchanger and Combustion Characteristics of a Fuel-Integrated Energy Recuperative Aircraft Engine

By

GARRETT ROBERTSON
THESIS

Submitted in partial satisfaction of the requirements for the degree of

MASTER OF SCIENCE

in

Mechanical and Aerospace Engineering

in the

OFFICE OF GRADUATE STUDIES

of the

UNIVERSITY OF CALIFORNIA

DAVIS

Approved:

Paul A. Erickson, Chair

Vinod Narayanan

Benjamin D. Shaw

Committee in Charge

2022

Table of Contents

List of Figures

List of Tables

Abstract

To meet the performance, economic, and environmental goals of the future, aircraft engines need to improve. One way to accomplish this is by enhancing the thermodynamic cycle by using intercooling and/or recuperation such as is employed in the fuel-integrated energy recuperative aircraft (FIERA) engine. The primary goal of this research was to determine if multistage intercooling using only the stator blades of the compressor is sufficient to provide the heat transfer required to obtain appreciable improvements in engine and combustion performance. This was split into three investigations: a small-scale examination of a single airfoil heat exchanger, an analysis of an effectiveness-NTU model for a full-scale, multistage-intercooled, axial compressor, and an investigation of the combustion characteristics of thermally enhanced kerosene. This work helped to identify a few insights, as well as a few failings of the envisioned FIERA engine. First, it is likely that the fuel consumption at cruise is not sufficient to provide adequate heat sink potential to provide substantial compressor intercooling even if high values of heat exchanger effectiveness are achieved. Secondly, the area provided by compressor stators alone appear to be insufficient to realistically approach high effectiveness values. Lastly, cracking of the fuel would likely not take place in a solely intercooled engine unless an engine with a very high overall pressure ratio (>60:1), or an intercooled recuperative engine was used. Therefore, it is of the author's opinion that using the fuel in a commercial turbofan engine to create a more complex thermodynamic cycle would not be worthwhile.

Acknowledgements

First and foremost, I would like to thank my parents, Paul and Robin, and my two older brothers, Neil and Alec, for their continuous love and support throughout my life and education. I am also grateful to my friends for their dependable support and unwavering camaraderie.

I am thankful for the teachings and mentorship of my advisor, Dr. Paul Erickson, who has guided me extensively throughout my undergraduate and graduate education. I would like to thank my committee members, Dr. Vinod Narayanan and Dr. Benjamin Shaw, for their time, patience, and invaluable feedback.

I am also grateful for the support of my fellow researchers in the Energy Research Laboratory, in particular Kellen Ochi, Michael Horton, and Kyle Heinzman, who helped me immensely with my research.

Lastly, I am thankful for the funding provided for this project by the Office of Naval Research and the early work conducted by George Herrera and Jonathan Doyle.

Chapter 1

Introduction

1.1 Motivation

Aircraft engine technology has evolved significantly since its inception, allowing many industries to develop and flourish including the commercial aircraft market, valued at 197.4 billion USD in 2020 and projected to reach 218.8 billion USD by 2026. [1] A dominant driver of innovation in this market comes from the push to reduce the amount of fuel burned and increase the aircraft's overall engine efficiency. However, with a greater push towards cleaner energy and carbon neutrality in the last few decades, an additional driving force has become increasingly prominent, and that is emissions.

In January of 2021, the Environmental Protection Agency (EPA) issued a greenhouse gas emissions standard for aircraft for the first time in US history, specifically matching the international airplane carbon dioxide standards adopted by the International Civil Aviation Organization (ICAO) in 2017. [2] The EPA already has regulations on other combustion products including smoke, unburned hydrocarbons, carbon monoxide, non-volatile particulate matter, and oxides of nitrogen, which have been getting stricter over time leading to new technological developments. Unfortunately, this new regulation is not expected to have a significant impact on emissions in the next few years as uncompliant engines are phased out, since most of all affected airplanes are expected to already conform to these new standards. [3] Regardless, this is a step in the right direction and will likely lead to more stringent emission standards over time and thus more improvements to meet them.

This significant push for cleaner, more efficient transportation and energy production systems both in the US and abroad has led to many advances in these sectors and some promising and economically viable paths forward for many industries, but commercial aviation is somewhat of an outlier. Currently there are four main potential alternatives to fossil fuel powered aircraft, and they are hydrogen, biofuel, e-fuel, or electric powered aircraft. However, all four still have significant hurdles in their way from large investment costs, safety hazards, and feedstock scalability issues, to reduced range and passenger capacity.

Consequently, fossil fuel powered gas turbines are likely to continue to dominate the commercial aviation industry for at least the next few decades and thus it is important to pursue concepts that may improve their efficiency and emissions. The work presented here investigates one such idea called the fuel-integrated energy recuperative aircraft (FIERA) engine. This would be a high-bypass turbofan engine, like the vast majority of commercial passenger aircraft engines, but it additionally utilizes the heat sink capacity of the fuel to remove heat from the compressor and other areas of the engine while simultaneously thermally enhancing the fuel injected into the combustor. The background to understand how this system can theoretically improve current turbofan engines will be discussed in the following sections.

1.2 Background

1.2.1 Gas Turbines and the Brayton Cycle

At its most fundamental level, gas turbines seek to extract useful work from the combustion of a fuel with air. The thermal energy released can be converted to mechanical energy and then to electrical energy in the case of gas-fired power plants, or it can be used to produce thrust in the case of aircrafts. Both setups employ three key components shown generically in Figure 1.1: a compressor, a combustor, and a turbine.

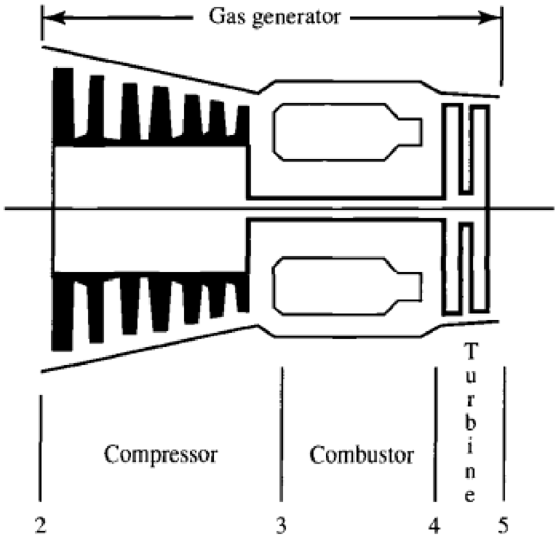

Figure 1.1: Schematic diagram of gas generator [4]

The compressor first converts the kinetic energy of the working fluid into pressure. Then, energy is added via the burning of fuel in the combustor. Lastly, some mechanical energy is extracted from the hot, high-pressure gases in the turbine to drive the compressor. However, a large amount of useful energy still remains in the exhaust as more energy was added in the combustor than was extracted in the turbine. This can be simply exhausted through a nozzle for maximum thrust in aviation applications, or it can be used for other power generation methods such as a steam-topping cycle, forming what is known as a combined cycle gas turbine.

Gas turbines can be simplified for general thermodynamic analysis into what is known as an open or closed Brayton cycle. The former is how a jet engine operates by pulling in clean air and not reusing the exhaust, while some ground and power generation applications use the closed Brayton cycle, which does recirculate the exhaust. Since the focus of this work seeks to improve aviation applications of the gas turbine, only the open Brayton cycle will be discussed.

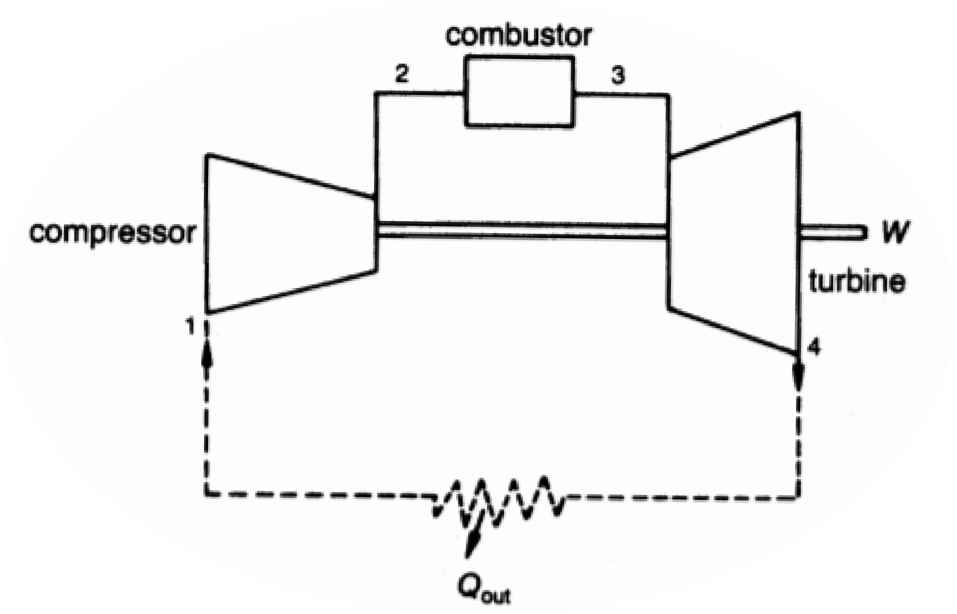

Figure 1.2: Open Brayton cycle layout [5]

Figure 1.2 shows the open Brayton cycle layout with the three main components of the gas turbine as discussed before. Correspondingly, the working fluid undergoes three key processes visualized on the ideal T-s and p-v diagrams shown in Figure 1.3. The air is compressed isentropically, increasing the pressure and temperature. The fuel then burns with the air isobarically in the combustor, significantly increasing the temperature of the working fluid.

Next some energy is extracted from the expanding gases in the turbine isentropically, leaving a relatively high temperature gas that can be exhausted for thrust. It should be noted that these are the ideal processes and there are always losses in an actual system that shift this from the ideal case.

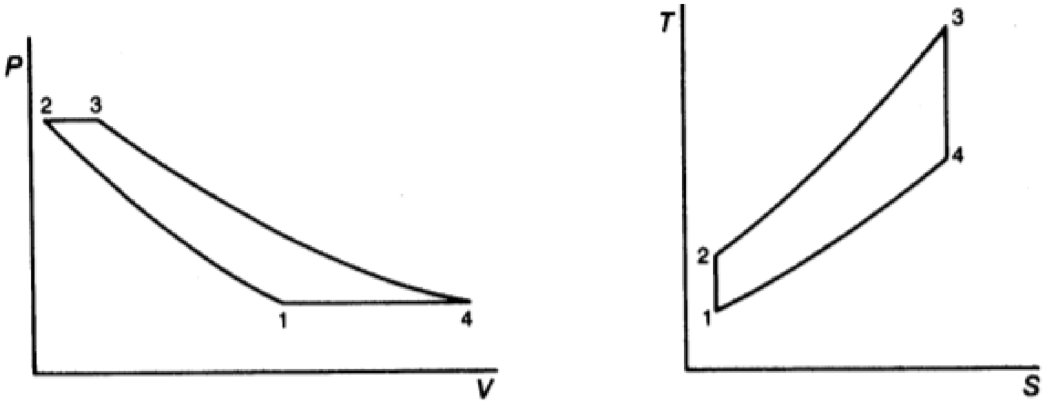

Figure 1.3: Ideal p-v and T-s diagram of air-standard Brayton cycle [5]

1.2.2 Intercooling and Recuperation

There are a few ways the Brayton cycle can be significantly improved from an overall thermodynamic approach. The first is by means of compression with intercooling. As seen in the previous section, compression causes a significant increase in the air temperature, which in turn requires more energy to compress. If the temperature were to be reduced during the compression, less back work from the turbine would be needed. However, the practical application of compression while simultaneously having significant heat transfer is difficult, so heat exchangers referred to as intercoolers can be used between compressor stages instead. Figure 1.4 shows how an intercooler between two compressor stages would change the p-v and T-s plots in relation to the simple cycle. The important thing to notice is the crosshatched area on the p-v diagram representing the reduction in work achieved with this single intercooler.

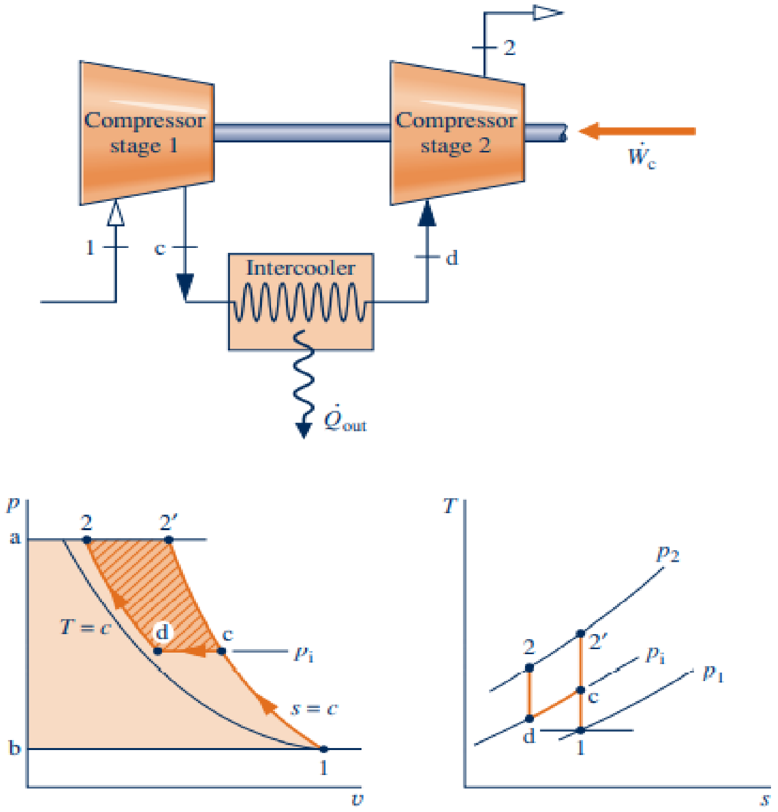

Figure 1.4: Effect of intercooling on p-v and T-s diagram [6]

In practice, intercooling has been used widely in land-based power generation gas turbines and is sometimes used multiple times between stages of very large compressors to maximize this concept's benefits. [5] However, this concept has failed to see use in aerospace applications as engine weight and size become significant design considerations and having a heat exchanger not only to remove heat, but another one to reject heat, can add significant weight to the system.

Recuperation is another method by which this cycle can be improved. Recuperation which is interchangeable with regeneration with regards to gas turbine applications, is the process of using the hot exhaust gas to preheat the air leaving the compressor before it enters the combustor. The gas-to-gas heat exchanger that enables this is called a recuperator or a regenerator. Figure 1.5 shows the new T-s diagram with the recuperator addition, illustrating how the heat from combustion only needs to increase the air temperature from state x to state 3 rather than from state 2 to state 3. This requires burning less fuel, and thus increases thermal efficiency. However, one thing to note is that the exhaust temperature goes down, reducing the amount of thrust from the engine core, and consequently the propulsive efficiency. These tradeoffs as well as the current level of research into the aero applications of these two complex cycles will be explored in more detail in Section 2.2.1.

Like intercooling, regeneration is used extensively in power production applications and in marine engines because of the benefits discussed, but as of now also suffers the same lack of adoption in aerospace applications largely due to size and weight considerations. [5]

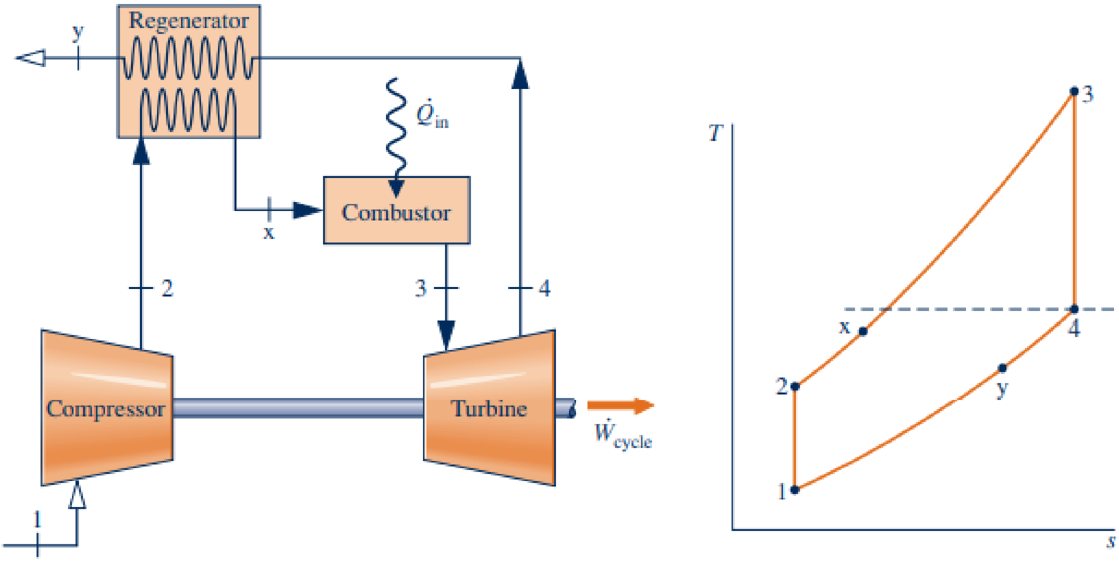

Figure 1.5: Ideal regenerative air-standard gas turbine cycle [6]

1.2.3 Turbofan Engine

The Brayton cycle and gas turbine concept form the basis for all airbreathing jet engines, which includes turbojet, turbofan, turboprop, turboshaft, ramjet, and scramjet engines. The one most widely used for passenger aviation is the high-bypass turbofan engine illustrated in Figure 1.6, owing to its high thermal and propulsive efficiency, and consequently its low thrust specific fuel consumption (also referred to as specific fuel consumption). Most turbofan engines have a two-spool design, with a low-pressure compressor section powered by a low-pressure turbine section rotating at one speed, and a high-pressure compressor section powered by a high-pressure turbine section rotating at a higher, more optimal speed for engine performance.

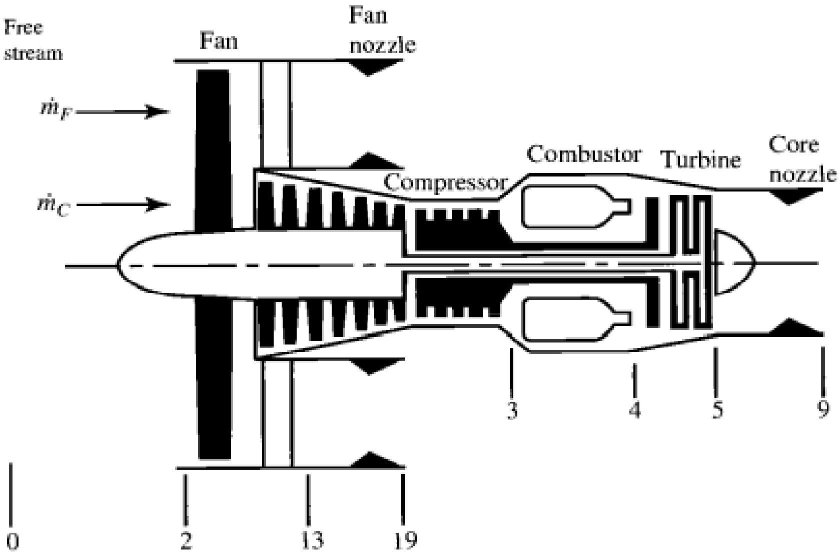

Figure 1.6: Turbofan engine layout and station numbering [4]

The most common metrics to compare engine performance are propulsive efficiency, thermal efficiency, and thrust specific fuel consumption. Propulsive efficiency is defined as the conversion of the kinetic energy of air to propulsive power as it passes through the engine. Thermal efficiency, or motor thermodynamic efficiency, is the conversion of the energy supplied in the fuel to the kinetic energy of the air. The product of these two gives the overall efficiency of the engine. These relationships are shown in Equation 1.1, 1.2, and 1.3, respectively. Lastly, the engine's thrust specific fuel consumption is simply the mass of fuel required per unit of thrust as shown in Equation 1.4.

$$\eta_P = \frac{Thrust\ power}{Power\ imparted\ to\ engine\ airflow} \tag{1.1}$$

$$\eta_{th} = \frac{Power\ imparted\ to\ engine\ airflow}{Rate\ of\ energy\ supplied\ in\ the\ fuel} \tag{1.2}$$

$$\eta_{tot} = \eta_P \eta_{th} \tag{1.3}$$

$$TSFC = \frac{\dot{m}_f}{F} \tag{1.4}$$

Table 1.1 lists some important details of two low-thrust class and two high-thrust class turbofan engines, which help to illustrate some of the trends and improvements in turbofan engines over the decades. The first three engines were chosen for this comparison because of their huge commercial success, with the JT-8D and CFM56 engines selling roughly 14,750 and 30,000 units, respectfully. [7] [8] The GE9x engine was chosen because it is currently the most powerful and advanced commercially available turbofan engine, so it will be referenced as the current state of the art.

Table 1.1: Specifications of four turbofan engines [9] [10] [11] [12] [13]

	Low-Thrust Class Turbofan Engines (<200kN)		High-Thrust Class Turbofan Engines (>200kN)	
Engine Model	JT-8D-17R	CFM56-5C2	GE-90	GE9x
Company	Pratt & Whitney	GE and CFM International	General Electric	General Electric
In Use Since	1970	1992	1995	2020
First flew on	B-727, B-737, DC-9	A-340	A-340, B-777	B777-9
Weight (dry) [kg]	1,585	3,856	7,893	9,630
Overall length [mm]	3,137	2,616	4,775	5,690
Fan diameter [mm]	1,080	1,836	3,124	3,400
Overall pressure ratio	17.3	37.4	39.3	60
Bypass ratio	1.0	6.6	8.4	9.9
Thrust at takeoff [kN]	72.9	138.8	388.8	490
Thrust during cruise	18.9	30.78	70	---
TSFC at sea level static (SLS) [g/kN-s]	23.37	16.06	8.30	---
Air mass flow rate at SLS [kg/s]	148	466	1350	---
Compressor stages	2F, 4 LP, 7 HP	1F, 4 LP, 9 HP	1F, 3 LP, 10 HP	1F, 3 LP, 11 HP
Turbine stages	1 HP, 3 LP	1 HP, 4 LP	2 HP, 6 LP	2 HP, 6 LP
Combustor Description	Can-annular combustor	Single annular combustor	Double annular combustor	Single annular combustor with TAPS injector

One of the most important things to notice in Table 1.1, is the increase in fan diameter and overall pressure ratio (OPR) over the years, allowing for a higher bypass ratio (BPR), and consequently a lower specific fuel consumption. The higher thrust engines also have higher air mass flow rates as expected, along with different types of combustor technologies, which will be discussed in Section 2.1.3. The increased pressure ratios, along with other advancements, have also significantly increased the temperatures achieved in turbofan engines, although there is limited available data on newer engine models.

That being said, Table 1.2 shows some of the relevant temperatures of two engines developed in the 1960s and 1970s to get an idea of the temperatures in the compressor and turbine sections. The values shown are from Pratt and Whitney's JT-8D and JT-9D engines, which were developed for the Boeing 727 (mid-size, mid-range narrow body airliner) and the Boeing 747 (large, long-range wide-body airliner), respectively. It should also be noted that the JT-8D and JT-9D engines have overall pressure ratios around 16:1 and 22:1 depending on the exact engine model and are thus not entirely representative of the newer engine generations. [13] For example, newer axial flow compressors with overall pressure ratios of 30:1 and 40:1 often have compressor exit temperatures of 538°C - 621°C. [5] This would be even higher in the case of the GE9x with its OPR of 60:1. Consequently, as these pressure ratios continue to increase, it becomes even more appealing to recover some of the compressor heat in a useful manner.

Table 1.2: Temperature and pressure data from some engines at different stations [4]

	JT-8D turbofan, mixed exhaust	JT-9D turbofan, separate exhaust
T_{t2}, °C	15	15
$T_{t2.5}$, °C	179	99
T_{t13}, °C	88	54
T_{t3}, °C	427	471
T_{t4}, °C	938	1,077
T_{t7}, °C	477	454
Bypass ratio	1.1	5.0
Thrust [kN]	62	193
Airflow [kg/s]	143	678

The turbine inlet temperature has also seen dramatic increases over the years from advancements in both material and cooling technologies. Current alloys and cooling techniques allow the turbine inlet temperature to reach 1,650°C, which is a large step up from the JT-8D and JT-9D engines. [9] Figure 1.7 illustrates this trend along with some of the advancements enabling it, which will be discussed in Section 2.1. Once again, these higher temperatures present opportunities for thermal recovery especially in components that already need to be actively cooled.

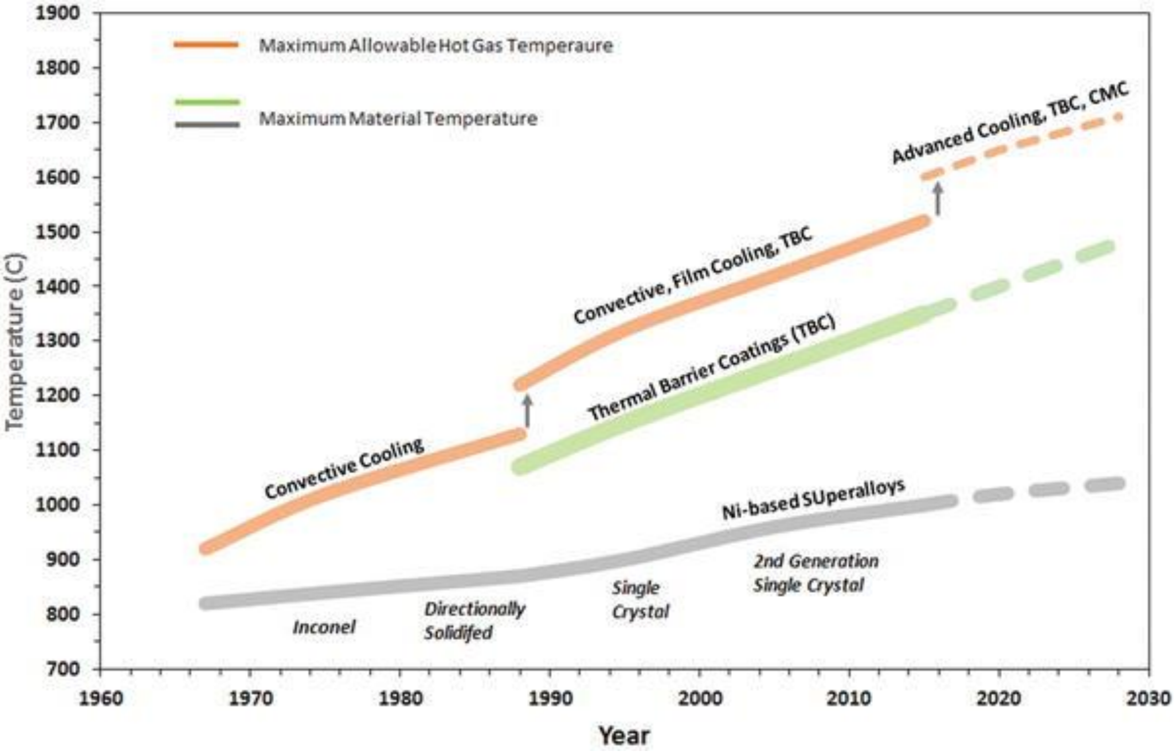

Figure 1.7: Evolution of gas turbine inlet temperatures, materials, and cooling technologies [14]

1.2.4 FIERA Engine

The fuel-integrated energy recuperative aircraft (FIERA) engine is a high-bypass turbofan engine that builds on the concepts of intercooling and recuperation but provides additional benefits while minimizing the drawbacks that arise in aero-specific applications. As the name suggests, the fuel is used as a heat sink to remove heat from the compressor and recover waste heat from other areas of the engine. This method provides a few advantages over the standard intercooler and recuperator concepts.

First, a full refrigeration cycle is no longer needed for the compressor intercooling, which usually requires a secondary heat exchanger in order to reject waste heat. Instead, only the intercooler and pump are required, which cuts down on size and weight. Furthermore, since fuel pumps are already employed to move fuel from the tanks to the combustor, the only main addition is the intercooler. The second advantage of such a system comes from the potential combustion benefits of a thermally enhanced fuel. Lastly, liquids typically have higher convective heat transfer coefficients than gases, theoretically reducing the heat exchanger size needed to match the performance of typical gas-to gas heat exchangers.

The most general layout for the FIERA engine is shown in Figure 1.8, with the fuel being preheated in the compressor and turbine sections before being injected into the combustor. Some variants of this concept have previously been investigated and will be discussed in Section 2.2.2.

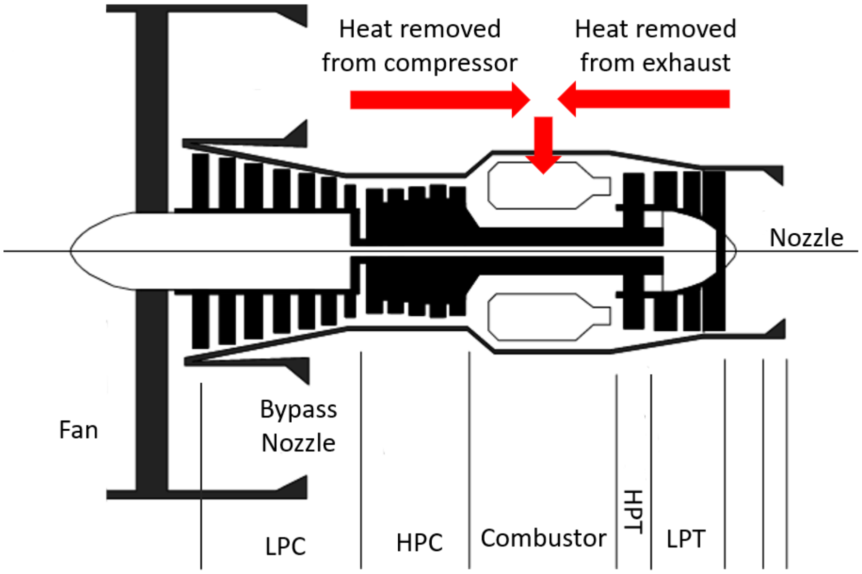

Figure 1.8: FIERA engine layout adapted from [15]

1.2.5 Thermally Enhanced Fuels

There are three possible paths that result in a thermally enhanced fuel. First and foremost is simply increasing the fuel temperature through sensible heat. This is often the main source of a fuel's heat sink capacity, which is proportional to the maximum temperature change it can achieve and its specific heat ($C_p \Delta T$).

The second way a fuel can be thermally enhanced is if it undergoes a phase change from liquid to gas as this reduces the amount of energy needed from the combustion itself due to the latent heat of vaporization. These methods are already ubiquitously employed for liquid rocket propulsion systems. An example that illustrates this is a rocket engine employing liquid hydrogen as its propellant. The reason cryogenic liquid hydrogen is used is twofold. First, and most importantly, it dramatically increases its density, and thus volumetric constraints can be met. Secondly, it can be used to cool components, most notably the rocket nozzle, whose materials would otherwise melt if no cooling mechanism was present.

The third way a fuel can be thermally enhanced is known as fuel cracking or fuel pyrolysis and is applicable only to endothermic fuels such as jet fuels, which are mixtures of various hydrocarbons. During pyrolysis, the fuel undergoes chemical decomposition into lighter products such as hydrogen, methane, and ethylene, which results in different, and potentially improved combustion characteristics. Fuel cracking can take place via two methods: catalytic pyrolysis or thermal pyrolysis. The prior can be accomplished at lower temperatures (often around 500°C) but requires a catalyst. The latter takes place typically around 600°C. It should be noted that these values can vary greatly in practice for a few important reasons. One is that cracking not only depends on temperature, but also pressure, residence time, and the specific composition of the hydrocarbon fuel. These all affect the conversion rate, and conversion product species as will be discussed further in Section 2.3.

The FIERA engine plans to thermally enhance the fuel, though the extent of this enhancement depends solely on the heat transfer that can be achieved from the particular design under changing operating conditions.

1.3 Problem Definition

Although alternative means of propulsion may one day change this, gas turbines will likely continue to be the dominant means of propulsion for the commercial aviation industry for the next few decades. To meet the performance, economic, and environmental goals of the future, these aircraft engines need to improve. The challenge that aeroengine designers face is how to reduce fuel burn, emissions, and noise while maintaining high thrust-to-weight ratios and high thermal and propulsive efficiencies.

1.4 Research Objectives

The primary goal of this research was to determine experimentally if multistage intercooling using only the stator blades of the compressor is sufficient to provide the heat transfer required to obtain appreciable improvements in engine and combustion performance. A breakdown of this goal and other objectives are listed below.

1. Synthesize Research

   Some of the significant improvements in gas turbine technology over the years and some active areas of research were to be examined to give context on the current state of the art, as well as show how the FIERA engine can mesh with existing technologies. Since the FIERA concept is built on the idea of using the fuel as a heat sink, it was also important to understand how the properties of the fuel and combustion characteristics may change.
2. Experimental Determination of the Average Heat Transfer Coefficients

   The average heat transfer coefficients were to be determined for a single stator heat exchanger setup using an energy balance and LMTD approach. Namely, empirical equations relating the heat transfer coefficients to three tested variables were to be created.
3. Prediction of the Fuel and Air Compressor Exit Temperatures

   The overall heat transfer coefficient determined experimentally was to be integrated into an effectiveness-NTU model for a full-scale, multistage-intercooled, axial compressor to determine what air and fuel exit temperatures could be expected in such a system.
4. Experimental Investigation of Combustion Characteristics of Thermally Enhanced Fuel

   Combustion experiments with thermally enhanced kerosene were conducted to determine changes in combustion characteristics.

Chapter 2

Literature Review

2.1 Gas Turbine Advancements

Gas turbine-powered commercial aircraft have seen significant improvements since their establishment in the 1950s. Fuel efficiency is one of the primary metrics that can illustrate this. Figure 2.1 shows the percent decrease in fuel burn per seat mile over the years compared to a 1950s baseline, demonstrating an average decrease of roughly two percent per year since 1970. About half of this gain comes from improvements to the aircraft, while the other half is from engine advancements. [16] Sections 2.1.1, 2.1.2. and 2.1.3 will highlight some of these key engine innovations and discuss their potential impact on the FIERA engine.

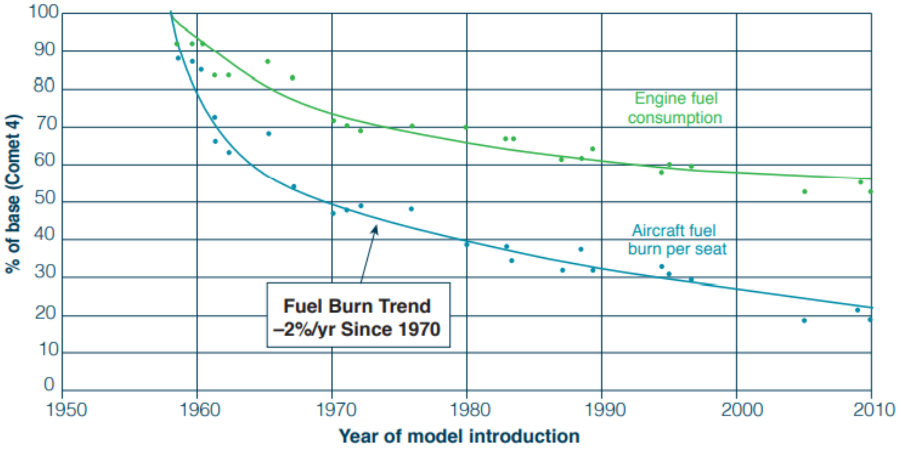

Figure 2.1: History of commercial aircraft fuel burn per seat-mile [16]

2.1.1 Material Improvements

Significant research has gone into developing materials that are able to withstand the harsh environments in gas turbines, with a desire to create materials that allow for the highest possible turbine inlet temperatures and consequently highest thermal efficiency.

For many years, the solution to this was devising better nickel superalloy compositions that can operate at higher fractions of their melting point while retaining good mechanical strength, resistance to thermal creep, and corrosion resistance. These superalloys were conventionally cast to form polycrystalline turbine airfoils, consisting of small equiaxed crystals or grains. Although they have fairly good properties in all directions, the grain boundaries provide sites for voids to form or slippage to occur, which can ultimately lead to blade failure. To mitigate this life-limiting mechanism, the number of grains was desired to be reduced leading to directionally solidified blades, and eventually single crystal blades shown in Figure 2.2. [17]

With that being said, even these single crystal superalloys have their limitations and complications. Gabb et al. [18] showed that the creation of unexpected grain defects in the single crystal superalloys significantly shorten the fatigue lives of these materials as they are typically designed with insufficient carbon, boron, or zirconium to strengthen the grain boundaries that are formed. Unfortunately, these defects can be created even in well-understood alloys because of variations in casting conditions, rough handling before heat treatment, or unexpected events during service. [18] [19]

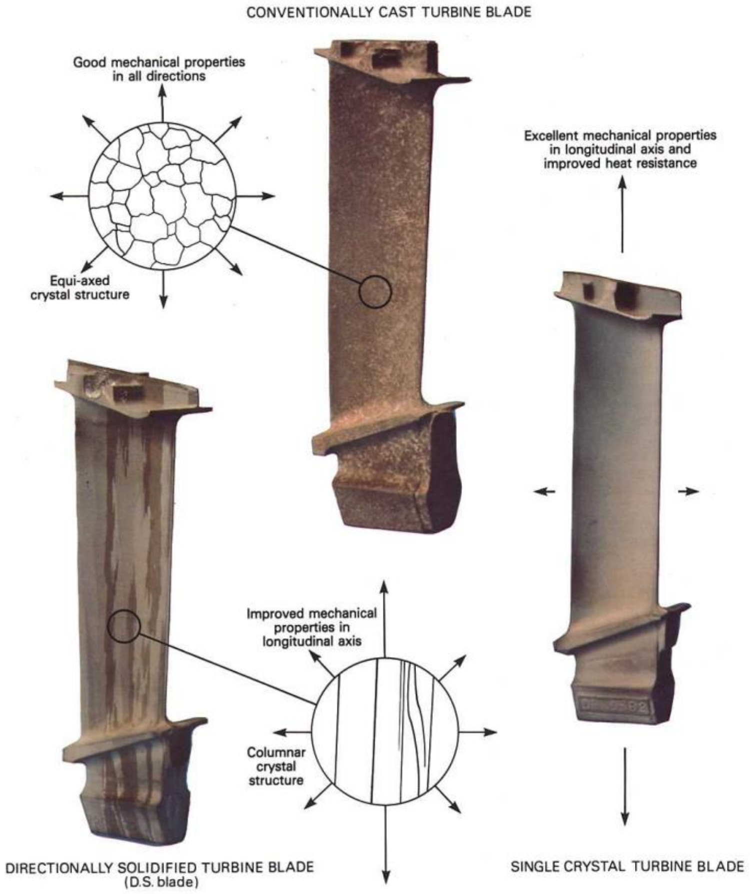

Figure 2.2: Conventionally cast, directionally solidified, and single crystal turbine blades [20]

To further improve turbine inlet temperatures above the melting point of these superalloys, considerable efforts have been made in the creation of thermal barrier coatings (TBCs) with much success. TBCs are multilayered systems typically consisting of a ceramic yttria-stabilized zirconia (YSZ) top coat and a metallic bond coat (either NiCrAlY, NoCoCrAlY, CoNiCrAlY or PtAl) that are deposited on the nickel-based superalloy substrate. The bond coat is more oxidation resistant that the superalloy, and it also promotes a thermally grown oxide (TGO) layer to form, further limiting oxygen diffusion from reaching the superalloy. The materials chosen for these layers must provide good thermal insulation, minimize thermal expansion mismatch, reflect radiation from the hot gases, and maintain thermal protection over many thermal cycles without failure. Currently, TBCs face a few general challenges, namely the reproducibility of the coating deposition and the development of a comprehensive model of the coating system and failure mechanisms over time. [21]

Additionally, some TBCs are already reaching their effective temperature limits as is the case for a common TBC called 7YSZ (made of ZrO_2 partially stabilized by ~7 wt% Y_2O_3). Above ~1,300°C sintering can occur, resulting in phase instability and the loss of strain tolerance. Even at ~1,200°C, molten silicate, collectively referred to as CMAS (calcia–magnesia– alumino–silicate), ingested by the engine in the form of sand or ash, can penetrate deep into the TBC and cause premature failure. [22]

One way of circumventing the issues presented by superalloys and TBCs, is by considering a completely different material such as ceramic matrix composites (CMCs). Currently, the most advanced CMCs are based on silicon carbide (SiC), or carbon matrix and fiber compositions made via chemical vapor infiltration (CVI). There are many variants of these materials being explored that offer different properties, but CVI SiC/SiC (silicon carbide matrix reinforced with silicon carbide fibers) is one of the most promising because of its resistance to thermal shock, impact resistance, toughness, and high strength to weight ratio. However, the lifetime of this composite is limited by its susceptibility to volatilization of the protective SiO_2 TGO layer that occurs when it reacts with water from the combustion products. [23] [24]

As such, a new type of coating has seen substantial research to mitigate this issue known as environmental barrier coatings (EBCs) or thermal/environmental barrier coatings (T/EBCs). EBCs are multilayer systems that consist of a bond coat, ceramic oxide environmental coats that prevent oxidation and volatilization of the TGO, and interlayers that can alleviate stress concentrations that arise from mismatching coefficients of thermal expansion. In the case of T/EBCs, a thermal barrier top coat is also used because of its low thermal conductivity. [23]

Figure 2.3 summarizes all these advancements and their effect on temperature capabilities over the years, in addition to how cooling can further extend these limits, as will be discussed in Section 2.1.2.

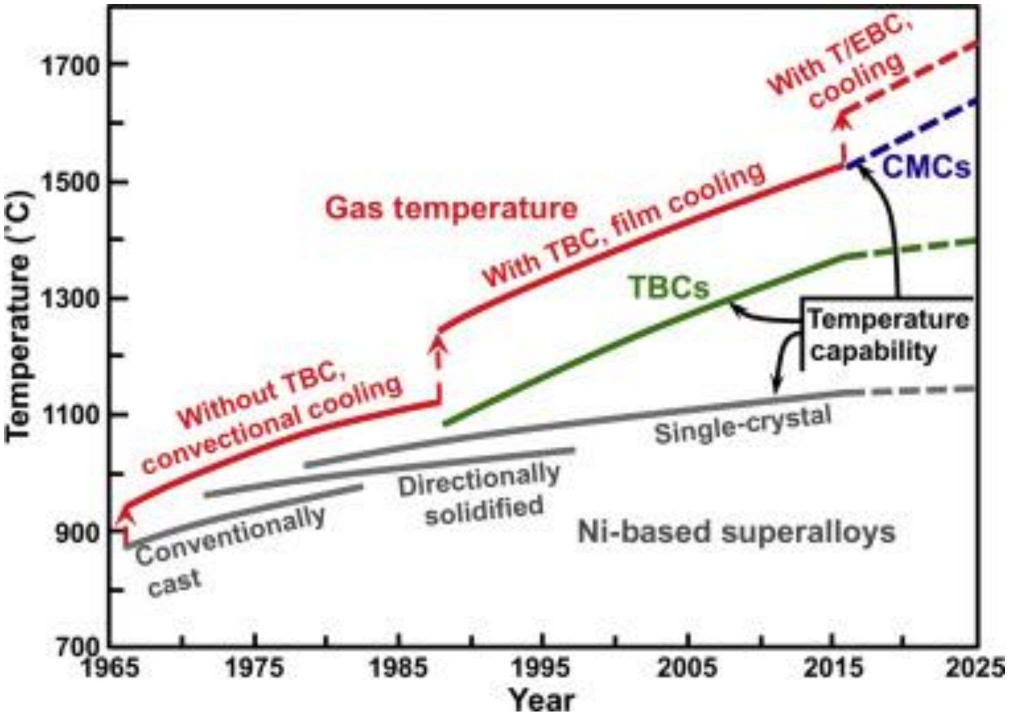

Figure 2.3: History of major improvements enabling increases in turbine inlet temperature [23]

These advanced materials are already seeing use in commercial aviation with the CFM LEAP engine being the first to incorporate a CMC into its design with the use of a CMC high-pressure turbine (HPT) shroud. In 2020, the GE9x engine entered service featuring an inner and outer combustor liner, as well as HPT Stage 1 shrouds and nozzles, and HPT Stage 2 nozzles. It is expected that CMCs will continue to phase out nickel-based superalloy parts being used in the engine hot section including the eventual replacement of the HPT blades and stators. [25]

With regards to the cooler sections of the engine such as in the compressor, there has been a lesser need for material improvements, though the materials used have changed over time to handle the new operating conditions and minimize weight. Steel and aluminum alloy compressor blades have largely been phased out in favor of titanium alloys with their high strength to weight ratios and relatively high temperature resistance. [4] However, nickel-based alloys are often used towards the rear of the compressor where temperatures of ~550°C can greatly reduce the strength of the titanium alloys. [26]

These materials and trends are important to understand when considering the FIERA engine for a few reasons. First, to improve these advanced engines with the FIERA concept, the same materials will likely need to be chosen and this determines not only the thermal conductivity of these components, but also if they can be compatible with an endothermic hydrocarbon fuel. This will be explored more in Section 2.3. Secondly, these trends provide some of the allowable surface temperatures of these materials, which will be used when evaluating this system.

2.1.2 Cooling Techniques

The other method to further increase the operating temperature of the engine, and consequently the thermal efficiency, is to incorporate some form of cooling as was shown in Figure 2.3. Cooling allows the turbine inlet temperature to be significantly higher than the materials' thermal limits. This was first accomplished with single pass internal (convection) cooling, but has since led to multi-pass internal cooling, impingement cooling, and external film cooling. [20] [14] [4] These methods are illustrated in Figure 2.4. Of these methods, film cooling is the most effective at reducing blade temperature because the film that forms over the blade simultaneously cools the blade surface as it passes over it and prevents significant heat transfer from the hot gases to the blade.

However, all these methods have a few drawbacks. For example, the main disadvantage of early internally cooled blades was their failure to sufficiently cool the trailing and leading edges, which are respectively very thin and experience the highest temperature, making them most susceptible to failure. Film cooled blades do not suffer this issue, but instead experience turbine efficiency losses from the injection of air into the boundary layer. In both internally and externally cooled blades, significant decreases in turbine efficiency occur with increasing bleed air. Therefore, it is critical to keep this amount low so as not to nullify the thermal efficiency gains from the higher turbine inlet temperature. [17]

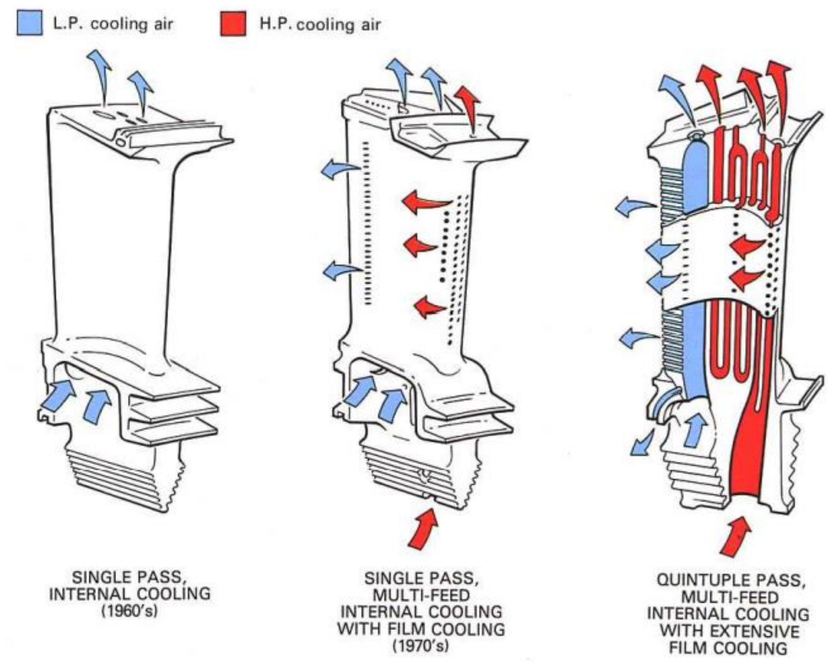

Figure 2.4: Development of high pressure turbine blade cooling [20]

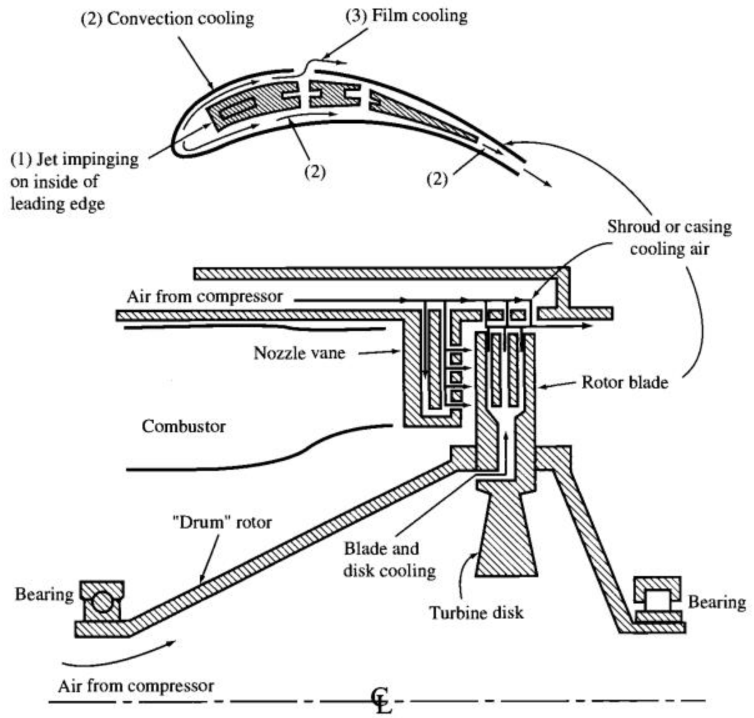

Figure 2.5: Schematic of air-cooled turbine [4]

Today, practically all large aeroengines cool at least the first-stage nozzle and rotor using bleed air from the compressor as shown in Figure 2.5. [9] Replacing this method with an equally effective system without the reduction in turbine efficiency is highly desired. Proposed liquid cooling alternatives have existed for decades to accomplish this, but to date, no liquid cooled turbine technology has been proven flight worthy. [27] The three main alternatives are thermosyphon systems that are driven by thermal buoyancy forces, heat pipe systems that use two phase flow with capillary structures, and forced convection systems that require an external pump. The main advantage these have over air-cooled systems comes from liquids' superior convective heat transfer coefficient owing to their high thermal conductivity, specific heat, and greater density. However, some disadvantages include larger thermal gradients across the blade wall causing larger thermal stresses, an increased potential for corrosion dictated by the coolant and materials chosen, and a much greater need to completely prevent coolant leaks from occurring. [28]

These problems were first shown in the 50s and 60s when the simplest, most effective, most reliable, and cost-efficient technique was still trying to be decided between the various forms of air and liquid cooled systems. Japiske [28] reviewed much of the research conducted on demonstrator turbines using the various liquid cooling methods revealing many with leakage, corrosion problems, or tip cap failure due to increased stress from centrifugal forces on the fuel. Fossen et al. [29] also reviewed the status of liquid cooling methods pointing out the lack of data and understanding of heat transfer, pressure drop, and flow stability in rotating turbine blades where centrifugal accelerations can reach up to 20,000 g's. Liquid starvation in some passages and flooding in others are also concerns that arise in multi-passage blades subjected to rotating environments. [30] Furthermore, liquid starvation can occur if the coolant escapes through cracks in the blade or worn-out seals, which can cause rapid increases in the blade temperature, and thus premature failure. A combination of these concerns, and the relative ease of using compressor discharge air, quickly propelled air cooling to be the predominant method of cooling in gas turbines in the 50s and 60s. Every iteration after sought to improve their effectiveness while liquid cooled systems' lack of general adoption led to less research and advancements.

That being said, advancements in materials and manufacturing techniques since then could now potentially enable their implementation to augment traditional air-cooled gas turbines. As previously discussed, the complications associated with liquid systems integrated into the rotating components make their use less appealing but appear more appropriate for some of the stationary components such as the nozzle vanes, stators, or combustor liners. This is equally true in the compressor. Therefore, the FIERA engine only seeks to alter some of the stationary components of the engine, while leaving the rotating equipment as-is (i.e. retaining compressor discharge cooled rotor blades). The synergy between the two systems provides the added benefit of supplying “cooled” cooling air from the intercooled compressor to the turbine blades, reducing the amount of bleed air required to maintain the blade temperature. It should also be noted that there may not be a significant weight penalty from the replacement of the conventional cooling system for these components as the ducting from the compressor sections to the turbine sections would essentially be replaced instead with piping for the liquid fuel.

2.1.3 Combustor Technology

The primary goal of the combustor is to reliably produce a stable flame over a wide operating range while minimizing the amount of particulate matter, unburned hydrocarbons (UHC), carbon monoxide (CO), and oxides of nitrogen (NOx) exhausted out of the engine. Unfortunately, these factors are not always positively correlated with respect to one another, so designs must compromise to reach acceptable levels. This is abundantly clear when considering UHCs, CO, and NOx. High levels of UHCs and CO is an indication of incomplete combustion either from local regions that are too fuel-lean to provide adequate burning, or too fuel-rich where there is insufficient oxygen to convert the CO to CO_2. Increasing the residence time or burning the fuel stoichiometrically would seem to be the solution to this, but NOx formation increases with residence time, particularly at the high flame temperatures (>1800K) reached near stoichiometric conditions as shown in Figure 2.6a, making this option less ideal. The general trends for these emissions against the primary temperature is shown graphically in Figure 2.6b. Although NOx can form by means of a few chemical pathways, thermal NO that forms via the Zeldovich mechanism is one of the major sources of NOx in gas turbines since its formation rate increases exponentially with temperature. [31] Smoke/soot on the other hand is predominantly formed because of local fuel-rich pockets from poor atomization or mixing, making injector design very important. The overall combustor design must take these considerations into account, while simultaneously maintaining flame stability across all power levels.

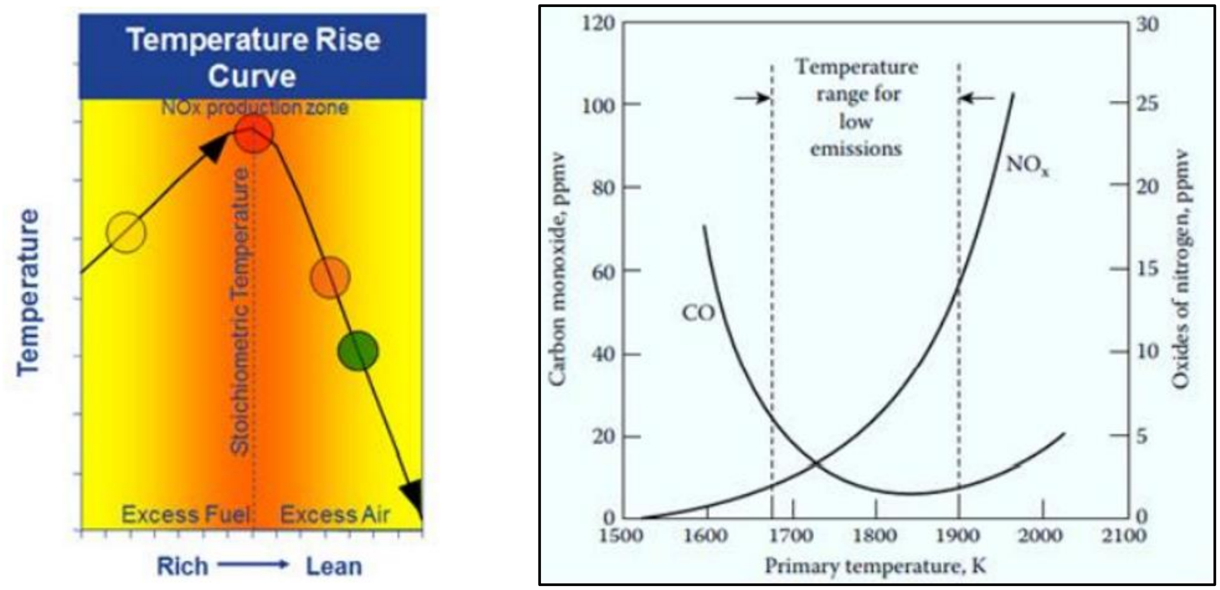

(a) (b)

Figure 2.6: (a) Temperature vs AFR (b) NOx and CO emissions vs primary temperature [32]

The desire to develop lower emission combustors has been further spurred by more stringent aircraft emission standards set forth by the International Civil Aviation Organization (ICAO) along with other entities. This has led to a combination of changes to the combustor layout and fuel injector design to fundamentally change the combustion process. The most advanced combustor technologies currently or soon to be implemented in commercial aeroengines to meet these standards are Rich-Quench-Lean (RQL) combustors, dual annular combustors (DACs), Twin Annular Premixing Swirler (TAPS) combustors, and Lean Direct Injection (LDI) combustors.

RQL combustors are spatially separated into three zones as shown in Figure 2.7: a primary zone that burns fuel-rich, an intermediate zone that quickly quenches the gas, and a dilution zone that burns fuel-lean. The fuel-rich zone normally burns with an equivalence ratio of 1.2-1.8 forming a stable, relatively low temperature flame with low amounts of NOx and high amounts of smoke, CO, and UHCs. More air is then quickly added in the quench region to further oxidize the CO and hydrocarbon intermediates. However, rapid formation of NOx can occur as local equivalence ratios pass the stoichiometric value. To mitigate this, additional air is added in the dilution zone so that complete combustion takes place under fuel-lean conditions with typical equivalence ratios of 0.5-0.7. [32]

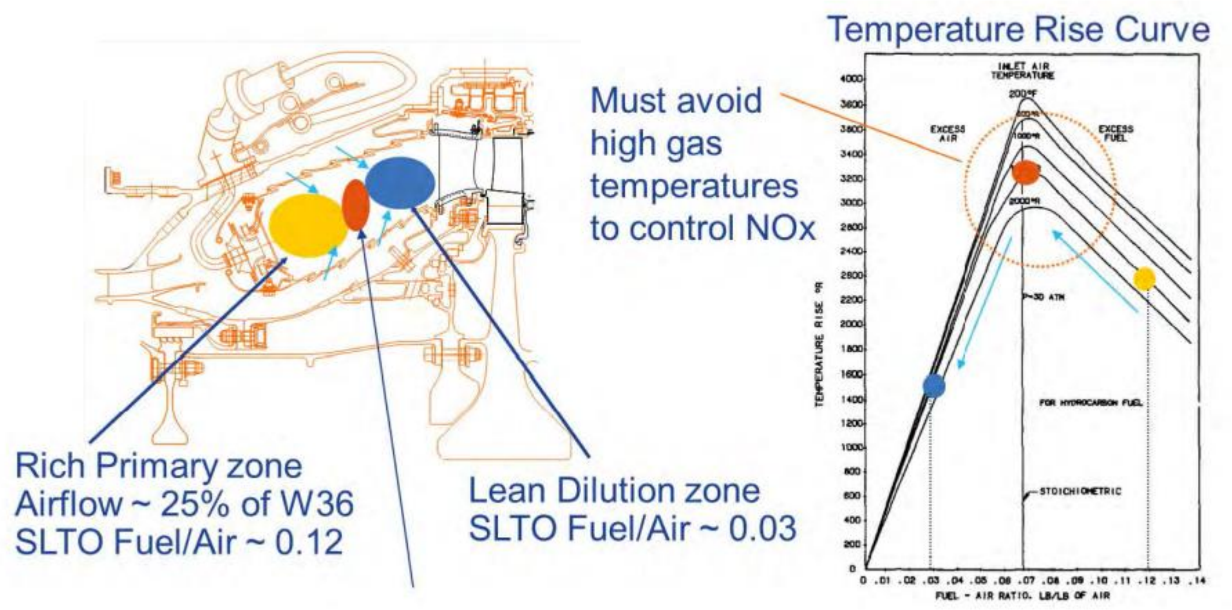

Figure 2.7: RQL combustion process in a single annular combustor configuration [33]

DACs differ from the single annular combustors (SAC) typically used with RQL systems as they have two radially separated zones as shown in Figure 2.8: a pilot outer annulus and a main inner annulus. Both regions operate at fuel-lean conditions with the pilot zone having an equivalence ratio of 0.6-0.8 depending on the power setting, while the main zone is only used for medium to high power settings, with a typical equivalence ratio of 0.6. The higher equivalence ratio of the pilot region in its low power configuration, ensures complete combustion and lessens the risk of flame instability. By burning fuel-lean, this method achieves low NOx and smoke emissions, but high pressure ratios tend to reduce its effectiveness since more compressor air has to be used for cooling. This decreases the amount of air available for combustion, making the fuel burn closer to the stoichiometric value, and thus hotter. The DAC configuration also tends to form nonuniform exit temperature profiles, which can cause additional thermal stress and impact the efficiency of the turbine. [32]

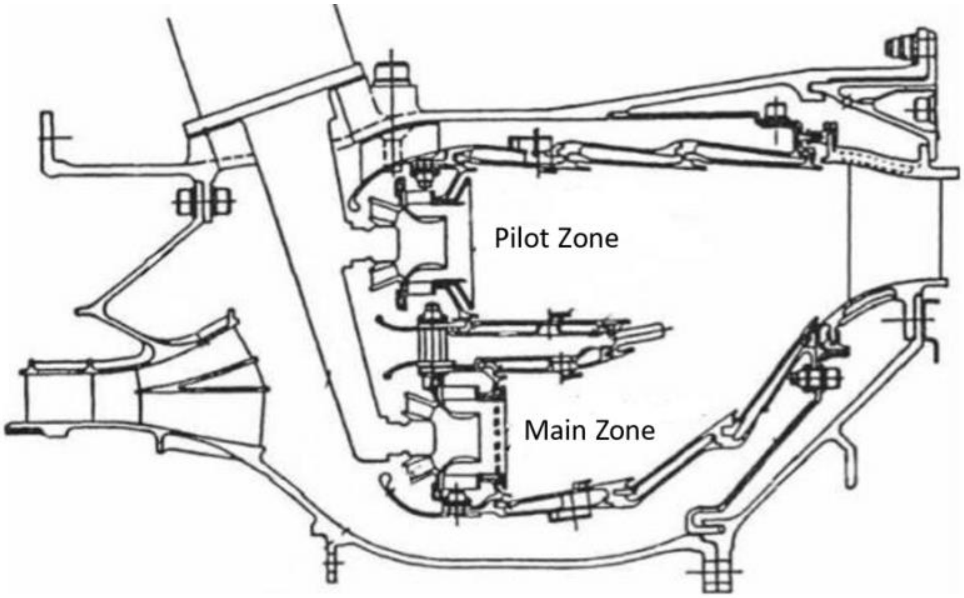

Figure 2.8: Dual annular combustor configuration [34]

The DAC system led to further development of lean burning techniques and the creation of the TAPS combustor. This combustor functions similarly to the DAC with a pilot and main combustion zone, but these regions are now created by a single complex fuel injector instead of two separated conventional injectors. This is shown in Figure 2.9. At starting and low power settings, only the central pilot injector operates to establish sufficiently high combustion efficiency and stability. At higher power modes, the main injector also becomes active, and functions to partially premix the fuel with air in cyclonic mixers before they are ejected and burned. Although this partially premixed fuel produces very low emissions, the possibility of autoignition becomes a concern. Consequently, short passages are used to lower the mixture's residence time since there is a delay associated with autoignition, which is dependent on the operating conditions of the combustor. [35] This nozzle was also found to have a high idle combustion efficiency interestingly attributed to carbon formations on the nozzle, that was referred to as "Good Karma, Good Coke", since coke formation is usually detrimental to performance. [36]

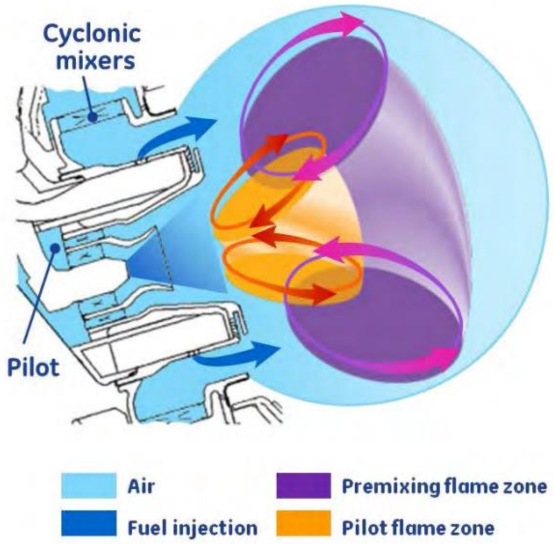

Figure 2.9: TAPS fuel injection concept [33]

To avoid the risk of autoignition and flashback that arises with the TAPS method, the fuel can be injected directly into the combustion zone. This technique is known as LDI and is shown schematically in Figure 2.10. It utilizes a multi-annulus injector similar to the TAPS injector with a pilot and main combustion region utilized for different power conditions. LDI requires mixing to take place very rapidly before the reaction can occur in order to derive the benefits of the lean combustion. If the fuel and air are not mixed uniformly and sufficiently in the short distance from the injector to the flame front, pockets of fuel rich regions will result in high NOx and smoke. Therefore, a large portion of air passes through axial swirlers in the nozzle head to mix with the fuel as it leaves the nozzle. [37]

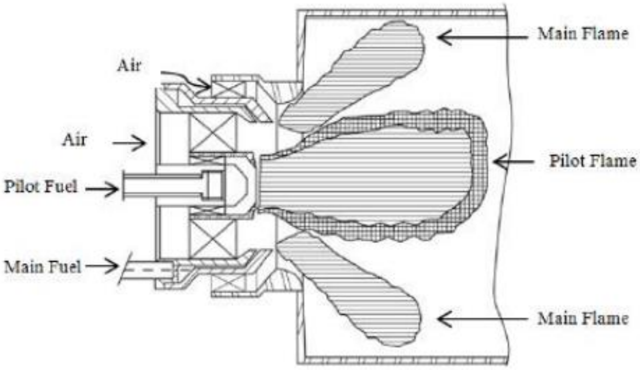

Figure 2.10: LDI injector head with bifurcated flow created by a splitter [38]

Although these are the most developed advanced combustor methods, a few other technologies should be mentioned that are of interest with regards to the FIERA engine. The first one being the Lean Premixed Pre-vaporized (LPP) combustor. As the name suggests, the fuel is vaporized and premixed with air before entering the combustion zone where it burns near the lean blowout limit. This greatly reduces the NOx and soot that forms, but also makes autoignition and flashback a high priority to be designed around. Unfortunately, this is only applicable for low pressure ratio engines (OPR < 25) since higher pressures and temperatures tend to decrease the ignition delay time. [35]

The higher pressure ratios in gas turbines of the future, brings to attention another aspect of combustion, namely the likelihood of supercritical combustion. Figure 2.11 illustrates the overall pressure ratio trend and projection for the next few years reaching supercritical or near critical pressures (~2 MPa) across all operating conditions. This by itself does not necessitate any specific changes to the injector as this is still in the classical atomization and spray regime having classical gas-liquid interfaces. However, if the fuel and ambient temperature are raised sufficiently (near the fuel’s critical temperature of 370-400°C), single-phase, dense-fluid injection dynamics dominate, and mixing becomes dictated by diffusion as discussed by Dahms and Oefelein [39]. They also demonstrated these regime transitions for the injection of n-decane at various ambient temperatures and pressures, representative of gas turbine operating conditions, as shown in Figure 2.12.

It is likely that the thermally enhanced fuel of the FIERA engine could extend farther into this diffusion dominated regime, perhaps necessitating the design of new injectors for optimal performance. Unfortunately, modeling supercritical fluids and supercritical combustion has proven challenging since fluid characteristics such as density and specific heat can vary widely. Nevertheless, a few attempts have been made recently for rocket engine applications and for hydrocarbon combustion with encouraging results. [40] [41] [42]

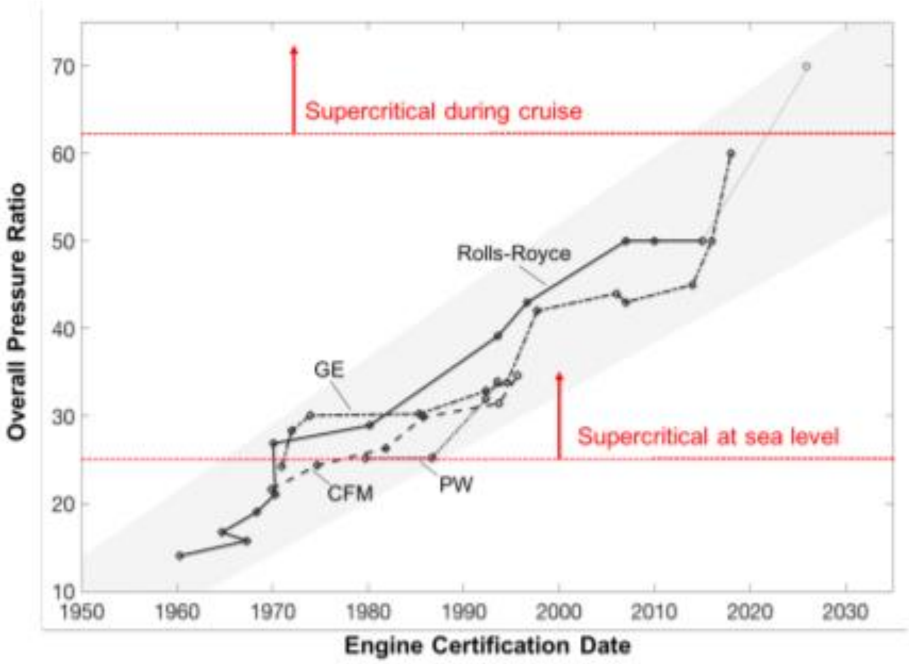

Figure 2.11: Gas turbine engine pressure ratio trends [42]

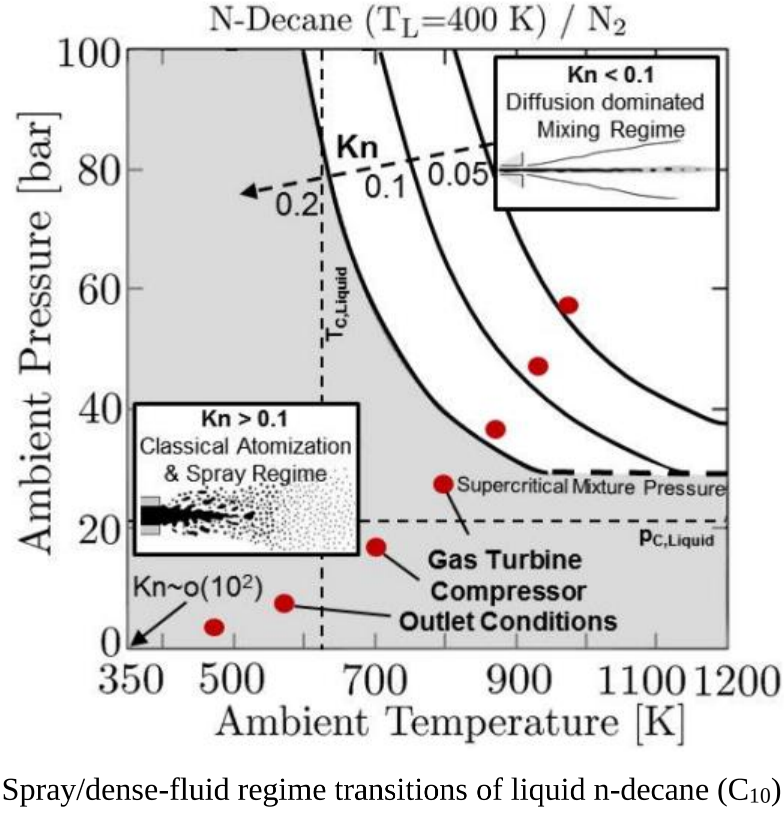

Figure 2.12: Spray/dense-fluid regime transitions of liquid n-decane (C_{10}) injection at a temperature of 400K into a gaseous nitrogen environment [39]

The last interesting concept of note is a fuel injector patented by GE that uses a plasma generator to break some of the fuel into hydrogen, acetylene, and smaller hydrocarbons to help extend the lean flammability limit of the fuel. [43] If this is implemented commercially, it may provide more of a path to the realization of the FIERA engine as this fuel decomposition can also be accomplished by heating the fuel sufficiently as will be discussed in Section 2.3.1.

Although these methods all have their merits, the FIERA concept would likely use a variation of the LDI combustor to produce a low emission, stable flame, with a low risk of autoignition and flashback in the injector. Other research into intercooled and intercooled recuperated aeroengines by Kyprianidis et al. [44] also pointed out the necessity of using lean-burn combustion technology in order to keep cruise NOx at acceptable levels in these engines.

2.2 Advanced Cycle Jet Engines

The advancements in materials, cooling techniques, and combustor technology have facilitated the development of vastly more fuel efficient and lower emission aeroengines since the 1940s. Yet, to improve further, more complex thermodynamic cycles are under investigation. These advanced cycles are based on the principles of intercooling and/or recuperation, though their specific implementation varies from design to design. Some of the most recent developments in this area will be examined as well as past research conducted on the FIERA engine.

2.2.1 Intercooled and Recuperative Aeroengine Research

As mentioned previously, intercoolers and recuperators are widely used in power generation and marine applications to reduce fuel consumption and increase power output but have yet to be integrated into aeroengines for their size and weight penalties. This does not discount them from use, simply that the heat exchangers and supplemental structures must be lightweight and compact, while maintaining low pressure losses and high effectiveness. A significant amount of research has gone into these complex cycles, particularly in the last 20 years, showing encouraging results.

A European technology program called the New Aeroengine Core (NEWAC) concepts [45] has been one of the most comprehensive assessments of these engines to date. Both an intercooled core (IC) and an intercooled recuperative aeroengine (IRA) configuration were investigated and are shown in Figure 2.13 and Figure 2.14. The proposed high overall pressure ratio (OPR) IC configuration uses a portion of the bypass air to cool the air of the LPC in an air-to-air cross-corrugated heat exchanger before it enters the HPC. It also proposed using an LDI combustor to meet emission standards as this technology can be implemented in very high pressure environments. The suggested IRA configuration on the other hand featured a radial HPC, a similarly designed intercooler, and a particular arrangement of tube heat exchangers in the nozzle to minimize pressure drop, while maintaining the recuperator effectiveness. Vlahostergios et al. [46] further optimized the configuration of recuperators in the model to provide as much as a 13.1% reduction in TSFC over a conventional non-intercooled and non-recuperated aeroengine. Furthermore, the IRA configuration was designed to operate at a much lower OPR than the IC configuration, making it more conducive to use LPP combustor technology. The differences in OPR for these configurations can be explained by conducting cycle analysis that shows that the optimal OPR for an intercooled cycle is higher (50-120) than that of a conventional core, while intercooled recuperative cycles have the highest thermal efficiencies at lower values of OPR (15-25). [5] [44] [47]

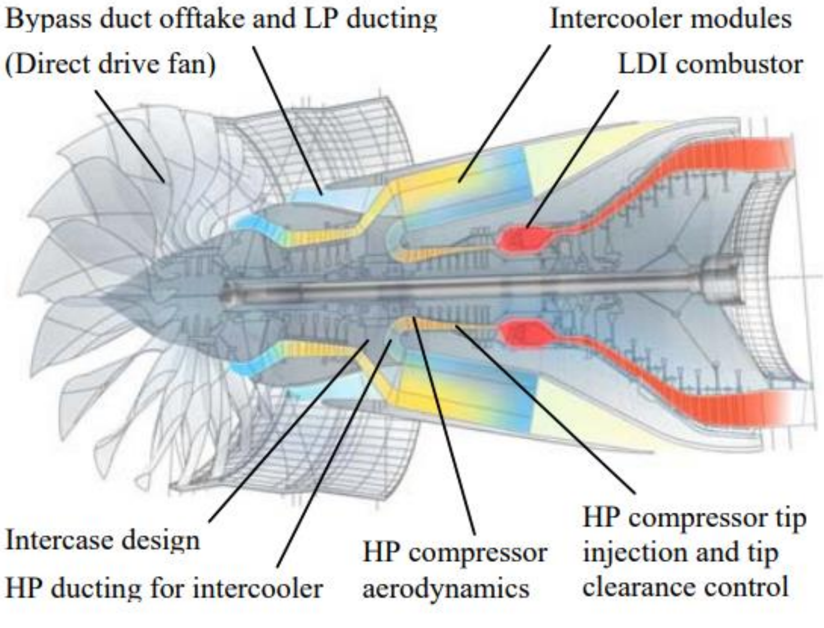

Figure 2.13: NEWAC intercooled core (IC) configuration [48]

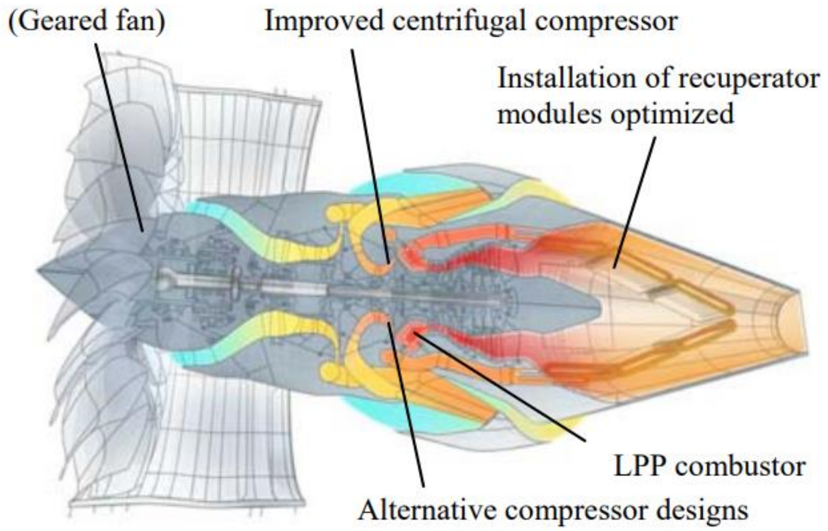

Figure 2.14: NEWAC intercooled recuperative aeroengine (IRA) configuration [48]

Ito et al. [49] took a different approach for the proposed intercooler and experimentally tested an air-to-refrigerant airfoil heat exchanger, similar to the one tested in this work. Their results suggested that the average air Nusselt number cannot be determined using only the air Reynolds number and Prandtl numbers as is the basis for essentially all empirical Nusselt number correlations. They attributed this to the large temperature fluctuations on the airfoil surfaces that change with varying refrigerant flow rates.

Lui et al. [50] investigated the boundary layer effects of cooling using a two and three-dimensional numerical model of a compressor stator vane and found that the laminar separation point along the blade was delayed, which is beneficial to the compressor’s aerodynamic performance. They also showed that cooling the blade and blade wall decreased the corner separation region, which reduced the pressure loss at the tip and consequently increased the total pressure rise in the stage.

2.2.2 FIERA Engine Research

A few investigations into the fuel-integrated energy recuperative aircraft engine concept have already been conducted utilizing component level engine analysis, which have shown promising results. An early version of the FIERA engine is shown in Figure 2.15 from [51]. Wong proposed using an intercooler between the LPC and HPC, and an exhaust recovery heat exchanger between the low-pressure turbine and the nozzle. The full-system configuration resulted in a few percent decrease in thrust specific fuel consumption, and additionally a few percent increase in the thermal, and overall efficiency. Interestingly, it was also shown that the intercooler alone could provide essentially the same benefits with slightly better thermal and overall efficiency, at the cost of a smaller reduction in specific fuel consumption. One thing that should be noted, was that this analysis was performed as a parametric study to determine some trends with changes in one or two variables at a time. Consequently, reasonable input engine specifications were chosen that are not necessarily optimized for these configurations, so performance characteristics could likely increase.

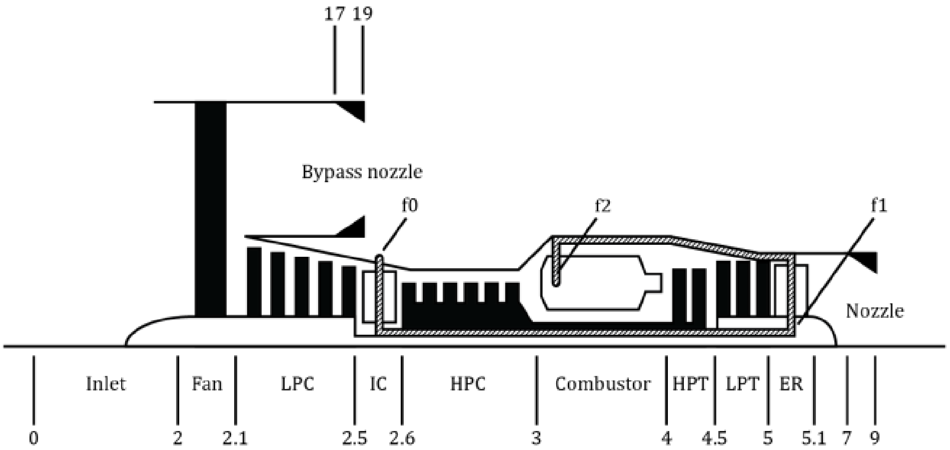

Figure 2.15: FIERA engine with intercooler and exhaust heat recuperator [51]

Nevertheless, an important trend that was identified was that the heat exchanger effectiveness and pressure drop significantly affect the performance characteristics. Figure 2.16a and Figure 2.16b show how these heat exchanger parameters affect the thrust specific fuel consumption for the full-system arrangement and the intercooler-only configuration, respectively. As expected, a lower pressure drop and a higher effectiveness resulted in a greater reduction in specific fuel consumption. The full-system configuration slightly beats out the intercooler-only configuration, but also has more of a penalty from pressure drop because of the additional heat exchanger. For this reason, in addition to mitigating the size and weight increases that would come with these heat exchangers, a variation of this system was investigated in [52] that sought to modify certain engine components (such as compressor vanes) to additionally function as heat exchangers, as discussed in Section 2.2.1.

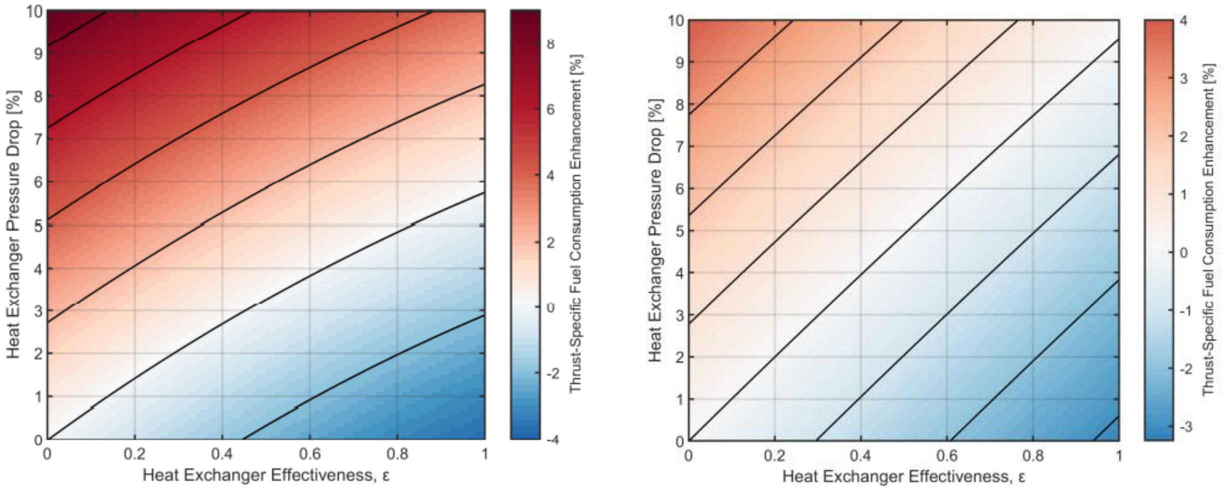

(a) (b)

Figure 2.16: Effect of pressure drop and effectiveness on TSFC enhancement for (a) full-system configuration (IC & ER) and (b) intercooler-only configuration [51]

Figure 2.17 shows some of the proposed modified components that could potentially serve this purpose, namely the stator blades, nozzle guide vanes, and nozzle wall channels. Figure 2.18 presents the layout of such a system as proposed by Herrera, which utilizes the compressor stator blades essentially as the intercooler, and the nozzle guide vanes and nozzle wall channels essentially as the exhaust recovery heat exchanger. In doing so, the components maintain functionality, while having a minimal effect on weight, complexity, and pressure drop.

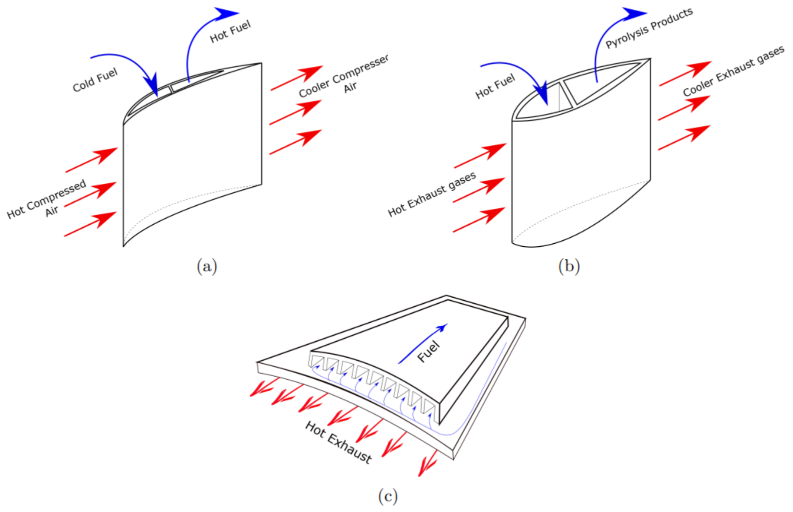

Figure 2.17: FIERA multipurposed heat exchanger components: stator blade (a), nozzle guide vane (b), and nozzle wall channels (c) [52]

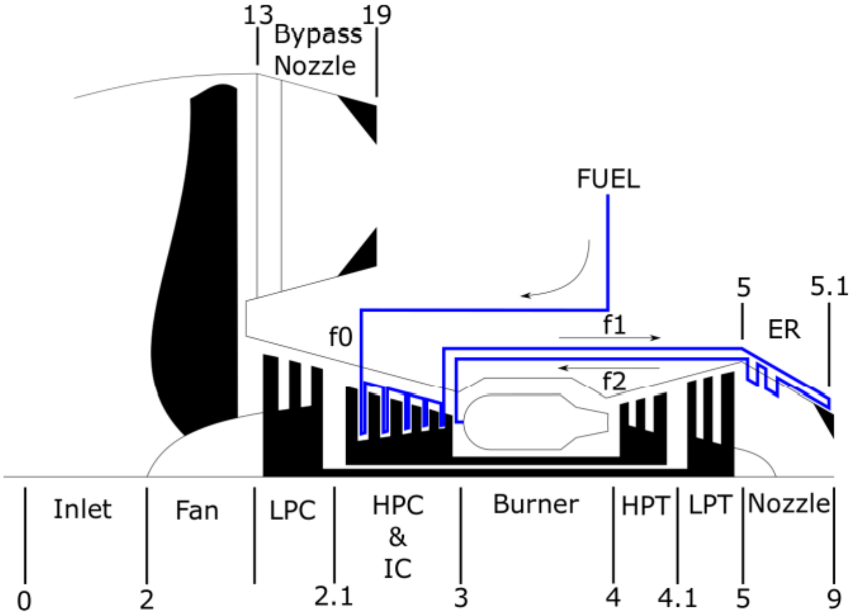

Figure 2.18: FIERA engine with multistage intercooler and exhaust heat recuperator [52]

The heat transfer effectiveness of the compressor stator blades was specifically investigated, and the computational model developed resulted in very low values, suggesting the surface area of the blades themselves may not be sufficient to produce the intended intercooling and fuel enhancing effects. However, it was appealing to experimentally determine if such a design is truly not worth pursuing, which was one of the objectives of this work.

2.3 Endothermic Hydrocarbon Fuels

2.3.1 Thermal and Catalytic Cracking

Significant research has gone into extending the heat sink capabilities of various fuels as a result of ongoing interest in hypersonic aircrafts. As the Mach number increases, the total heat load on the aircraft increases and air cooling becomes impossible, necessitating new thermal management techniques. Taking advantage of a fuels' heat sink capabilities is one of the most attractive options to accomplish this. While the heat sink capacity of a fuel such as liquid hydrogen is only due to its sensible heating and latent heat of vaporization, a hydrocarbon fuels' heat sink capacity can also come from endothermic decomposition reactions that take place.

However, due to the complex compositions of these multicomponent hydrocarbon fuels, the reactions that take place are difficult to control, and improper management can lead to undesired results. The most extreme example illustrating this is considering the equilibrium products of cracking, which are actually exothermic (methane and solid carbon). Thus, at high enough levels of conversion, the endothermicity of the fuel has been shown to reduce dramatically both in thermal cracking and cracking using certain catalysts. [53] [54] [55] [56] [57] Therefore, the total conversion must be closely considered, as well as reaction selectivity if a catalyst is used.

Dinda et al. [58] summarized and reviewed a large amount of research on this topic and found the range of the total heat sink capacity of various kerosene-type fuels was around 2500-3500 kJ/kg of fuel for a temperature range of 550-750°C and a pressure range of 25-60 bar. Additionally, they showed that the endothermic heat sink value for most fuels tested was in the range of 500-1100 kJ/kg. These values are much lower than the theoretical maximum (~3,500 kJ/kg) of most of these fuels if only olefins such as ethylene were produced through cracking. [53] Consequently, catalytic cracking of these fuels has also been investigated that improve olefin selectivity, resulting in additional increases in the total heat sink capability of the fuel as reviewed by Edwards [55] and Dinda et al. [58]. However, it remains to be seen whether the additional catalytic structures in the already narrow tubes would result in more harm than good considering catalyst fouling, coke build up, and eventual deactivation. These considerations are not only paramount for hypersonic aircraft, but also for the theoretical FIERA engine as the fuel needs to absorb a considerable amount of heat to reduce the compressor air temperature, in addition to any exhaust heat recuperated.

2.3.2 Coke Mitigation

As hydrocarbon fuels are heated, they begin to form thermal-oxidative deposits because of reactions with dissolved oxygen at temperatures close to 150°C. However, these deposits peak and then decrease as the dissolved oxygen is depleted for any physically realistic residence time at temperatures near 370°C. At roughly 500°C, pyrolytic deposits begin to form as a result of thermal cracking of the fuel. The production of these deposits increases with conversion, which is dependent on temperature, pressure, residence time, and fuel composition. Both oxidative and pyrolytic coke can form filamentous or amorphous coke deposits depending on the operating conditions. It has been shown that filamentous coke is very dependent on the wall material and the roughness of certain materials, and can be largely eliminated by coating the wall with an “inert” layer of material such as silica or alumina. Amorphous deposits are thought to be fairly independent of surface composition, and generally more difficult to mitigate. [59] [58] [60] [61]

Currently, the literature suggests that oxidative coking and pyrolytic coking can be reduced in a few ways. [58] [55] Thermal-oxidative deposits can be suppressed by reducing the oxygen concentration in the fuel, which can be partially achieved by purging the fuel with inert nitrogen gas. Pyrolytic coke formation is harder to prevent, but considerable research into various additives have shown significant reductions in coke formation. One such additive, successfully developed in the USAF JP8+100 thermal stability additive (TSA) program, increases the heat sink capacity of JP-8 by allowing the fuel temperature to rise by an additional 100°F without serious fuel degradation. [62] Coking has also been shown to decrease in specific catalyst coated reactors, though never completely eliminated. [63] [64] [65]

One reoccurring observation made across coking experiments with various test rigs, was that the worst coking problems occur downstream of the high temperature reactors, where the fuel cools to subcritical temperatures. This is attributed to the enhanced solubilities of coke and its precursors in supercritical fuels. [55] This would likely not be an issue in hypersonic aircraft or in a FIERA engine since the fuel is to be burned before significant cooling takes place, but it is an important consideration nonetheless if the system is cooled and reused numerous times.

2.3.3 Combustion of Cracked Hydrocarbon Fuels

The heat sink capacity is not the only parameter that needs to be optimized with regard to fuel cracking, as stable and efficient heat release is still the fuel’s primary purpose. In general, as the rate of conversion increases, the amount of smaller gaseous products increases, with a reduction in the larger hydrocarbons in liquid state. This, along with the elevated temperatures and pressures at which the pyrolysis products are injected into the combustor, creates a complex combustion scenario.

The gaseous hydrogen and alkenes produced have the benefit of short ignition delays and fast burning rates, while the larger aromatics generally have worse ignition and combustion characteristics. [66] The net effect that these more complex fuels have on combustion have been investigated substantially. Colket and Spadaccini [67], Castaldi et al. [68], and Puri et al. [69] have all shown reductions in ignition delay times for thermally cracked hydrocarbon fuels with various levels of conversion. Zhong and Peng [66] experimentally found that the laminar flame speed of thermally cracked RP-3 was greater than that of the original fuel. They also suggested that excessively thermally cracking endothermic hydrocarbon fuels is not advantageous for combustion characteristics as it was shown that the combustion characteristics mainly depend on the pyrolysis liquid products rather than the pyrolysis gaseous products. This further supports the idea that high fuel conversion (at least in thermal cracking) should be avoided as it also reduces the endothermic heat sink capacity of the fuel as previously discussed.

This is not necessarily the case for catalytic cracking, as the reaction selectivity of the catalyst can promote the production of more desirable products to a certain extent. However, catalyst fouling can eventually render them ineffective, which has led to research investigating the inclusion of dispersible nanostructured catalytic particles in the fuel itself. Sim et al. [70] showed how these additives can enhance conversion, ignition, and combustion of hydrocarbon fuels under supercritical conditions.

Both hypersonic aircraft and the FIERA engine would likely require the use of one of these methods. However, as can be seen, this requires precise tailoring of the system to not only obtain a maximally endothermic heat sink capacity, but also predictable and desirable combustion characteristics.

2.4 Contribution

The main goal of this work was to provide further insights into the FIERA engine that may support further development and/or expose potential failings of the system and modifications that may mitigate them. This was to be done through the experimental investigation of the average heat transfer coefficients of a single stator heat exchanger in relation to three independent variables. These results were used as a baseline in an effectiveness-NTU heat exchanger model for a full-scale, multistage-intercooled, axial compressor to determine the expected heat transfer. Combustion experiments with thermally enhanced fuel were also conducted to determine changes in emissions and combustion characteristics.

Chapter 3

Stator Heat Exchanger Experiments

3.1 Stator Heat Exchanger Experimental Approach

These experiments were designed to determine the average air heat transfer coefficient and overall heat transfer coefficient by using an energy balance and LMTD approach, respectively. Additionally, three variables were varied to determine which, if any, had a statistically significant effect on these outputs following Lawson and Erjavec's factorial design of experiments. [71] A single hollow stator was used as the heat exchanger such that hot air flows around the blade and liquid flows through the blade in a crossflow arrangement as shown in Figure 3.1. Water was chosen as a surrogate for jet fuel for these experiments for ease of use.

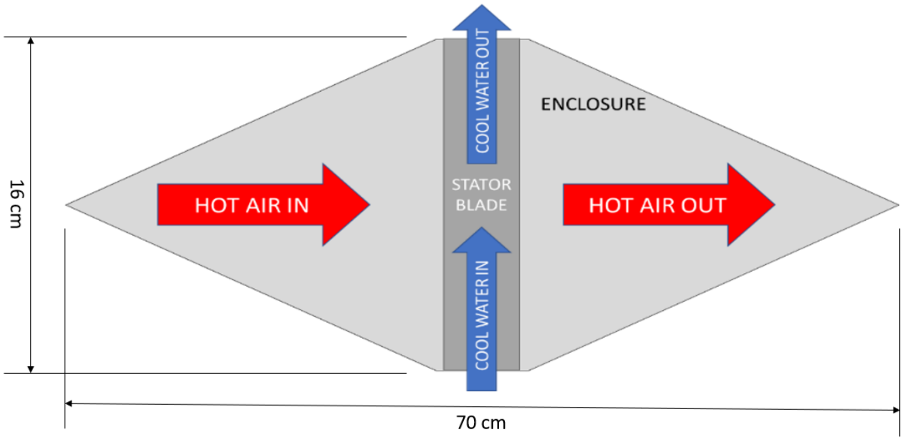

Figure 3.1: Crossflow stator heat exchanger layout

The amount of heat transferred ($\dot{Q}_c$) from the air to the water was calculated from an overall energy balance of the water as shown in Equation 3.1, where $\dot{m}_c$ is the mass flow rate of the water, $c_{p,c}$ is the specific heat of the water, and $T_{c,o}$ and $T_{c,i}$ are the outlet and inlet water temperatures, respectively. This was preferred instead of using an energy balance of the air since some of the heat lost from it would be transferred to the enclosure and surroundings as unaccountable waste heat, while all the heat transferred to the water essentially comes from the air flow over the stator heat exchanger.

The average air heat transfer coefficient over the blade was found using an average outer surface temperature of the blade shown in Equation 3.2 and an air free stream temperature shown in Equation 3.3. Equation 3.2 averages the surface temperatures on the upper and lower, and left and right sides of the blade (i.e., T_{UR}, T_{UL}, T_{LR}, and T_{LL}). Equation 3.3 approximates the air free stream temperature as if it were constant as the air passes over the stator with slightly more weight given to the entry temperature, as again some heat is lost to the enclosure between the two temperature measuring devices. This assumption allowed for the calculation of the average air heat transfer coefficient over the stator using Newton's law of cooling shown in Equation 3.4.

$$\dot{Q}_c = \dot{m}_c c_{p,c}\left(T_{c,o} - T_{c,i}\right) \tag{3.1}$$

$$\bar{T}_{surf} = \frac{T_{UR} + T_{UL} + T_{LR} + T_{LL}}{4} \tag{3.2}$$

$$T_\infty = \frac{\left(2T_{h,i} + T_{h,o}\right)}{3} \tag{3.3}$$

$$h_h = \frac{\dot{Q}_c}{A_o\left(T_\infty - \bar{T}_{surf}\right)} \tag{3.4}$$

The overall heat transfer coefficient was also to be found, but used the log mean temperature difference (LMTD) of the two fluids which could be calculated either for a parallel-flow heat exchanger or counterflow heat exchanger as shown in Equations 3.5-3.9. As this is a crossflow heat exchanger (i.e., the fluids move perpendicularly to one another), an average between the LMTD values is used in Equation 3.10. The heat gained by the water was again used in this equation, in addition to the average area (A_{avg}) of the internal and external surface area of the stator. This allowed for the calculation of an overall heat transfer coefficient (U) for our experimental system.

$$LMTD = \frac{\Delta T_A - \Delta T_B}{\ln\left(\frac{\Delta T_A}{\Delta T_B}\right)} \tag{3.5}$$

$$\Delta T_{A,parallel} = T_{h,i} - T_{c,i} \tag{3.6}$$

$$\Delta T_{B,parallel} = T_{h,o} - T_{c,o} \tag{3.7}$$

$$\Delta T_{A,counter} = T_{h,i} - T_{c,o} \tag{3.8}$$

$$\Delta T_{B,counter} = T_{h,o} - T_{c,i} \tag{3.9}$$

$$U = \frac{\dot{Q}_c}{A_{avg} LMTD_{avg}} \tag{3.10}$$

These values were calculated at different experimental conditions using a two-level factorial design of experiments, meaning each independent variable had a high (+) and low (-) level corresponding to a chosen value. Three independent variables were chosen for these experiments and therefore there were 2^3 unique runs or configurations as shown in Table 3.1. This method allows for the formulation of an empirical model of the form shown in Equation 3.11, relating the effects (E_1, E_2, E_3) and interactions (I_{12}, I_{13}, I_{23}, I_{123}) of the chosen variables (X_1, X_2, X_3) and the average output of all runs ($\bar{Y}$) to the predicted output (Y), which in this case are the heat transfer coefficients. The effects are calculated using Equation 3.12 and the interactions are calculated similarly using Equation 3.13 and Equation 3.14.

Table 3.1: Configuration list for 2^3 factorial design of experiments

Config.	X_1	X_2	X_2
1	+	+	+
2	+	+	−
3	+	−	+
4	+	−	−
5	−	+	+
6	−	+	−
7	−	−	+
8	−	−	−

$$Y = \bar{Y} + \frac{E_1}{2}X_1 + \frac{E_2}{2}X_2 + \frac{E_3}{2}X_3 + \frac{I_{12}}{2}X_1X_2 + \frac{I_{13}}{2}X_1X_3 + \frac{I_{23}}{2}X_2X_3 + \frac{I_{123}}{2}X_1X_2X_3 \tag{3.11}$$

$$E_i = \frac{1}{4}\left(\sum_{run=1}^{8} Y_{run}X_{i,run}\right) \tag{3.12}$$

$$I_{ij} = \frac{1}{4}\left(\sum_{run=1}^{8} Y_{run}X_{i,run}X_{j,run}\right) \tag{3.13}$$

$$I_{ijk} = \frac{1}{4}\left(\sum_{run=1}^{8} Y_{run}X_{i,run}X_{j,run}X_{k,run}\right) \tag{3.14}$$

Two sets of replications were also conducted so that the statistical significance of the effects and interactions could be determined using the signal-to-noise t-ratio (t_E). First, the sample variance was calculated for each configuration using Equation 3.15, where n is the number of replications (or observations), Y_i is the value of one observation, $\bar{Y}$ is the mean value of all observations, and σ_j^2 is the sample variance for the jth configuration. The degrees of freedom for each configuration (ν_j) and pooled degrees of freedom (ν_P) were calculated using Equation 3.16 and Equation 3.17, respectively, which were used to calculate the pooled variance (σ_P^2) using Equation 3.18, where m is the total number of configurations. The standard error (S_E) was then calculated using Equation 3.19, where n_F is the number of factorial points (or simply the total number of data points). Finally, the signal-to-noise t-ratio was found for each effect or interaction as shown in Equation 3.20. This value could then be compared to the critical t-value (t^*) obtained using the two-tail Student's t-distribution, which is determined using the total degrees of freedom, and a chosen confidence level. The effects or interactions that resulted in t-ratios greater than the t^* value could thus be considered significant.

$$\sigma_j^2 = \frac{1}{m-1}\left(\sum_{i=1}^{n}(Y_i - \bar{Y})^2\right) \tag{3.15}$$

$$\nu_j = n - 1 \tag{3.16}$$

$$\nu_P = \sum_{j=1}^{m} \nu_j \tag{3.17}$$

$$\sigma_P^2 = \sum_{j=1}^{m} \nu_j\sigma_j^2 \Big/ \nu_P \tag{3.18}$$

$$S_E = \frac{2\sigma_P}{\sqrt{n_F}} \tag{3.19}$$

$$t_E = \frac{E\ or\ I}{S_E} \tag{3.20}$$

3.2 Input Variables and Output Parameters for Stator Heat Exchanger Experiments

Three independent variables were chosen for these experiments: air mass flow rate (X_1), water mass flow rate (X_2), and air inlet temperature (X_3). A "high" and "low" level were selected for each of these variables and their coded experimental values are shown in Table 3.2. Though it was desired to test with experimental conditions as similar to those experienced in full scale, modern axial compressors, facility and equipment limitations made this difficult. Notwithstanding, the values chosen function for the purposes of this preliminary investigation of the stator heat exchanger. While the "high" levels for the air mass flow rate and air inlet temperature were set at the limits of the system, the levels of the water mass flow rate were chosen with the full-scale version in mind. This essentially means that if a set value of air was flowing over one stator in a compressor stage, there would be a corresponding amount of fuel that could flow through the stator that is determined by the stoichiometric ratio at which the combustor burns. For this reason, the mass flow rate of water was chosen such that in some experimental configurations the "fuel"-air equivalence ratio would be slightly lean ($\phi < 1$) and in other configurations would be slightly rich ($\phi > 1$). This is shown in Table 3.3.

The heat capacity rate ratio is another metric that can be compared when considering the similarity to real engine operating conditions. As calculated and further discussed in Chapter 4, modern turbofan engines at cruise have very low heat capacity rate ratios (~0.03), while the heat capacity rate ratios under the tested experimental conditions are significantly larger as shown in Table 3.3. This was due in part by the higher specific heat of water than of jet fuel, and the still fairly low air-fuel ratios. More similar experimental conditions were difficult to obtain due to system limitations. Additionally, the water flow rate could not be reduced significantly without increasing the likelihood of boiling occurring in the stator, which would affect the calculated heat transfer coefficients. This is further discussed in the results.

As stated in the previous section, the output parameters from these experiments were the average air heat transfer coefficient (h_h) and the overall heat transfer coefficient (U). These values are dependent on some intermediate outputs, namely fluid temperatures, mass flow rates, and stator surface temperatures as previously described.

Table 3.2: Input variables' experimental values corresponding to "high" and "low" levels

Independent Variables	Levels	
	$-$	$+$
Air Inlet Temperature (X_1) [°C]	150	210
Air Mass Flow Rate (X_2) [SLPM]	900	1050
Water Mass Flow Rate (X_3) [mL/min]	50	100

Table 3.3: Experimental configuration air-fuel ratio (AFR), fuel-air ratio (FAR), fuel-air equivalence ratio (ϕ), and heat capacity rate ratio (C_r)

	$X_2 = "-"$				$X_2 = "+"$			
	AFR	FAR	ϕ	C_r	AFR	FAR	ϕ	C_r
$X_3 = "-"$	22	0.045	0.71	0.18	26	0.039	0.61	0.16
$X_3 = "+"$	11	0.091	1.4	0.38	13	0.078	1.21	0.33

3.3 Facility and Data Acquisition for Stator Heat Exchanger Experiments

Figure 3.2 shows the overall P&ID for the experiment and Figures 3.3 and 3.4 show detail views of the enclosure and heating array, respectively. Air was supplied to the laboratory from an air-compressor and mass flow rate was measured and controlled using a mass flow meter (with a maximum of 1000 SLPM), needle valve, and a mass flow controller (with a maximum of 500 SLPM). The air was then heated in an array of gas heaters after which, it entered the enclosure housing the hollow stator blade. The air passes over the blade and is then exhausted into the fume hood. A gear pump was used to pump water from the reservoir, through the stator, and out to a waste container.

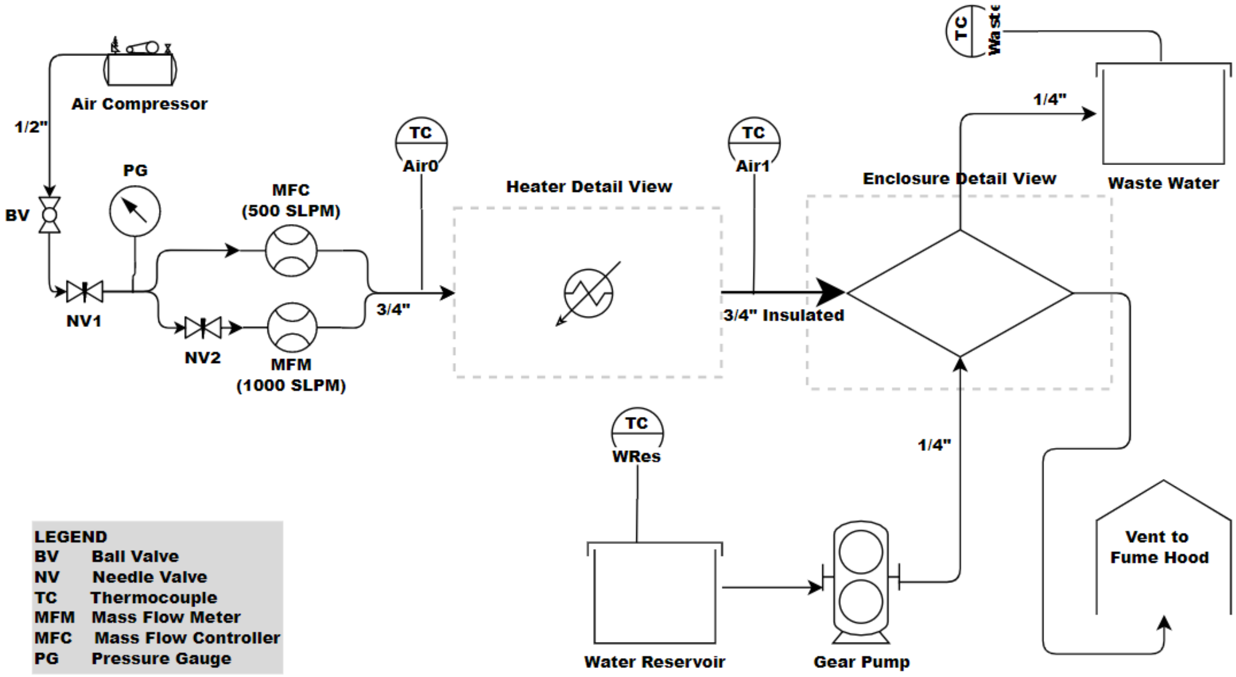

Figure 3.2: P&ID of the stator heat exchanger experiments

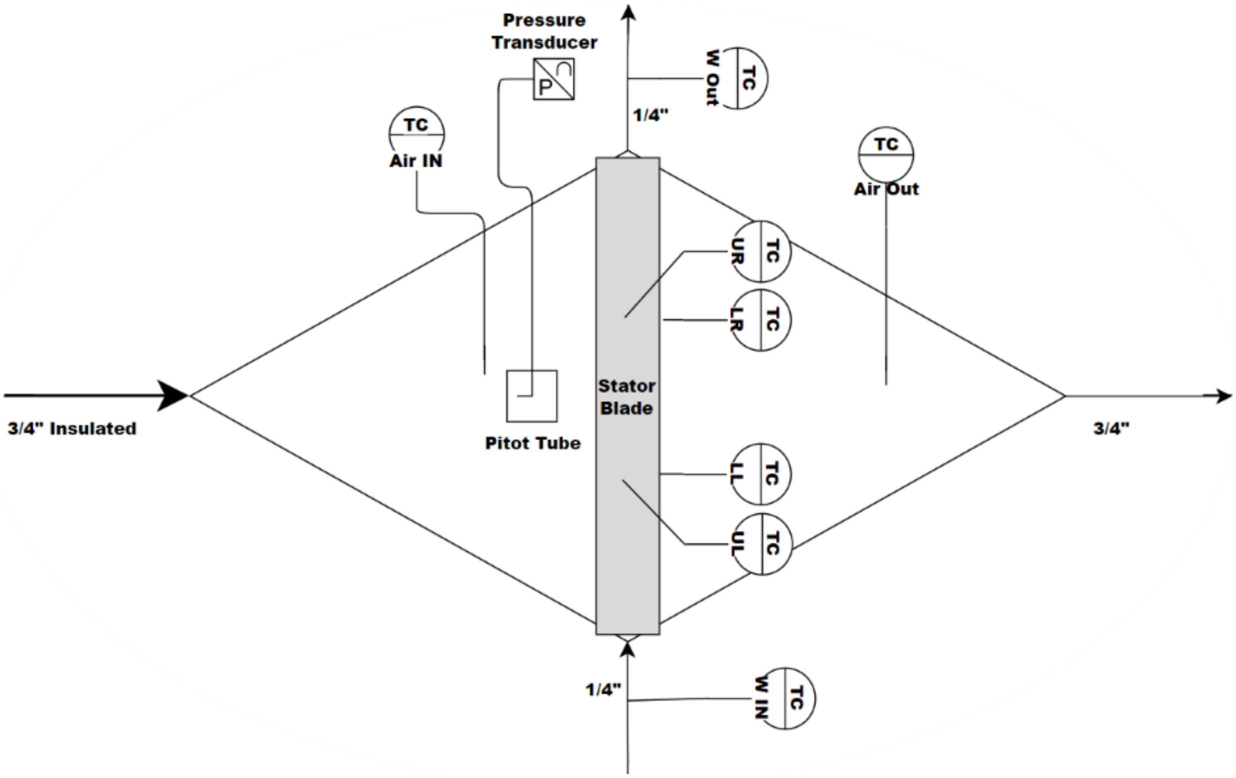

Figure 3.3: Enclosure detail view

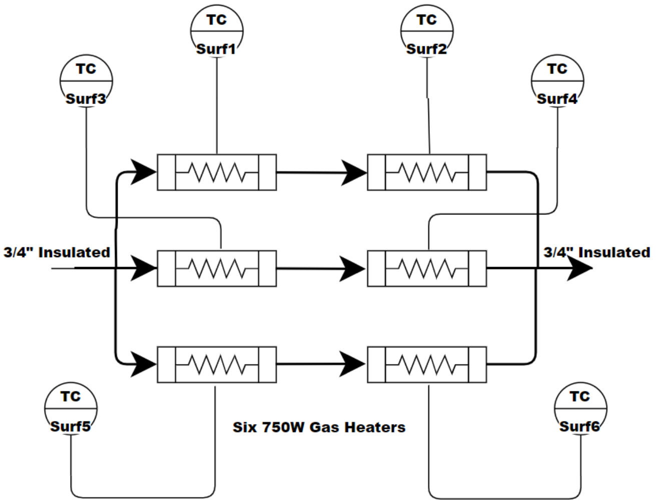

Figure 3.4: Heating Array detail view

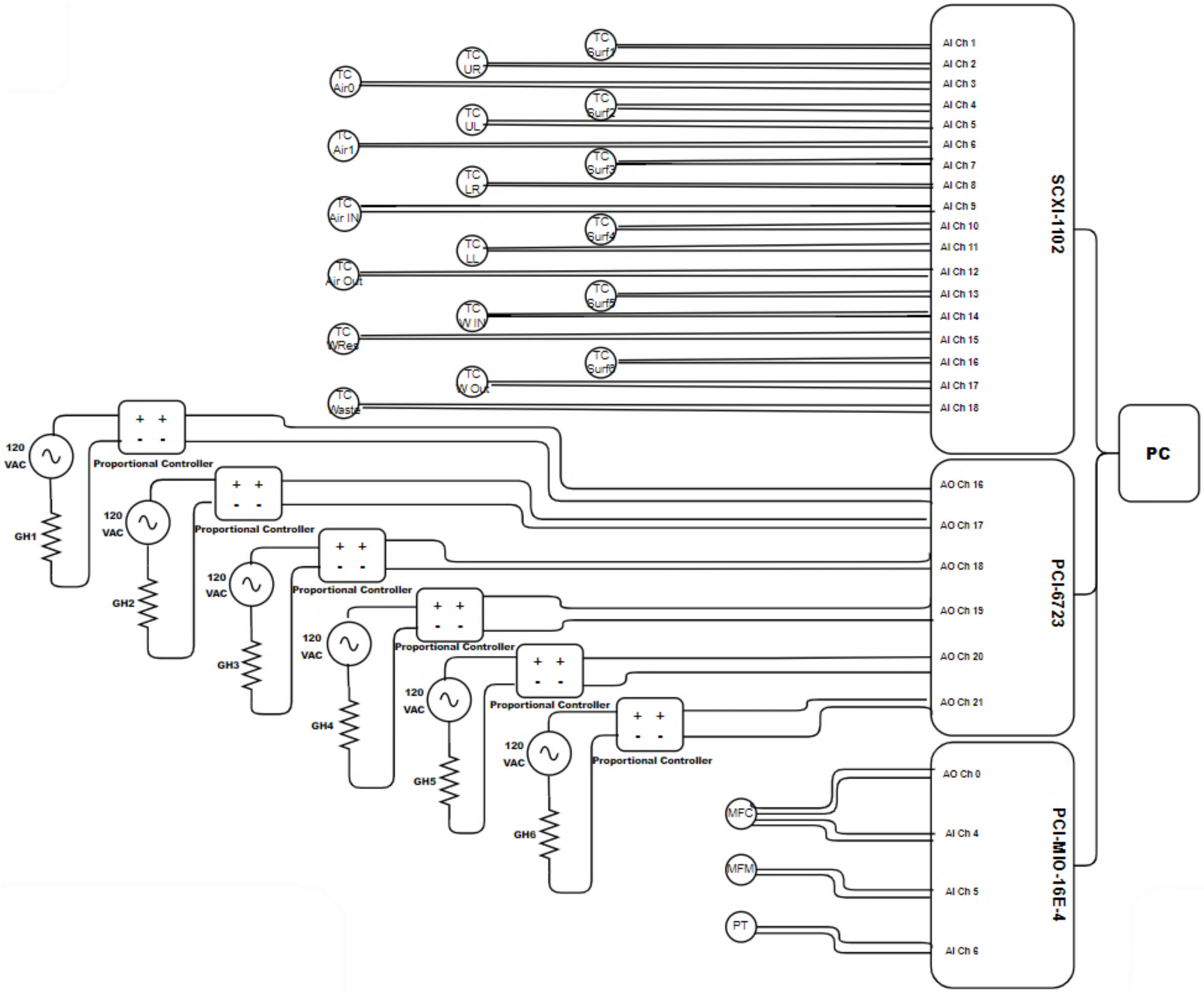

Figure 3.5: Wiring diagram for the stator heat exchanger experiments

Measurement and control systems were connected to a data acquisition PC via National Instruments (NI) hardware (SCXI-1001 chassis with three modules) as shown in Figure 3.5 and was operated using NI LabVIEW software. All temperature measurements were taken with 1/16" or 1/32" sheathed K-type thermocouples except for the stator surface temperatures, which were taken with four self-adhesive K-type thermocouples, placed equidistant from the stator ends and each other. Only the outputs of the thermocouples shown in Figure 3.3 were used in the data reduction, while the others were used simply to monitor the system.

An Aalborg GFM77 mass flow meter and an Aalborg GFC67 mass flow controller were used to monitor air flow. The feedback voltage signals from both instruments were converted to SLPM in LabVIEW virtual instrument (VI) and the desired total SLPM of airflow was maintained for the different experimental conditions. The mass flow controller was similarly controlled using output control voltages from the LabVIEW VI. A pressure gauge was placed before the mass flow meter and mass flow controller to provide the same inlet air pressure and maintain repeatability for all experiments.

The heater array consisted of six 750 W Omega T-type in-line gas heaters with 1/32" K-type thermocouples wrapped around the outer surface of each heater to ensure maximum operating temperatures were not exceeded. The array and subsequent piping were covered with fiber glass insulation to minimize heat loss as shown in Figure 3.6. Each heater was controlled manually from 0 to 100% by a proportional controller (Crydom MCPC-1225) using a 0-5 VDC control voltage from the NI PCXI 6723 module so that the desired air temperature was reached.

Figure 3.6: Heater array

Room temperature water was pumped from a closed container to the stator blade using a Cole-Parmer model 75211-30 gear pump and a model L22097 pump head. Mass flow rate calibration was conducted before experiments using a digital scale and timer.

The enclosure was made from 3/16” mild steel sheet metal. The pieces were cut with an OMAX Water Jet, welded together, and painted for corrosion resistance. The lid was made to be removable to enable access to the inside but can be clamped into place and has a rubber gasket to reduce leakage. A hole was also drilled in the lid to enable insertion of a pitot tube in front of the stator. A Setra-239 pressure transducer was used to measure the dynamic pressure for air speed calculations at the stator and was calibrated using a Dwyer Series 475 Mark III digital manometer. The enclosure dimensions at the stator are listed in Table 3.4.

The stator has a NACA 6412 blade profile, and its dimensions are listed in Table 3.5. This airfoil shape was chosen since similarly shaped blades are commonly used in axial compressors, and it also has a large cross-sectional area compared to double circular arc blades, which is another common blade type. [5] Stainless steel was chosen as the material for the blade as it is still employed in the early compressor stages of some engines. Additionally, it has a thermal conductivity of 16.2 W/m-K, which is very similar to the now more predominantly used titanium and nickel superalloy blades with thermal conductivities of roughly 20 W/m-K. [72] [73] Thus, this experiment would likely extend to experiments with those materials. Although the preferred manufacturing method for this single hollow stator would have been some form of additive manufacturing, such as laser metal deposition, monetary costs made this unfeasible. Therefore, 22 gauge, 304 grade, stainless steel was cut in two pieces, bent into the correct shape using a 3D printed mold, and connected using high-temperature metal-reinforced epoxy.

Table 3.4: Stator dimensions

Height [m]	0.0445
Width [m]	0.161
Cross-Sectional Area [m^2]	0.00716

Table 3.5: Enclosure properties at the stator

Span Length [m]	0.161
Chord [m]	0.041
Wall Thickness [m]	0.00076
Inner Wetted Perimeter [m]	0.062
Inner Cross-Sectional Area [m^2]	0.000075
Inner Surface Area [m^2]	0.00998
Outer Surface Area [m^2]	0.0132
Average Surface Area [m^2]	0.0116
Max Camber [% of chord]	6
Distance to Max Camber from Leading Edge [% of chord]	40
Max Thickness [% of chord]	12
Blade Profile	NACA 6412

Figure 3.8 shows the linkage to connect the stator to the enclosure, which consists of a few components that hold the stator in place and connect it to the piping. The round piece that connects to the stator was manually turned from stainless steel stock and an NPT fitting was welded on. The upper and lower clamps, which screw together (holding the round piece in place), were manually and CNC milled from mild steel stock. Rotary union joints were used to allow the stator to rotate and change its pitch. The pitch was set at +10° for all experiments as shown in Figure 3.7, corresponding roughly to a 0° incidence angle with the inlet air. The enclosure and stator assembly are shown in Figure 3.9.

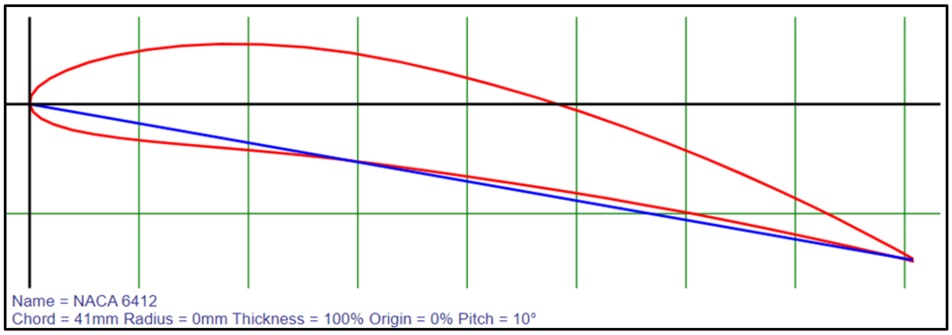

Figure 3.7: NACA 6412 blade profile with +10° pitch [74]

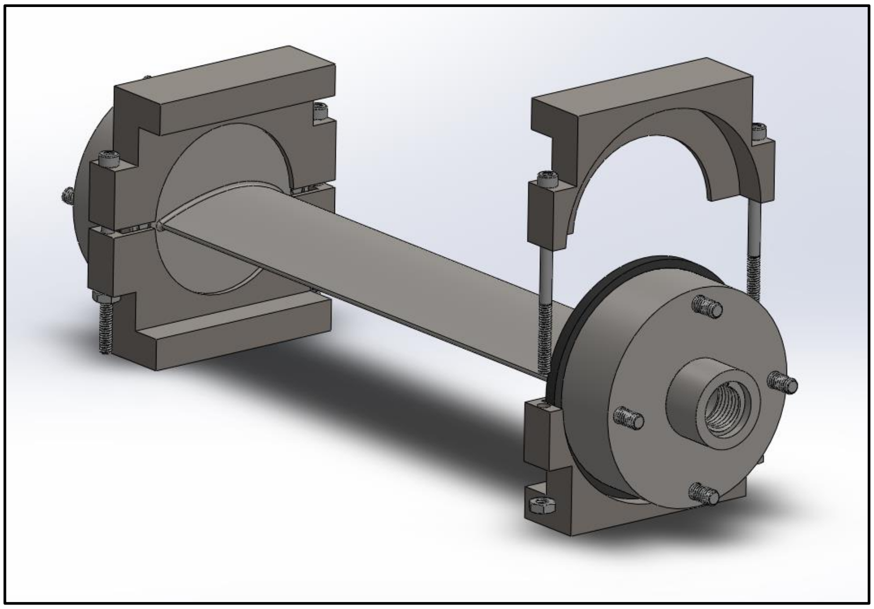

Figure 3.8: Linkage between stator and enclosure

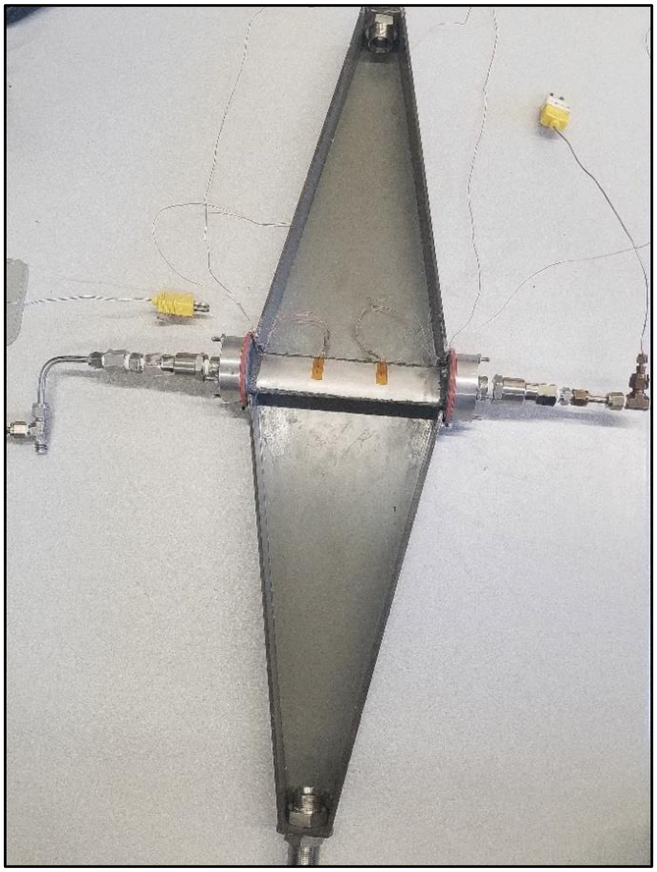

Figure 3.9: Enclosure and stator heat exchanger assembly

3.4 Stator Heat Exchanger Experimental Procedure

The stator was placed in the enclosure housing such that it had a +10° pitch. The lid was put in place and the component holding the stator and lid in position was tightened. Additional clamps were put in place between the lid and enclosure base to reduce air leakage. The water reservoir was filled, and subsystems were turned on. The air supply was opened, and inlet pressure was set to 70 psig. The air flow through the mass flow meter was set to 600 SLPM using the needle valve and the air flow through the mass flow controller was changed from around 300 SLPM to roughly 450 SLPM depending on the configuration being tested and the total air flow desired. The gear pump was turned on and set to the appropriate flow level for the chosen configuration as well. The control voltage to the gas heaters were increased over the course of five to ten minutes to obtain the proper air temperature right before the stator, and minor adjustments were made during the next ten minutes to ensure steady state values were obtained. After this period, and when values seemed to have stabilized, the displayed values on the LabVIEW VI were recorded. As mentioned previously, eight configurations were tested a total of three times using a factorial design of experiments. The run order for the configurations in each set of replications was randomized to reduce the effect of process drift and this order is shown in Table 3.6.

Table 3.6: Experimental run order for stator heat exchanger experiments

	Coded Levels			Experimental Values			Run Order		
Config.	Air Temp (X_1)	Air Flow (X_2)	Water Flow (X_3)	Air Temp (°C)	Air Flow (SLPM)	Water Flow (mL/min)	Data Set 1	Data Set 2	Data Set 3
1	−	−	−	150	900	50	1	5	8
2	−	−	+	150	900	100	6	7	4
3	−	+	−	150	1050	50	4	4	6
4	−	+	+	150	1050	100	8	1	3
5	+	−	−	210	900	50	5	6	5
6	+	−	+	210	900	100	3	3	7
7	+	+	−	210	1050	50	7	2	1
8	+	+	+	210	1050	100	2	8	2

3.5 Stator Heat Exchanger Results and Discussion

Using the factorial design of experiments and the heat transfer approach explained in Section 3.1, two empirical equations relating the average air heat transfer coefficient and the overall heat transfer coefficient to three independent variables was created.

The average air heat transfer coefficient (h_h) was calculated for each run of each configuration and the results are shown in Table 3.7. The effects and interactions of the three variables were calculated and the results are shown in Table 3.8. Their statistical significance was checked by comparing the signal-to-noise (SNR) t-ratio to the critical t-value using the two-tail Student's t-distribution. This required the calculation of the pooled standard deviation, the total degrees of freedom, and the standard error, which are tabulated in Table 3.9. In these experiments, the total degrees of freedom was 16 and the 95% confidence interval was chosen, which resulted in a critical t-value of 2.120. Thus, effects or interactions with SNR t-ratios greater than that critical t-value could be considered significant, as shown in Table 3.10, and a reduced empirical equation relating the statistically significant inputs to the output is shown in Equation 3.21.

Table 3.7: Calculated values of the average air heat transfer coefficient (h_h) across the stator in W/m^2-K for each run of each configuration

Config.	Air Temp (X_1)	Air Flow (X_2)	Water Flow (X_3)	Data Set 1	Data Set 2	Data Set 3	Average
1	−	−	−	131.3	114.9	131.3	125.8
2	−	−	+	110.7	129.8	143.4	128.0
3	−	+	−	125.5	123.2	125.5	124.8
4	−	+	+	130.9	129.5	152.9	137.8
5	+	−	−	113.9	114.3	138.5	122.2
6	+	−	+	129.8	120.7	133.8	128.1
7	+	+	−	122.4	137.4	139.2	133.0
8	+	+	+	155.0	158.9	167.7	160.6
				Pooled Average			132.5

Table 3.8: Calculated effects and interactions of the three independent variables on the average air heat transfer coefficient (h_h)

	X_1	X_2	X_3	X_1X_2	X_1X_3	X_2X_3	$X_1X_2X_3$
E_i or I_{ij} or I_{ijk}	6.883	12.976	12.153	8.618	4.579	8.140	2.709

Table 3.9: Statistical values from the average air heat transfer coefficient (h_h) results

Pooled Standard Deviation (σ_P)	Total Degrees of Freedom (ν_P)	Standard Error (S_E)
10.63	16	4.341

Table 3.10: SNR t-ratios of the effects and interactions and their statistical significance on the average air heat transfer coefficient (h_h)

	X_1	X_2	X_3	X_1X_2	X_1X_3	X_2X_3	$X_1X_2X_3$
SNR t-ratio	1.586	2.989	2.800	1.985	1.055	1.875	0.624
Statistically significant at 95%?	NO	YES	YES	NO	NO	NO	NO

$$h_h = 132.5 + 6.5X_2 + 6.1X_3 \quad \left[\frac{W}{m^2K}\right] \tag{3.21}$$

The air heat transfer coefficient can also be represented more generally by its corresponding nondimensional number (Nusselt number). Using the chord length of the stator as the characteristic length and the value of the calculated average heat transfer coefficient, the experimentally obtained air Nusselt number is calculated to be 146.8.

The same statistical DOE was followed for the overall heat transfer coefficient (U), and the calculated value in each trial is shown in Table 3.11. The effects and interactions were again determined, along with the pooled standard deviation, total degrees of freedom, and standard error tabulated in Table 3.12 and 3.13, respectively. Lastly, the SNR t-ratios were calculated, and it was found that only the water mass flow rate had a statistically significant effect on the overall heat transfer coefficient at the 95% confidence interval, as shown in Table 3.14. The simplified empirical equation for this output is shown in Equation 3.22.

Table 3.11: Calculated values of the overall heat transfer coefficient (U) across the stator in W/m^2-K for each run of each configuration

Config.	Air Temp (X_1)	Air Flow (X_2)	Water Flow (X_3)	Data Set 1	Data Set 2	Data Set 3	Average
1	$-$	$-$	$-$	114.2	85.60	100.1	99.95
2	$-$	$-$	$+$	102.0	100.4	103.7	102.0
3	$-$	$+$	$-$	116.9	89.58	90.37	98.95
4	$-$	$+$	$+$	117.7	94.02	109.8	107.2
5	$+$	$-$	$-$	105.7	93.23	104.1	101.0
6	$+$	$-$	$+$	111.5	91.33	100.5	101.1
7	$+$	$+$	$-$	104.5	101.2	99.38	101.7
8	$+$	$+$	$+$	141.6	122.4	121.1	128.4
				Pooled Average			105.0

Table 3.12: Calculated effects and interactions of the three independent variables on the overall heat transfer coefficient (U)

	X_1	X_2	X_3	X_1X_2	X_1X_3	X_2X_3	$X_1X_2X_3$
E_i or I_{ij} or I_{ijk}	6.022	8.012	9.260	5.961	4.114	8.180	5.122

Table 3.13: Statistical values from the overall heat transfer coefficient (U) results

Pooled Standard Deviation (σ_P)	Total Degrees of Freedom (ν_P)	Standard Error (S_E)
10.49	16	4.282

Table 3.14: SNR t-ratios of the effects and interactions and their statistical significance on the overall heat transfer coefficient (U)

	X_1	X_2	X_3	X_1X_2	X_1X_3	X_2X_3	$X_1X_2X_3$
SNR t-ratio	1.406	1.871	2.163	1.392	0.961	1.910	1.196
Statistically significant at 95%?	NO	NO	YES	NO	NO	NO	NO

$$U = 105.0 + 4.63X_3 \quad \left[\frac{W}{m^2K}\right] \tag{3.22}$$

A few conclusions can be made from these results. First, the average air heat transfer coefficient was found to be almost equally affected by the water mass flow rate as by the air mass flow rate. However, this equation is potentially misleading as these are based on the range of the chosen input values, and while the water mass flow rate was doubled from 50 mL/min to 100 mL/min, the air flow was only varied from 900 SLPM to 1050 SLPM. This suggests that while the water does have a statistically significant effect on the average air heat transfer coefficient, doubling the air mass flow rate would likely have more of an impact than doubling the water flow. This is expected as convection correlations are predominantly made using only a combination of the Reynolds number and Prandtl number of the fluid in question (i.e., the air). Nevertheless, the reason for the inclusion of the effect of the water on the average air heat transfer coefficient is likely due to a change in surface thermal conditions. This is also consistent with the observations made by Ito et al. [49], that the average air Nusselt number over an airfoil heat exchanger can vary greatly even at the same, or very similar air Reynolds numbers, due to changes in the refrigerant flow rate.

The overall heat transfer coefficient results were similar, but only the water mass flow was found to be statistically significant, although the effect of the air mass flow and their combined interaction were the next SNR t-ratios near the critical t-value cutoff. Regardless, the average value over all the experiments for U was found to be 105 W/m^2-K.

Overall, these experiments had a few sources of error that ultimately affected the results. The first one was that there were a few minor air leaks in the enclosure, specifically at the linkage that secured the stator into the enclosure. These were reduced as much as possible before the experiments took place, but accurate quantification was not possible. The thermocouples for the air temperatures in the enclosure were also inserted into the flow as close to the same position for all experiments, but some displacement was unavoidable between all the runs. Likewise, the stator was kept as close to the same orientation in the enclosure, but a small tilt between data sets when the enclosure was opened and equipment inspected, could have caused some change in the flow, and consequently the heat transfer results. Another factor that may have affected the results was the potential presence of boiling in the stator, particularly in configuration 5 and 7, where water exit temperatures reached approximately 70°C. This scenario was not as likely in the other configurations where exit temperatures were 50°C or less. Another contributor to the error in the system was the amount of heat from the air lost to the environment.

While the heat transfer rate to the water varied from approximately 100W to 200W depending on the configuration, the heat transfer rate from the air was between approximately 200W and 600W, making the heat transferred to the water about a third of the heat lost by the air.

The final component of these experiments that was considered after post processing, was the determination if the experimental heat transfer coefficients obtained would match those calculated using a few chosen Nusselt number correlations. The Reynolds number and Prandtl number were required for these correlations and were determined at the experimental conditions. The air speed (u_h) was calculated using Equation 3.23, which involves the dynamic pressure, or the difference between the stagnation pressure (P_0) and static pressure (P_s) and the air density (ρ_h). The dynamic pressure was found using the averaged output of the pressure transducer (connected to the stagnation and static ports of the pitot tube) in each respective configuration. The air Reynolds number ($Re_{chord,h}$) was calculated using the air speed and kinematic viscosity of the air (ν_h), and chord length (c) as the characteristic length, as shown in Equation 3.24. The air properties were evaluated at the air temperature before the stator (either 150°C or 210°C) and the inlet static pressure of 70 psig, although the actual pressure in the enclosure was likely lower than this. These values are shown in Table 3.15 along with the air Prandtl numbers (Pr_h).

$$u_h = \sqrt{\frac{2(P_0 - P_s)}{\rho_h}} \tag{3.23}$$

$$Re_{chord,h} = \frac{u_h c}{\nu_h} \tag{3.24}$$

Table 3.15: Air properties at experimental conditions

	$X_2 = "-"$		$X_2 = "+"$	
$\dot{m}_h$[kg/s]	0.0184		0.0214	
	$X_1 = "-"$	$X_1 = "+"$	$X_1 = "-"$	$X_1 = "+"$
u_h [m/s]	3.83	4.39	4.14	4.67
$Re_{chord,h}$ [×10^4]	3.10	2.84	3.35	3.02
Pr_h	0.699	0.699	0.699	0.699

The air Reynolds number was found to be much lower than the critical Reynolds number for external flow over a flat plate (5×10^5). Therefore, a Nusselt number correlation for laminar flow over a flat plate was chosen from [72] and is shown in Equation 3.25. While this equation calls for the properties to be evaluated at the film temperature to help account for the effect of variable properties, the free stream air temperature was used for simplicity to get a rough calculation of the air heat transfer coefficient at the different experimental configurations. Equation 3.26 shows the average air heat transfer coefficient ($\bar{h}_h$) that was calculated using the average air Nusselt number ($\overline{Nu}_h$), chord length (c), and thermal conductivity of the air (k_h). These results are presented in Table 3.16.

The air heat transfer coefficients calculated were found to be significantly lower than those experimentally obtained by roughly 40 W/m^2-K, resulting in a mean average error between the model and experiments of 42%. This large discrepancy is likely due to some of the sources of error previously mentioned but could also be the result of an improperly chosen Nusselt number correlation as the roughness of the leading edge of the stator may trip the laminar flow through the enclosure, thus inducing turbulence, resulting in a larger heat transfer coefficient. Nevertheless, it should also be noted that the values only change slightly with the change in air mass flow rate (X_2) similar to the experimental results, although to a lesser extent. These values also suggest that the air temperature affects the heat transfer coefficient as much as the air mass flow rate contrary to the experimental results.

$$\overline{Nu}_h = 0.664 Re_{chord,h}^{1/2} Pr_h^{1/3} \tag{3.25}$$

$$\bar{h}_h = \frac{\overline{Nu}_h k_h}{c} \tag{3.26}$$

Table 3.16: Air heat transfer coefficient approximations using Nusselt number correlations

	$X_2 = "-"$		$X_2 = "+"$	
	$X_1 = "-"$	$X_1 = "+"$	$X_1 = "-"$	$X_1 = "+"$
$\overline{Nu}_h$	103.8	99.3	107.8	102.4
$\bar{h}_h$ [W/m^2-K]	88.6	94.2	92.1	97.2

In order to approximate the overall heat transfer coefficient at the different experimental conditions, the heat transfer coefficient of the water first had to be found using the same approach as was used for the air. The water speed (u_c) was calculated using Equation 3.27, where $\dot{V}_c$ is the volumetric flow rate of water and $A_{i,c/s}$ is the inner cross-sectional area of the stator. The water Reynolds number ($Re_{D_h,c}$) was calculated using the water speed and kinematic viscosity of the water (ν_c), and hydraulic diameter of the stator (D_h) as the characteristic length, as shown in Equation 3.28. The water properties were evaluated at an average temperature of 40°C. These values are shown in Table 3.17 along with the water Prandtl numbers (Pr_c).

$$u_c = \frac{\dot{V}_c}{A_{i,c/s}} \tag{3.27}$$

$$Re_{D_h,c} = \frac{u_c D_h}{\nu_c} \tag{3.28}$$

Table 3.17: Water properties at experimental conditions

	$X_3 = ” - “$	$X_3 = ” + ”$
$\dot{m}_c$ [kg/s]	0.00083	0.0017
u_c [m/s]	0.011	0.022
$Re_{D_h,c}$	80	160
Pr_c	4.50	4.50

The water Reynolds number was found to be much lower than the critical Reynolds number for internal flows (2300). Therefore, a laminar Nusselt number correlation was chosen from [72]. Due to the irregular geometry of the channel in the stator, an approximation was made to a rectangular cross section with an aspect ratio of 8:1. The Nusselt number was then averaged between the Nusselt numbers for a constant heat flux condition and a constant surface temperature condition as shown in Equation 3.29 and 3.30, respectively. Equation 3.31 shows the water heat transfer coefficient (h_c) that was calculated using the water Nusselt number (Nu_c), hydraulic diameter (D_h), and thermal conductivity of the water (k_c). These results are presented in Table 3.18. As can be seen, the calculated water heat transfer coefficients did not change with a change in the water flow rate due to the Nusselt number correlation chosen.

$$Nu_c = 6.49 \tag{3.29}$$

$$Nu_c = 5.60 \tag{3.30}$$

$$h_c = \frac{Nu_c k_c}{D_h} \tag{3.31}$$

Table 3.18: Water heat transfer coefficient approximations using Nusselt number correlations

	$X_3 = ” - “$	$X_3 = ” + ”$
Nu_c	6.05	6.05
h_c [W/m^2-K]	790.9	790.9

Nevertheless, an approximated overall heat transfer coefficient (U) was calculated using the approximated air and water heat transfer coefficients, as well as the inner surface area (A_i), outer surface area (A_o), average surface area (A_{avg}), stator wall thickness (t_{wall}), and wall conductivity (k_{wall}) as shown in Equation 3.32. The approximated U values under the different experimental conditions are tabulated in Table 3.19. These values of U match fairly closely to the experimentally obtained overall heat transfer coefficients with a mean average error of 14% and similarly change slightly when subjected to the different experimental conditions. However, as a whole, both the air and overall heat transfer coefficients obtained using the chosen correlations fail to match what was experimentally determined to have the most significant effect on these values (i.e., the air and water flow rates for $\bar{h}_h$ and the water flow rate for U).

$$\frac{1}{UA_{avg}} = \frac{1}{\bar{h}_h A_o} + \frac{t_{wall}}{k_{wall} A_{avg}} + \frac{1}{h_c A_i} \tag{3.32}$$

Table 3.19: Overall heat transfer coefficient approximations using Nusselt number correlations

	$X_3 = "-"\ or\ "+"$			
	$X_2 = "-"$		$X_2 = "+"$	
	$X_1 = "-"$	$X_1 = "+"$	$X_1 = "-"$	$X_1 = "+"$
U [W/m^2-K]	88.0	92.8	91.0	95.3

Chapter 4

Stator Heat Exchanger Model

4.1 Stator Heat Exchanger Model Approach

This section aimed to find the expected air and fuel exit temperatures of a full-scale, multistage-intercooled, axial compressor using three effectiveness-NTU models. For this to be accomplished, a compressor configuration needed to be specified enabling the calculation of the necessary values at each stage in the compressor. Two compressor configurations were considered, and their characteristic values are shown in Table 4.1.

Compressor Design #1 was made as a proxy for a GE90 engine and was created around its cruise design point. [11] [75] This means it has a 3-stage LPC, a 10-stage HPC, and an overall pressure ratio (OPR) of 38.9. Additionally, the inlet total temperature and inlet total pressure were evaluated at cruise conditions (altitude of 35,000 ft), and an inlet Mach number of 0.7 was chosen. Compressor Design #2 was made as a proxy for a higher pressure ratio engine like the GE9x with an 11-stage HPC and an OPR of 60. However, due to limited publicly available information of this engine, the same air mass flow rate, rotor angular velocities, and LPC were used in this second configuration.

The values of the inlet flow angle, diffusion factor, solidity, polytropic efficiency, and approximate stator loss coefficient were all chosen using reasonable values as described in [4]. An accompanying mean-line design program called Compressor Preliminary Design Program (COMPR) was used for the evaluation of the properties at each stage, and the inlet flow angle and diffusion factor were iteratively changed until the desired OPR was reached. This program also enabled quick calculation of the conditions in each compressor stage as well as the conditions within the stage itself (i.e., before and after the rotor and stator), in addition to blade dimensions and blade quantity. This crucially enabled the calculation of the surface areas used in the heat exchanger models.

The output values for the LPC are shown in Table 4.2. The values of total temperature ($T_{t,3m,f}$), total pressure ($P_{t,3m,f}$), and Mach number ($M_{3m,f}$) after the final stator row, are the values used as the inlet conditions for HPC #1 and HPC #2. Since the temperatures in the three stages of the LPC at the cruise conditions were found to be lower or roughly equal to any realistic initial fuel temperature, only the HPCs were chosen to be modeled with integrated stator intercooling as will be discussed in Section 3.2.2.

Figure 4.1 shows the stage nomenclature with station 1, station 2, and station 3 referring to the properties before the rotor, before the stator, and after the stator, respectively. Figure 4.2 shows a rotor blade-disk structure and associated nomenclature with the relevant variables being r_h, r_t, and r_m, representing the hub radius, tip radius, and mean radius. These values were used for the surface area estimation of the blades.

Table 4.1: Compressor conditions and configurations

	Compressor Design #1		Compressor Design #2	
Compressor Type	LPC	HPC #1	LPC	HPC #2
Number of Stages	3	10	3	11
Air Mass Flow Rate $\dot{m}_{h,tot}$ [kg/s]	71	71	71	71
Rotor Angular Velocity ω [rad/s]	247	977	247	977
Inlet Total Pressure $P_{t,i}$ [kPa]	24	64.97	24	64.97
Inlet Total Temperature $T_{t,i}$ [K]	218	299.1	218	299.1
Inlet Flow Angle α_1 [deg]	35	35	35	40
Inlet Mach Number M_1	0.7	0.583	0.7	0.583
Diffusion Factor D	0.4	0.51	0.4	0.54
Solidity σ	1	1	1	1
Polytropic Efficiency e_c	0.9	0.9	0.9	0.9
Approx. Stator Loss Coeff. ϕ_{cs}	0.03	0.03	0.03	0.03
Ratio of Specific Heats γ	1.4	1.4	1.4	1.4
Gas Constant R [kJ/kg-K]	0.2871	0.2871	0.2871	0.2871
C_p [kJ/kg-K]	1.0049	1.0049	1.0049	1.0049
Mean Radius r_m [m]	1.27	0.35	1.27	0.38
Pressure Ratio	2.71	14.36	2.71	22.84
Overall Pressure Ratio OPR	38.9		61.9	

Table 4.2: COMPR outputs for all stages of the LPC

	Stage 1	Stage 2	Stage 3
N_S	61	78	98
c [mm]	133	103.1	82.1
r_{2t} [mm]	1348	1330	1317
r_{2h} [mm]	1190	1208	1221
r_{3t} [mm]	1338	1323	1312
r_{2h} [mm]	1200	1215	1226
$(c/h)_S$ and $(c/h)_R$	0.9	0.9	0.9
T_{2m} [K]	212.1	239.1	266.1
P_{2m} [kPa]	21.12	30.96	43.54
$T_{t,3m,f}$ [K]			299.1
$P_{t,3m,f}$ [kPa]			64.97
$M_{3m,f}$			0.583

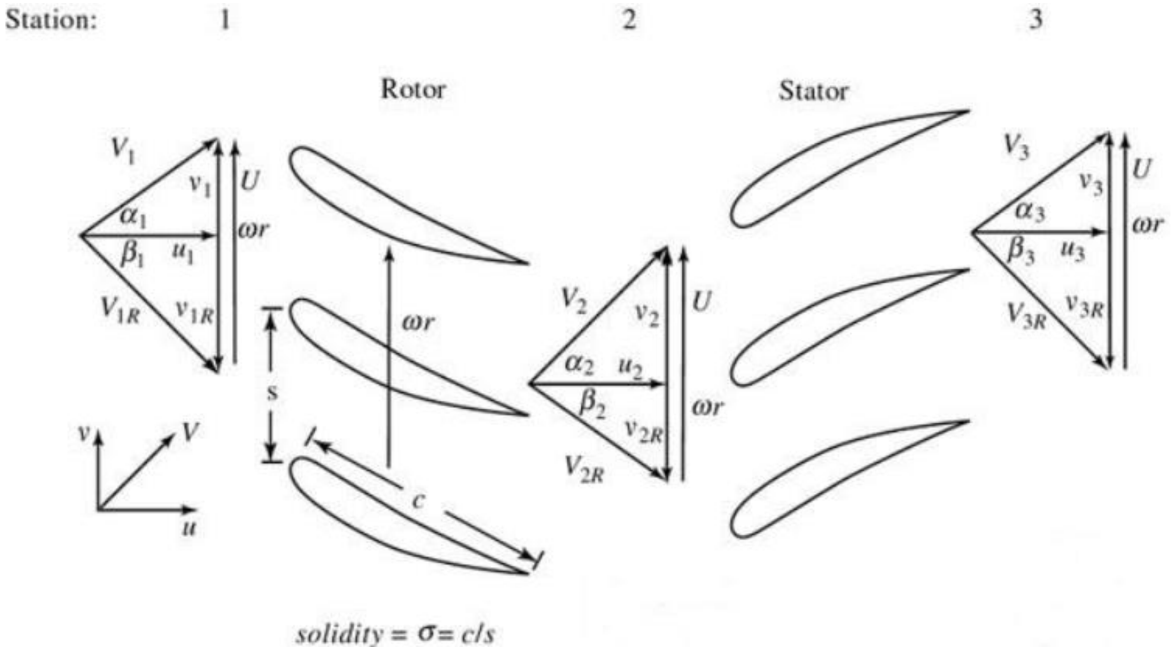

Figure 4.1: Compressor stage nomenclature [4]

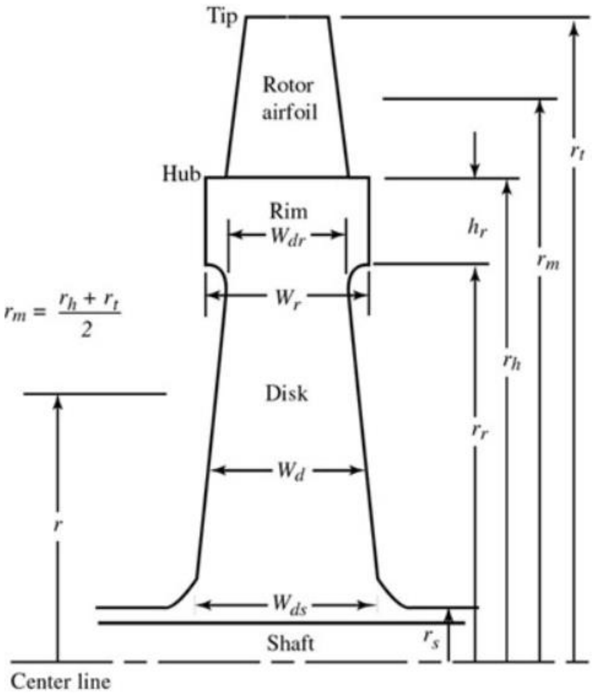

Figure 4.2: Blade-disk nomenclature [4]

The properties of HPC #1 and HPC #2 were evaluated next, and the results are shown in Table 4.3 and Table 4.4, respectively. In order to develop heat transfer models for these compressors, the stator surface area ($A_{o,surf}$), air mass flow rate over one stator ($\dot{m}_h$), and fuel mass flow rate through one stator ($\dot{m}_c$) were calculated using Equations 4.1 – 4.4. The surface area of each blade is estimated as a double-sided trapezoid using the radius and chord values, while the flow rates ($\dot{m}_h$, $\dot{m}_c$) were found simply by dividing the total flow rate ($\dot{m}_{h,tot}$, $\dot{m}_{c,tot}$) by the number of stators (N_S) in each stage. These values, corresponding to the two HPCs, are tabulated in Table 4.5 and Table 4.6. Figure 4.3 and Figure 4.4 show a visual representation of the Compressor Design #1 and Compressor Design #2 generated using COMPR.

$$A_{o,surf} = c[(r_{2t} - r_{2h}) + (r_{3t} - r_{3h})] \tag{4.1}$$

$$A_{o,surf,tot} = N_S A_{o,surf} \tag{4.2}$$

$$\dot{m}_h = \frac{\dot{m}_{h,tot}}{N_S} \tag{4.3}$$

$$\dot{m}_c = \frac{\dot{m}_{c,tot}}{N_S} \tag{4.4}$$

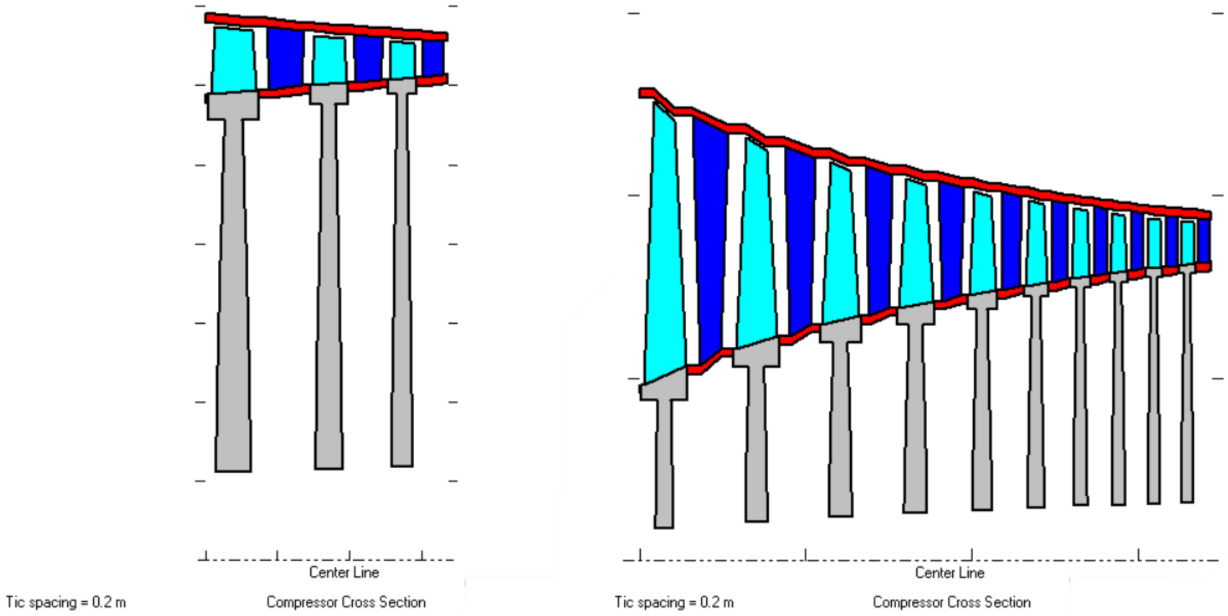

Figure 4.3: Visual representation of Compressor Design #1

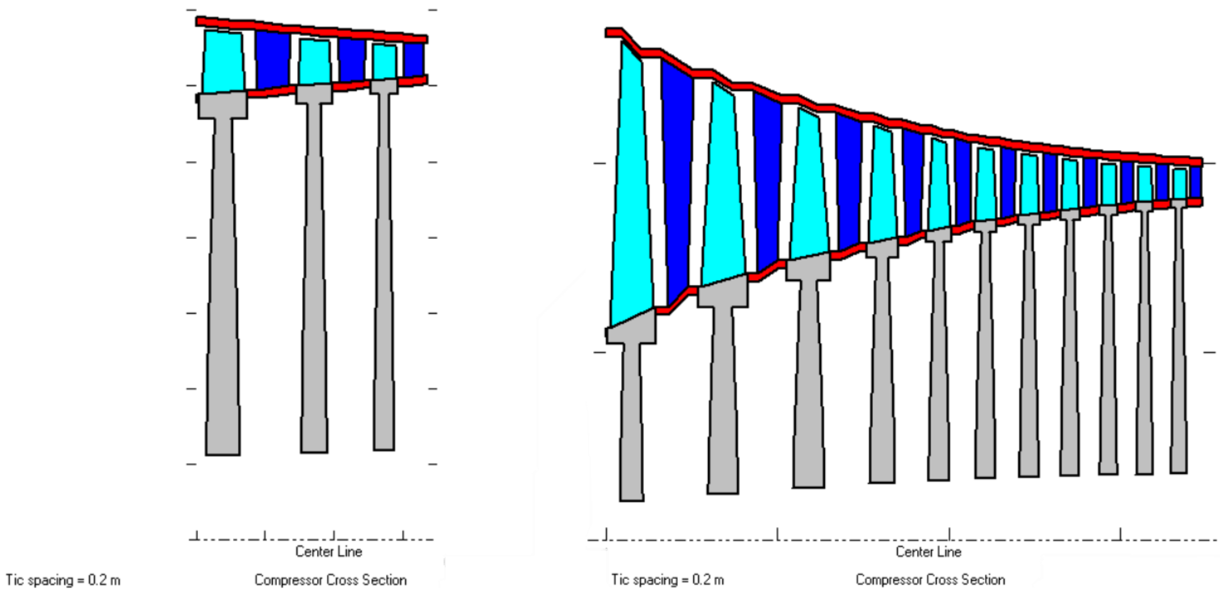

Figure 4.4: Visual representation of Compressor Design #2

Table 4.3: COMPR outputs for all stages of HPC #1

	Stage 1	Stage 2	Stage 3	Stage 4	Stage 5	Stage 6	Stage 7	Stage 8	Stage 9	Stage 10
N_S	44	50	56	60	72	86	101	107	112	116
c [mm]	50.9	45	40.2	37.5	31	26	22	20.8	19.7	19.2
r_{2t} [mm]	487	454	432	416	404	395	388	383	378	375
r_{2h} [mm]	213	246	268	284	296	305	312	317	322	325
r_{3t} [mm]	468	441	423	409	399	391	385	380	376	373
r_{2h} [mm]	232	259	277	291	301	309	315	320	324	327
$(c/h)_S$ and $(c/h)_R$	0.2	0.23	0.26	0.3	0.3	0.3	0.3	0.33	0.36	0.4
T_{2m} [K]	300.0	339.8	379.6	419.4	459.1	498.9	538.7	578.5	618.3	658.1
P_{2m} [kPa]	63.4	94.2	134.0	183.9	245.2	319.1	407.0	510.0	629.6	767.0
$T_{t,3m,f}$ [K]										933
$P_{t,3m,f}$ [kPa]										697
$M_{3m,f}$										0.375

Table 4.4: COMPR outputs for all stages of HPC #2

	Stage 1	Stage 2	Stage 3	Stage 4	Stage 5	Stage 6	Stage 7	Stage 8	Stage 9	Stage 10	Stage 11
N_S	50	54	58	74	91	94	98	103	107	113	118
c [mm]	48.7	45.1	41.6	32.9	26.6	25.6	24.6	23.5	22.4	21.4	48.7
r_{2t} [mm]	512	477	454	438	427	418	412	407	403	400	512
r_{2h} [mm]	248	283	306	322	333	342	348	353	357	360	248
r_{3t} [mm]	491	463	445	432	422	415	409	405	402	399	491
r_{2h} [mm]	269	297	315	328	338	345	351	355	358	361	269
$(c/h)_S$ and $(c/h)_R$	0.2	0.25	0.3	0.3	0.3	0.35	0.4	0.45	0.5	0.55	0.6
T_{2m} [K]	302.8	348.9	395.1	441.2	487.3	533.5	579.6	625.7	671.9	718	764.1
P_{2m} [kPa]	65.2	102.4	152.0	216.0	296.3	394.9	513.8	655.1	820.9	1013.0	1491.0
V_{2m} [m/s]	292	292	292	292	292	292	292	292	292	292	292
$T_{t,3m,f}$ [K]											1484
$P_{t,3m,f}$ [kPa]											806.5
$M_{3m,f}$											0.348

Table 4.5: Stator surface area and fluid flowrate calculations for all stages of HPC #1

	Stage 1	Stage 2	Stage 3	Stage 4	Stage 5	Stage 6	Stage 7	Stage 8	Stage 9	Stage 10
$A_{o,surf}$ [m^2]	0.02596	0.01755	0.01246	0.00938	0.00639	0.00447	0.00321	0.00262	0.00213	0.00184
$A_{o,surf,tot}$ [m^2]	1.142	0.878	0.698	0.563	0.460	0.385	0.324	0.280	0.238	0.214
$\dot{m}_{h,tot}$ [kg/s]	71	71	71	71	71	71	71	71	71	71
$\dot{m}_{c,tot}$ [kg/s]	1.079	1.079	1.079	1.079	1.079	1.079	1.079	1.079	1.079	1.079
$\dot{m}_h$ [kg/s]	1.614	1.420	1.268	1.183	0.986	0.826	0.703	0.664	0.634	0.612
$\dot{m}_c$ [kg/s]	0.0245	0.0216	0.0193	0.0180	0.0150	0.0125	0.0107	0.0101	0.0096	0.0093

Table 4.6: Stator outer surface area and fluid flowrate calculations for all stages of HPC #2

	Stage 1	Stage 2	Stage 3	Stage 4	Stage 5	Stage 6	Stage 7	Stage 8	Stage 9	Stage 10	Stage 11
$A_{o,surf}$ [m^2]	0.02367	0.01624	0.01156	0.00724	0.00473	0.00374	0.00300	0.00244	0.00202	0.00167	0.00139
$A_{o,surf,tot}$ [m^2]	1.183	0.877	0.671	0.536	0.431	0.351	0.294	0.252	0.216	0.189	0.164
$\dot{m}_{h,tot}$ [kg/s]	71	71	71	71	71	71	71	71	71	71	71
$\dot{m}_{c,tot}$ [kg/s]	1.079	1.079	1.079	1.079	1.079	1.079	1.079	1.079	1.079	1.079	1.079
$\dot{m}_h$ [kg/s]	1.420	1.315	1.224	0.959	0.780	0.755	0.724	0.689	0.664	0.628	0.602
$\dot{m}_c$ [kg/s]	0.0216	0.0200	0.0186	0.0146	0.0119	0.0115	0.0110	0.0105	0.0101	0.0095	0.0091

4.2 Stator Heat Exchanger Model Design and Assumptions

As mentioned previously, three effectiveness-NTU heat transfer models were developed to analyze the two HPCs with fuel-integrated stator intercooling. The first model, HX Model #1, served as a baseline and modeled HPC #1 using the experimentally obtained average overall heat transfer coefficient (U) from Chapter 3. This model assumed that U remains constant throughout the compressor. Though this is a substantial assumption due to the great variations in conditions, this model was made simply to provide initial performance values of fuel-integrated intercooling in a typical modern turbofan engine.

The next heat exchanger model, HX Model #2, served closer to an ideal scenario and modeled HPC #2 using chosen values of U that produced roughly a 50% stage heat exchanger effectiveness. This effectiveness value was chosen instead of a higher, more optimal value (such as 80%) because preliminary results showed that the U values required were quite unreasonably large. Therefore, the results from this model were used to get an indication of the overall heat transfer coefficients needed for each stage such that substantial, but not maximal intercooling was achieved.

The final model, HX Model #3, was the most realistic and similarly modeled HPC #2, but instead used values of U approximated using empirical Nusselt number correlations based on the flow properties in each stage. This model aimed to provide some support for whether the U values in HX Model #2 would be achievable in practice. These differences are summarized in Table 4.7.

Table 4.7: Summary of heat exchanger models

	HX Model #1	HX Model #2	HX Model #3
Compressor Modeled	HPC #1	HPC #2	
Description	Average U value from stator heat exchanger experiments used	Values of U chosen for each stage to reach ~50% effectiveness	Values of U approximated using empirical Nu number correlations

All three heat exchanger models employ the effectiveness-NTU method, which allows for the calculation of heat transfer rate based on the fluid inlet temperatures and an effectiveness value. The heat exchanger effectiveness (ϵ) is defined as the ratio of the actual heat transfer rate (q) to the maximum possible heat transfer rate (q_{max}), where q_{max}, in principle, can be achieved in a counterflow heat exchanger of infinite length. These are shown mathematically in Equation 4.5 and Equation 4.6. This method also requires the calculation of the heat capacity rates of the two fluids (C_h and C_c), and determination of which is smaller as shown in Equations 4.7 – 4.10.

$$q_{max} = C_{min}\left(T_{h,i} - T_{c,i}\right) \tag{4.5}$$

$$\epsilon = \frac{q}{q_{max}} \tag{4.6}$$

$$C_h = c_{p,h}\dot{m}_h \tag{4.7}$$

$$C_c = c_{p,c}\dot{m}_c \tag{4.8}$$

$$C_{min} = min[C_h, C_c] \tag{4.9}$$

$$C_{max} = max[C_h, C_c] \tag{4.10}$$

For a given geometry, ϵ can be calculated using correlations in terms of the heat capacity ratio (C_r) and the number of transfer units (NTU) as calculated by Equation 4.11 and 4.12, where U is the overall heat transfer coefficient and $A_{o,surf}$ is the outer surface area of each stator. The heat exchanger modeled, was in a crossflow configuration, as shown in Figure 4.5, but since C_r was found to be nearly zero for all stages in all models, the effectiveness was calculated simply using the correlation shown in Equation 4.13. The actual heat transfer rate from the air to the fuel could then be found by multiplying the difference in the inlet fluid temperatures for that stage, by the effectiveness value and minimum heat capacity rate, as shown in Equation 4.14.

$$C_r = \frac{C_{min}}{C_{max}} \tag{4.11}$$

$$NTU = \frac{UA_{o,surf}}{C_{min}} \tag{4.12}$$

$$\epsilon = 1 - \left(e^{-NTU}\right) \tag{4.13}$$

$$q = \epsilon C_{min}\left(T_{h,i} - T_{c,i}\right) \tag{4.14}$$

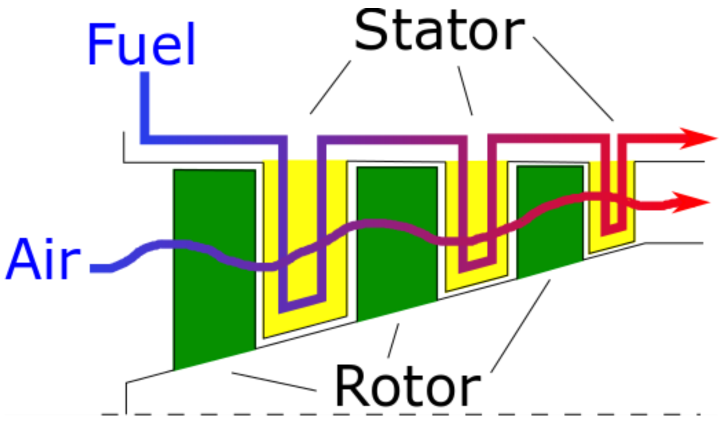

Figure 4.5: Multistage fuel intercooling using stator blades

With the actual heat transfer known, the air and fuel outlet temperatures for that stage could be found using Equation 4.15 and Equation 4.16. However, there is an additional factor (ΔT_{gain}) in Equation 4.16 to account for the temperature rise of the air as it passes over the stator, in addition to the rotor of the following stage. This is shown mathematically in Equation 4.17 and, in the slightly revised form for the temperature gain of the last stage, in Equation 4.18, where n is the stage number. The fluid outlet temperatures were then used to calculate the fluid properties of the proceeding stage, and also as the new inlet temperatures. The other property used to fix the state of both fluids was pressure. The static air pressures before each stator from the COMPR results were used for the air, while the fuel pressure was fixed at 2 MPa for all stages and had an initial temperature of 0°C. Engineering Equation Solver (EES) was used for the evaluation of these fluid properties, with n-dodecane being used as a surrogate for jet fuel. This process was repeated for all but the last stage of both HPCs, where a heat exchanger in the stator was not included ($q = 0$) as it would provide no benefit with regard to the reduction in compressor work. It should also be noted that only temperatures along the mean line of the compressor were used for all calculations.

$$T_{c,o} = T_{c,i} + \frac{q}{C_c} \tag{4.15}$$

$$T_{h,o} = T_{h,i} + \Delta T_{gain} - \frac{q}{C_h} \tag{4.16}$$

$$\Delta T_{gain} = T_{2m,n+1} - T_{2m,n} \tag{4.17}$$

$$\Delta T_{gain} = T_{2m,last} - T_{3m} \tag{4.18}$$

The equations up to this point were sufficient for HX Model #1 and HX Model #2, but HX Model #3 required some additional information about the flow characteristics to evaluate the overall heat transfer coefficient of a stage using Nusselt number correlations. This requires the Reynolds number for the air flowing over the stator and the fuel flowing through the stator.

The stator was modeled as having two channels of equal perimeters and areas as shown in Figure 4.6; one channel brings cool fuel in, while the other carries warmer fuel out to the next stage. The values of the outer cross-sectional area ($A_{o,c/s}$) and outer cross-sectional perimeter ($P_{o,c/s}$) for each stage were found using an airfoil plotter with NACA 6412 blade profiles, and the chord values from the COMPR results. [74] These values were then used in Equations 4.19 – 4.21 to approximate the wetted perimeter (P_w), inner cross-sectional flow area ($A_{i,c/s}$), and hydraulic diameter ($D_{h,c}$). The inner cross-sectional flow area was approximated as 70% of the outer cross-sectional area to account for the walls and halved to account for the two channels. The outer cross-sectional perimeter was similarly halved to estimate the wetted perimeter of one channel. These values are tabulated for HPC #2 in Table 4.8.

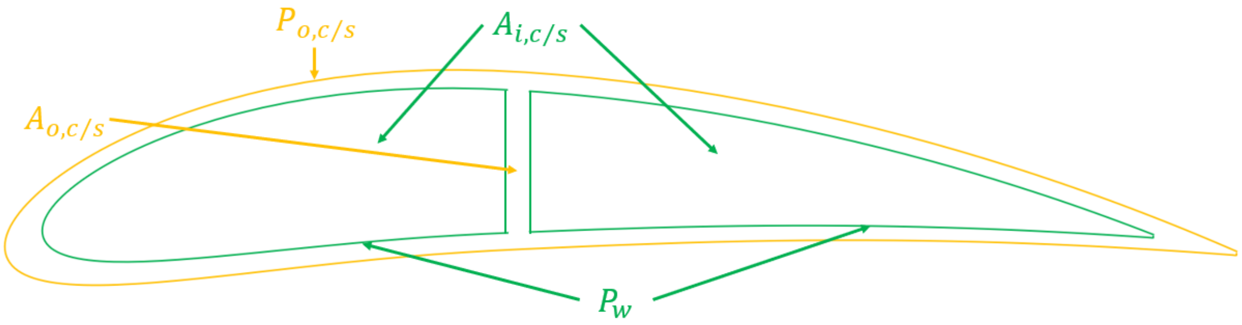

Figure 4.6: Cross section of stator blade

$$P_w = \frac{P_{o,c/s}}{2} \tag{4.19}$$

$$A_{i,c/s} = \frac{0.7A_{o,c/s}}{2} \tag{4.20}$$

$$D_{h,c} = \frac{4A_{i,c/s}}{P_w} \tag{4.21}$$

Table 4.8: Calculated values for stator cross section for all stages of HPC #2

	Stage 1	Stage 2	Stage 3	Stage 4	Stage 5	Stage 6	Stage 7	Stage 8	Stage 9	Stage 10	Stage 11
$P_{o,c/s}$ [mm]	100.3	92.9	85.7	67.7	54.8	52.7	50.7	48.4	46.1	44.1	42.0
P_w [mm]	50.2	46.4	42.8	33.9	27.4	26.4	25.3	24.2	23.1	22.0	21.0
$A_{o,c/s}$ [mm^2]	196.1	168.2	143.1	89.51	58.51	54.2	50.05	45.67	41.49	37.87	34.42
$A_{i,c/s}$ [mm^2]	68.6	58.9	50.1	31.3	20.5	19.0	17.5	16.0	14.5	13.3	12.0
$D_{h,c}$ [mm]	5.47	5.07	4.68	3.70	2.99	2.88	2.77	2.64	2.52	2.41	2.29

The velocity of the fuel (V_c) through the stator channel was calculated using Equation 4.22, and the Reynolds number ($Re_{D_h,c}$) subsequently using Equation 4.23, with the hydraulic diameter as the characteristic length. The Reynolds number of the air ($Re_{chord,h}$) over the stator was calculated using Equation 4.24 with the chord (c) as the characteristic length and the velocity before the stator (V_{2m}) from the COMPR results. Similar to the specific heats, the density of the fuel (ρ_c) and the kinematic viscosity of both fluids (ν_c and ν_h) were evaluated for each stage at the previous stage's outlet conditions using EES.

$$V_c = \frac{\dot{m}_c}{\rho_c A_{i,c/s}} \tag{4.22}$$

$$Re_{D_h,c} = \frac{V_c D_{h,c}}{\nu_c} \tag{4.23}$$

$$Re_{chord,h} = \frac{V_{2m} c}{\nu_h} \tag{4.24}$$

With the Reynolds numbers of a stage taken into consideration, appropriate Nusselt number correlations were chosen for the two fluids. The fuel Reynolds number was found to be less than the critical Reynolds number ($Re_{D,cr}$) for internal flows as shown in Equation 4.25 for all stages, and consequently a laminar correlation of the fuel Nusselt number (Nu_c) was used for all stages. Since the channels were irregularly shaped, a rectangular duct with an aspect ratio of 4:1 was selected to approximate the two channels. A uniform surface heat flux condition or a uniform surface temperature condition did not suit the surface thermal condition that might be present along the stator, so an average of the two correlations (Equation 4.26 and Equation 4.27) was found and shown in Equation 4.28. Another assumption made for these correlations to be applied, was that the flow in the channels were fully developed.

$$Re_{D,cr} = 2300 \tag{4.25}$$

$$Nu_c = 5.33 \tag{4.26}$$

$$Nu_c = 4.44 \tag{4.27}$$

$$\overline{Nu_c} = 4.89 \tag{4.28}$$

Although there are some published values of the critical Reynolds number over certain airfoil shapes, none were found for the NACA 6412 blade being assessed. Therefore, the air flow over the stator was equated to external flow over a flat plate and a corresponding critical Reynolds number ($Re_{x,cr}$) was used, as shown in Equation 4.29. The air Reynolds number was found to be above, yet close, to this critical Reynolds number, particularly in the early stages. Due to this, a mixed boundary layer correlation for the average air Nusselt number ($\overline{Nu}_h$) was chosen, as shown in Equation 4.30.

$$Re_{x,cr} = 5 \times 10^5 \tag{4.29}$$

$$\overline{Nu}_h = \left(0.037Re_{chord,h}^{4/5} - \left(0.037Re_{x,cr}^{4/5} - 0.664Re_{x,cr}^{1/2}\right)\right) Pr_h^{1/3} \tag{4.30}$$

The average air heat transfer coefficient ($\bar{h}_h$) and average fuel heat transfer coefficient ($\bar{h}_c$) were then calculated by the definition of the Nusselt number using Equation 4.31 and Equation 4.32, respectively. These values were used, along with the wall thickness of the stator (t_{wall}) and the stator material conductivity (k_{wall}), to calculate an approximate average overall heat transfer coefficient (U) using Equation 4.33. The wall thickness was set at 2 mm and the conductivity of 20 W/m-K was chosen as an approximate value for titanium alloy or nickel alloy blades. The U value was then used in the same process previously described to determine the number of transfer units and the heat exchanger effectiveness. It should be noted that Equation 4.33 assumes that the outer and inner surface areas of the stator approach being equal, which is a fair assumption with the described stator-channel layout. Lastly, it should be stressed that this process was conducted on a stage-by-stage basis with the Reynolds number being considered for every new stage to ensure the correlations were still applicable.

$$\bar{h}_h = \frac{\overline{Nu}_h k_h}{c} \tag{4.31}$$

$$\bar{h}_c = \frac{\overline{Nu}_c k_c}{D_{h,c}} \tag{4.32}$$

$$U = \left(\frac{1}{\bar{h}_h} + \frac{t_{wall}}{k_{wall}} + \frac{1}{\bar{h}_c}\right)^{-1} \tag{4.33}$$

4.3 Stator Heat Exchanger Model Results and Discussion

The heat capacity rates (C_h and C_c), overall heat transfer coefficients (U), number of transfer units (NTU), heat capacity ratios (C_r), effectiveness (ϵ), heat transfer rates per blade (q), air temperatures (T_h), and fuel temperatures (T_c) are tabulated for HX Model #1, HX Model #2, and HX Model #3 in Table 4.9, Table 4.10, and Table 4.11, respectively. For comparison, these also show the temperatures of the fluids in each stage if no heat exchange was present and the difference between those and the model temperatures (ΔT_h and ΔT_c).

HX Model #1 used the average experimentally obtained U value of 105 W/m^2-K from the stator heat exchanger experiments for each stage of HPC #1. As expected, this resulted in extremely low values of NTU and ϵ, and thus only around 100 W of heat was transferred from the air to the fuel per blade as seen in Table 4.9. This resulted in a compressor exit temperature 0.9°C less than having no heat exchanger and a fuel exit temperature 28.2°C greater than having no heat exchanger. Another interesting observation made was how small the value of the heat capacity ratio was. This suggests that even if very high effectiveness values were achieved, there simply would not be enough fuel flow to significantly lower the air temperature to meaningfully reduce the compressor work.

HX Model #2 analyzed HPC #2 and provided more of an idealistic model by using values of U chosen to reach approximately 50% heat transfer effectiveness for each stage. This resulted in about a 1-2°C reduction in air temperature per stage and a final compressor exit temperature 15.7°C lower than the baseline without heat exchangers as shown in Table 4.10. Thus, a fuel-integrated heat exchanger even with a reasonably high effectiveness, would likely result in inconsequential intercooling at cruise conditions. On the other hand, the fuel outlet temperature increased significantly by 386.3°C from its initial temperature of 0°C. This also goes to show that intercooling alone would not result in thermal or catalytic cracking of the fuel in a compressor with an overall pressure ratio of roughly 60:1. This could change either from using a higher pressure ratio engine or incorporating some amount of exhaust recuperation. The last things of note from this model, were the high values of U, with the final stage requiring 14,000 W/m^2-K to achieve 50% effectiveness. This is not unattainable, but is quite large, and even near the high end of typical liquid-to-liquid forced convection heat exchanger systems. [72]

Table 4.9: Single blade HX Model #1 using experimentally obtained U for first 9 stages of HPC #1

	Initial	Stage 1	Stage 2	Stage 3	Stage 4	Stage 5	Stage 6	Stage 7	Stage 8	Stage 9	Final
$c_{p,h}$ [kJ/kg-K]		1.006	1.008	1.012	1.017	1.023	1.031	1.039	1.048	1.057	
$c_{p,c}$ [kJ/kg-K]		2.137	2.139	2.148	2.156	2.165	2.177	2.189	2.198	2.211	
C_h [W/K]		1623.3	1431.4	1283.1	1203.5	1008.8	851.2	730.4	695.4	670.1	
C_c [W/K]		52.4	46.2	41.4	38.8	32.4	27.3	23.4	22.2	21.3	
U [W/m^2-K]		105	105	105	105	105	105	105	105	105	
NTU		0.052	0.040	0.032	0.025	0.021	0.017	0.014	0.012	0.010	
C_r		0.032	0.032	0.032	0.032	0.032	0.032	0.032	0.032	0.032	
ϵ		0.051	0.039	0.031	0.025	0.020	0.017	0.014	0.012	0.010	
q [W]		71.7	118.1	132.1	135.2	116.2	98.3	82.8	77.5	71.0	
T_h [K]	300	339.8	379.5	419.2	458.8	498.4	538.1	577.8	617.5	657.2	677.0
T_c [K]	273	274.4	276.9	280.1	283.6	287.2	290.8	294.3	297.8	301.2	301.2
TEMPERATURES WITHOUT HEAT EXCHANGERS FOR COMPARISON											
T_h [K]	300.0	339.8	379.6	419.4	459.1	498.9	538.7	578.5	618.3	658.1	677.9
T_c [K]	273	273	273	273	273	273	273	273	273	273	273
ΔT_h [K]	0.0	0.0	-0.1	-0.2	-0.3	-0.5	-0.6	-0.7	-0.8	-0.9	-0.9
ΔT_c [K]	0.0	1.4	3.9	7.1	10.6	14.2	17.8	21.3	24.8	28.2	28.2

Table 4.10: Single blade HX Model #2 of the first 10 stages of HPC #2 using chosen U values for ~50% stage effectiveness

	Initial	Stage 1	Stage 2	Stage 3	Stage 4	Stage 5	Stage 6	Stage 7	Stage 8	Stage 9	Stage 10	Final
$c_{p,h}$ [kJ/kg-K]		1.006	1.009	1.014	1.02	1.028	1.037	1.046	1.057	1.068	1.078	
$c_{p,c}$ [kJ/kg-K]		2.137	2.178	2.276	2.414	2.575	2.747	2.920	3.102	3.299	3.551	
C_h [W/K]		1428.5	1326.6	1241.3	978.6	802.1	783.3	757.8	728.6	708.7	677.3	
C_c [W/K]		46.1	43.5	42.3	35.2	30.5	31.5	32.1	32.5	33.3	33.9	
U [W/m^2-K]		1300	1800	2500	3300	4400	5600	7300	9000	11000	14000	
NTU		0.667	0.672	0.683	0.679	0.682	0.664	0.681	0.677	0.667	0.689	
C_r		0.032	0.033	0.034	0.036	0.038	0.040	0.042	0.045	0.047	0.050	
ϵ		0.487	0.489	0.495	0.493	0.495	0.485	0.494	0.492	0.487	0.498	
q [W]		669.1	1296.7	1599.6	1446.0	1312.6	1353.7	1428.8	1433.8	1453.9	1522.6	
T_h [K]	302.8	348.4	393.7	438.5	483.1	527.7	572.0	616.2	660.5	704.5	748.4	771.8
T_c [K]	273	287.5	317.3	355.1	396.2	439.2	482.1	526.5	570.6	614.3	659.3	659.3
TEMPERATURES WITHOUT HEAT EXCHANGERS FOR COMPARISON												
T_h [K]	302.8	348.9	395.1	441.2	487.3	533.5	579.6	625.7	671.9	718	764.1	787.5
T_c [K]	273	273	273	273	273	273	273	273	273	273	273	273
ΔT_h [K]	0.0	-0.5	-1.4	-2.7	-4.2	-5.8	-7.6	-9.5	-11.4	-13.5	-15.7	-15.7
ΔT_c [K]	0.0	14.5	44.3	82.1	123.2	166.2	209.1	253.5	297.6	341.3	386.3	386.3

HX Model #3 was made to determine how realistic/achievable the values found in HX Model #2 might be by using the flow conditions in the heat exchanger and Nusselt number correlations described in Section 4.2. The results, shown in Table 4.11, suggest that the U values in HX Model #2 would be difficult to achieve in practice as there is a magnitude of difference between the values in the two models. The compressor exit temperature in this model ended up decreasing by 1.8°C, while the outlet fuel temperature increased by 54.7°C compared to the baseline values without heat exchangers. Like HX Model #1, this model had very low levels of effectiveness ranging from 4.4% to 1.8% per stage.

The Reynolds number ($Re_{chord,h}$ and $Re_{D_h,c}$), Nusselt number ($\overline{Nu}_h$ and $\overline{Nu}_c$), and average heat transfer coefficient ($\bar{h}_h$ and $\bar{h}_c$) in each stage for both fluids are shown in Table 4.12. As previously mentioned, the air flow likely had mixed boundary flow conditions with Reynolds numbers ranging from 5.51×10^5 to 8.81×10^5. The fuel flow conditions were found to be laminar in all stages, with the Reynolds number approaching the critical Reynolds number by the 10th stage with a value of 1,810. Thus, the Nusselt number correlations are justified. It should also be noted that the fuel heat transfer coefficient is the main contributor to the low values of U, particularly in the latter stages, where the air heat transfer coefficient reaches the thousands, and the fuel heat transfer coefficient remains in the low hundreds. This could potentially be improved if mixed or turbulent conditions were achieved that are more conducive to higher heat transfer coefficients. Regardless, the overall heat transfer coefficients would still likely be an order of magnitude lower than those chosen in HX Model #2, even if the fuel heat transfer coefficients became roughly equal to the air heat transfer coefficients.

The differences between these three heat exchanger models, with regard to exit fuel and air temperatures, are summarized in Table 4.13. Ultimately, these results indicate that the FIERA engine would likely not be viable without a significant increase in heat transfer area. This would again cut back at the main attributes of the idea, namely the small weight penalty, unchanged air pressure drop, and relative simplicity of using multipurposed components.

Table 4.11: Single blade HX Model #3 of the first 10 stages of HPC #2 using calculated U values from Nu correlations

	Initial	Stage 1	Stage 2	Stage 3	Stage 4	Stage 5	Stage 6	Stage 7	Stage 8	Stage 9	Stage 10	Final
$c_{p,h}$ [kJ/kg-K]		1.006	1.009	1.014	1.02	1.028	1.037	1.048	1.059	1.07	1.081	
$c_{p,c}$ [kJ/kg-K]		2.137	2.14	2.148	2.162	2.177	2.197	2.219	2.242	2.266	2.29	
C_h [W/K]		1428.5	1326.6	1241.3	978.6	802.1	783.3	759.3	730.0	710.0	679.2	
C_c [W/K]		46.1	42.8	40.0	31.5	25.8	25.2	24.4	23.5	22.9	21.9	
U [W/m^2-K]		88	104	118	147	179	192	203	214	225	236	
NTU		0.045	0.040	0.034	0.034	0.033	0.028	0.025	0.022	0.020	0.018	
C_r		0.032	0.032	0.032	0.032	0.032	0.032	0.032	0.032	0.032	0.032	
ϵ		0.044	0.039	0.034	0.033	0.032	0.028	0.025	0.022	0.020	0.018	
q [W]		61.0	123.5	158.4	167.5	167.1	169.5	167.9	164.7	160.7	154.5	
T_h [K]	302.8	348.9	395.0	440.9	486.9	532.9	578.7	624.6	670.6	716.5	762.3	785.7
T_c [K]	273	274.3	277.2	281.2	286.5	293.0	299.7	306.6	313.6	320.6	327.7	327.7
TEMPERATURES WITHOUT HEAT EXCHANGERS FOR COMPARISON												
T_h [K]	302.8	348.9	395.1	441.2	487.3	533.5	579.6	625.7	671.9	718	764.1	787.5
T_c [K]	273	273	273	273	273	273	273	273	273	273	273	273
ΔT_h [K]	0.0	0.0	-0.1	-0.3	-0.4	-0.6	-0.9	-1.1	-1.3	-1.5	-1.8	-1.8
ΔT_c [K]	0.0	1.3	4.2	8.2	13.5	20.0	26.7	33.6	40.6	47.6	54.7	54.7

Table 4.12: Calculations of U using Nu correlations for use in HX Model #3

	Stage 1	Stage 2	Stage 3	Stage 4	Stage 5	Stage 6	Stage 7	Stage 8	Stage 9	Stage 10
t_{wall} [m]	0.002	0.002	0.002	0.002	0.002	0.002	0.002	0.002	0.002	0.002
k_{wall} [W/m-K]	20	20	20	20	20	20	20	20	20	20
V_c [m/s]	0.411	0.444	0.487	0.613	0.767	0.806	0.843	0.885	0.945	0.987
$Re_{chord,h}$	5.71E+5	6.46E+5	7.12E+5	6.61E+5	6.18E+5	6.79E+5	7.37E+5	7.89E+5	8.36E+5	8.81E+5
$Re_{D_h,c}$	7.40E+2	7.63E+2	8.23E+2	9.07E+2	1.01E+3	1.16E+3	1.30E+3	1.46E+3	1.64E+3	1.81E+3
$\overline{Nu}_h$	551.6	689.0	806.1	714.8	636.5	747.4	852.4	943.6	1026.4	1106.8
$\overline{Nu}_c$	4.89	4.89	4.89	4.89	4.89	4.89	4.89	4.89	4.89	4.89
$\bar{h}_h$ [W/m^2-K]	301	457	642	787	937	1227	1553	1909	2301	2731
$\bar{h}_c$ [W/m^2-K]	127	137	147	185	226	232	239	247	256	265
U [W/m^2-K]	88	104	118	147	179	192	203	214	225	236

Table 4.13: Output fuel and air temperatures for each HX model compared to having no HX

	HX Model #1		HX Model #2		HX Model #3	
	$T_{c,o}$	$T_{h,o}$	$T_{c,o}$	$T_{h,o}$	$T_{c,o}$	$T_{h,o}$
T_{model} [K]	301.2	677.0	659.3	771.8	327.7	785.7
$T_{original}$ [K]	273.0	677.9	273.0	787.5	273.0	787.5
ΔT [K]	+28.2	-0.9	+386.3	-15.7	+54.7	-1.8

Chapter 5

Thermally Enhanced Kerosene Combustion Experiments

5.1 Experimental Approach for Combustion Experiments

These experiments were designed to determine the effect, if any, a thermally enhanced kerosene fuel had on emissions, the lean blowout limit, and combustion characteristics. The same approach (i.e., factorial design of experiments), was used as described in Section 3.1.

The output parameters were determined at different experimental conditions, again using a two-level factorial design of experiments with independent variables having a high (+) and low (-) level corresponding to a chosen value. Two independent variables were chosen for these experiments and therefore there are 2^2 unique configurations as shown in Table 5.1. This method enabled the formulation of an empirical model of the form shown in Equation 5.1, relating the effects (E_1, E_2) and interaction (I_{12}) of the chosen variables (X_1, X_2) and the average output of all runs ($\bar{Y}$) to the predicted output (Y). The effects were calculated using Equation 5.2 and the interaction between the two variables was calculated similarly using Equation 5.3. Only one set of replications were conducted for these experiments, but the statistical significance was again found using Equations 3.15 – 3.20 from Section 3.1.

Table 5.1: Configuration list for 2^2 factorial design of experiments

Config.	X_1	X_2
1	$+$	$+$
2	$+$	$-$
3	$-$	$+$
4	$-$	$-$

$$Y = \bar{Y} + \frac{E_1}{2}X_1 + \frac{E_2}{2}X_2 + + \frac{I_{12}}{2}X_1X_2 \tag{5.1}$$

$$E_i = \frac{1}{2}\left(\sum_{run=1}^{4} Y_{run}X_{i,run}\right) \tag{5.2}$$

$$I_{ij} = \frac{1}{2}\left(\sum_{run=1}^{4} Y_{run}X_{i,run}X_{j,run}\right) \tag{5.3}$$

5.2 Input Variables and Output Parameters for Combustion Experiments

Two independent variables were chosen for these experiments: fuel temperature (X_1) and air mass flow rate (X_2). A “high” and “low” level were selected for each of these variables and their coded experimental values are shown in Table 5.2. The “high” levels for both variables were set at the limits of the system with the maximum achievable fuel temperature being 80°C and maximum air mass flow rate being 1000 SLPM. The “low” level for the fuel temperature was 25°C and the chosen “low” level for the air mass flow rate was 600 SLPM. The fuel flow rate was kept constant at 0.48 g/s, creating two globally fuel-lean configurations as shown in Table 5.3. This value was the lowest achievable flowrate the pump could provide to produce a stable spray without sputtering. The output parameters from these experiments were the concentration of nitrogen oxides, CO, CO_2, and unburned hydrocarbons, as well as the exhaust temperature.

Table 5.2: Input variables’ experimental values corresponding to “high” and “low” levels

Independent Variables	−	+
Fuel Temperature (X_1) [°C]	25	80
Air Mass Flow Rate (X_2) [SLPM]	600	1000

Table 5.3: Experimental configuration air-fuel ratio, fuel-air ratio, and fuel-air equivalence ratio

	AFR	FAR	ϕ
$X_2 = " - "$	25	0.040	0.62
$X_2 = " + "$	41	0.024	0.37

5.3 Facility and Data Acquisition for Combustion Experiments

Figure 5.1 shows the overall P&ID for the experiments. Air was supplied to the laboratory from an air-compressor and mass flow rate was measured and controlled using two mass flow controllers (each with a maximum of 500 SLPM). The air was then heated successively by two 750 W gas heaters after which, it entered the bottom of the combustion chamber. The co-flow air then passed through an airflow straightener before reaching the nozzle. The kerosene was pumped from a covered reservoir through a series of three 750 W cartridge heaters before reaching the nozzle. A sampling probe at the top of the combustion chamber collected a portion of the exhaust products for analyzing before the remainder was exhausted to the fume hood. The full system is shown in Figure 5.2.

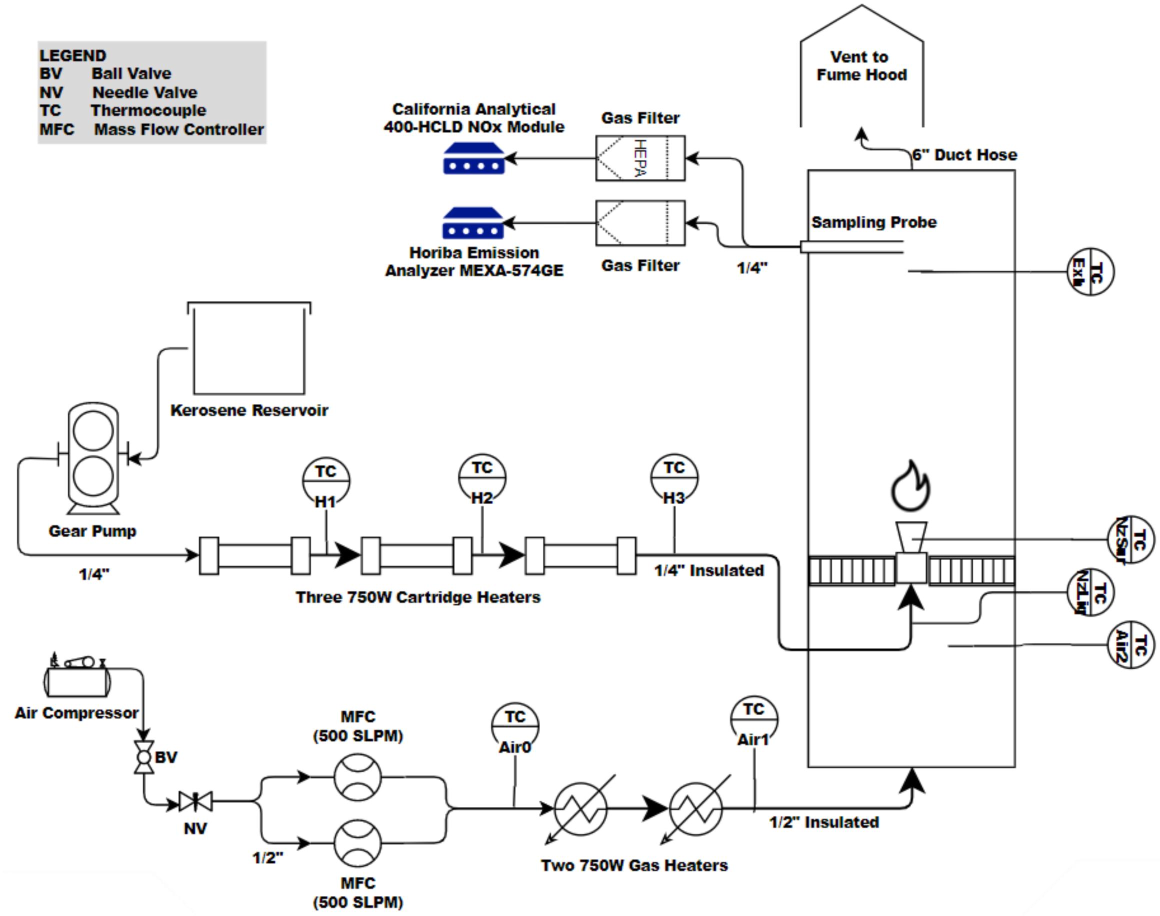

Figure 5.1: P&ID for the combustion experiments

Figure 5.2: Combustion chamber and experimental facility

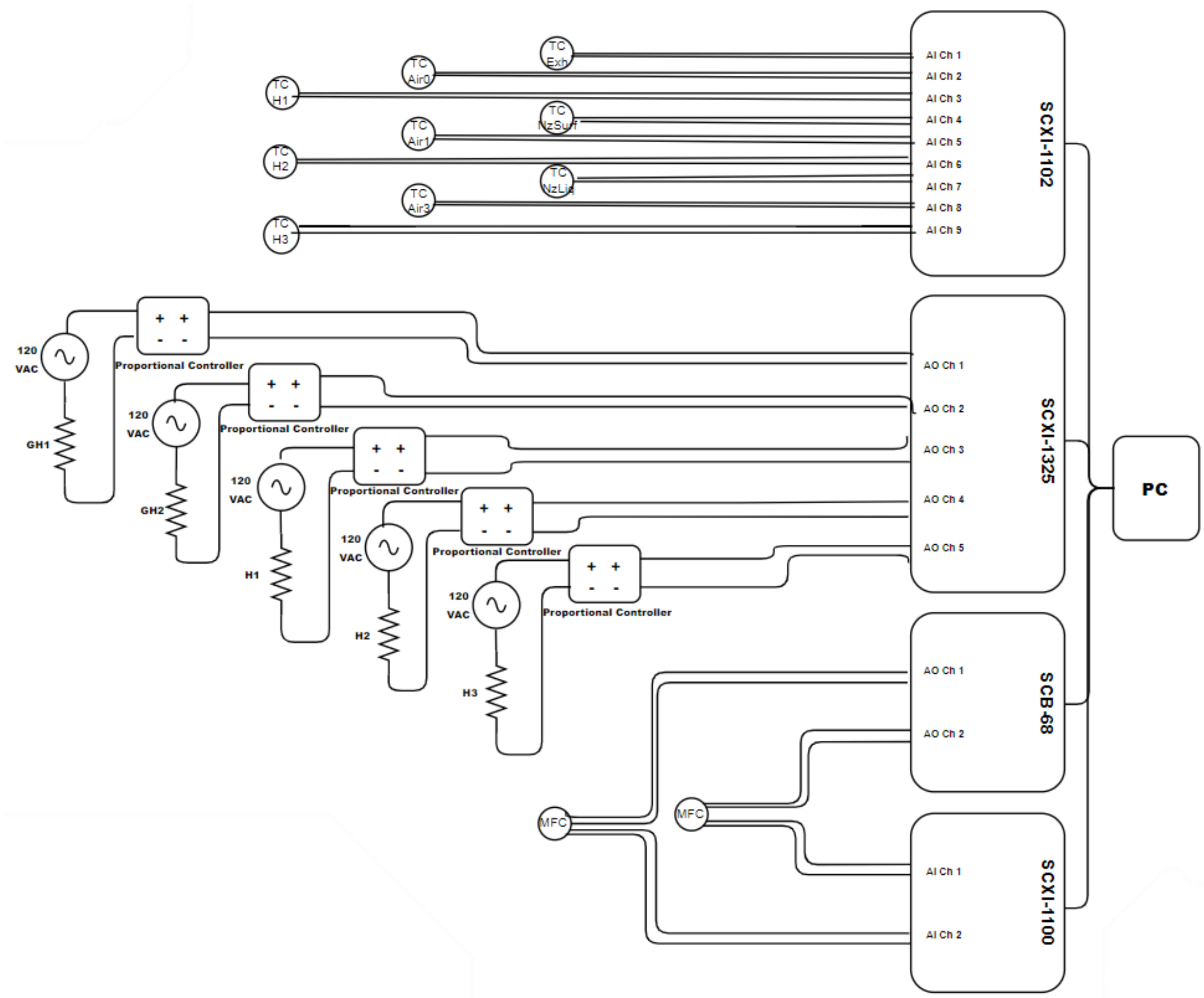

Figure 5.3: Wiring diagram for the combustion experiments

Measurement and control systems were connected to a data acquisition PC via National Instruments (NI) hardware (SCXI-1000 chassis with four modules) as shown in Figure 5.3 and was operated using NI LabVIEW software, which was set to record data at 2 Hz. All temperature measurements were taken with 1/16” or 1/32” sheathed K-type thermocouples and connected to the NI SCXI 1102 module.

Two Aalborg GFC67 mass flow controllers (MFCs) were used to monitor air flow. The feedback voltages from both instruments to the NI SCXI 1100 module were converted to SLPM in LabVIEW virtual instrument (VI), and the desired total SLPM of airflow was maintained for the different experimental conditions using output control voltages from the NI SCB68 module.

The series of fuel heaters consisted of three 750 W cartridge heaters fitted inside 316 SS pipe filled with aluminum pellets to enhance heat transfer as shown in Figure 5.4. Two 750 W Omega T-type in-line gas heaters were used to heat the co-flow air to a temperature of 105°C before passing the nozzle. All heaters and subsequent piping were covered in fiberglass insulation to minimize heat loss. Each heater was controlled manually from 0 to 100% by a proportional controller (Crydom MCPC-1225) using a 0-5 VDC control voltage from the NI SCXI 1325 module so that the desired air temperature and fuel temperature at the nozzle were maintained.

Room temperature kerosene was pumped from a closed container to the combustion chamber using a Cole-Parmer model 75211-30 gear pump and a model L22097 pump head. Mass flow rate calibration of the kerosene was conducted before experiments using a digital scale and timer.

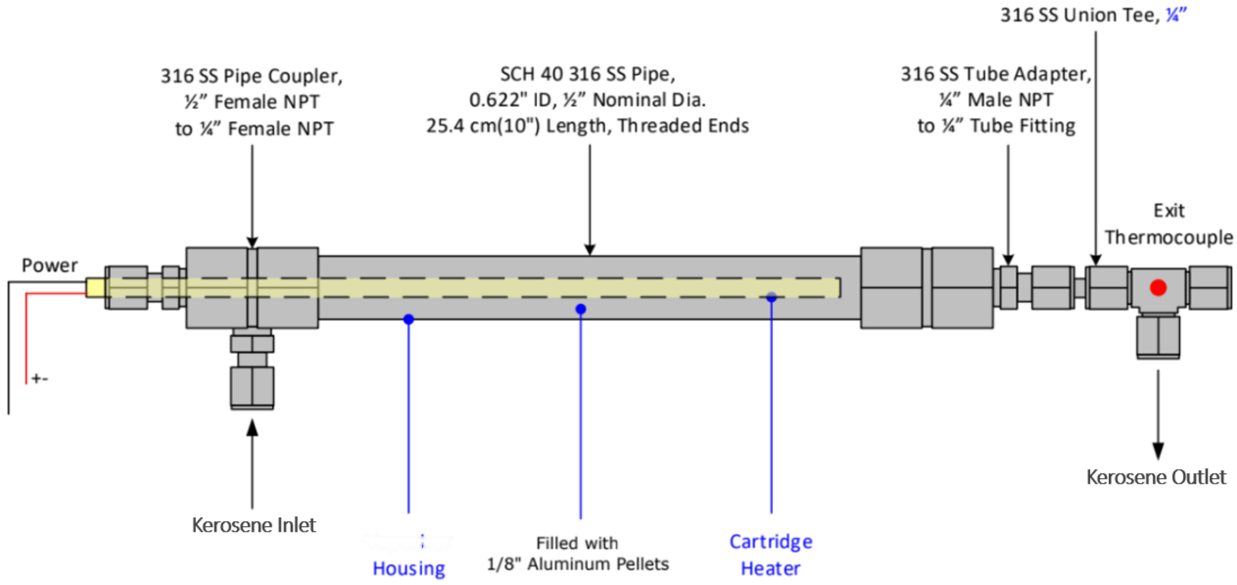

Figure 5.4: Schematic of cartridge heater adapted from [76]

Figure 5.5 shows the detailed schematic of the combustion chamber. The sampling probe was located in the center of the chamber approximately 54" downstream from the nozzle. The exhaust temperature was also measured at this location using a thermocouple. The nozzle used was a full cone misting nozzle with a 0.01" orifice diameter and 80° spray angle. The thermocouple placed in the fuel line before the nozzle was used for the fuel temperature measurements, while a thermocouple touching the outside of the nozzle was used to monitor the surface temperature. An additional thermocouple measured the temperature of the heated co-flow air before it passed through the 2” thick, 1/8” honeycomb flow straightener. A 1” diameter cutout in the side of the combustion chamber enabled access to the nozzle for ignition and was covered during the tests. A pyroceramic glass panel on one side of the combustion chamber enabled visual access to the flame. The sampling probe at the top of the combustion chamber was connected to a California Analytical 400-HCLD NOx module and a Horiba MEXA-574GE emissions analyzer for measurements of CO_2, CO, and UHCs.

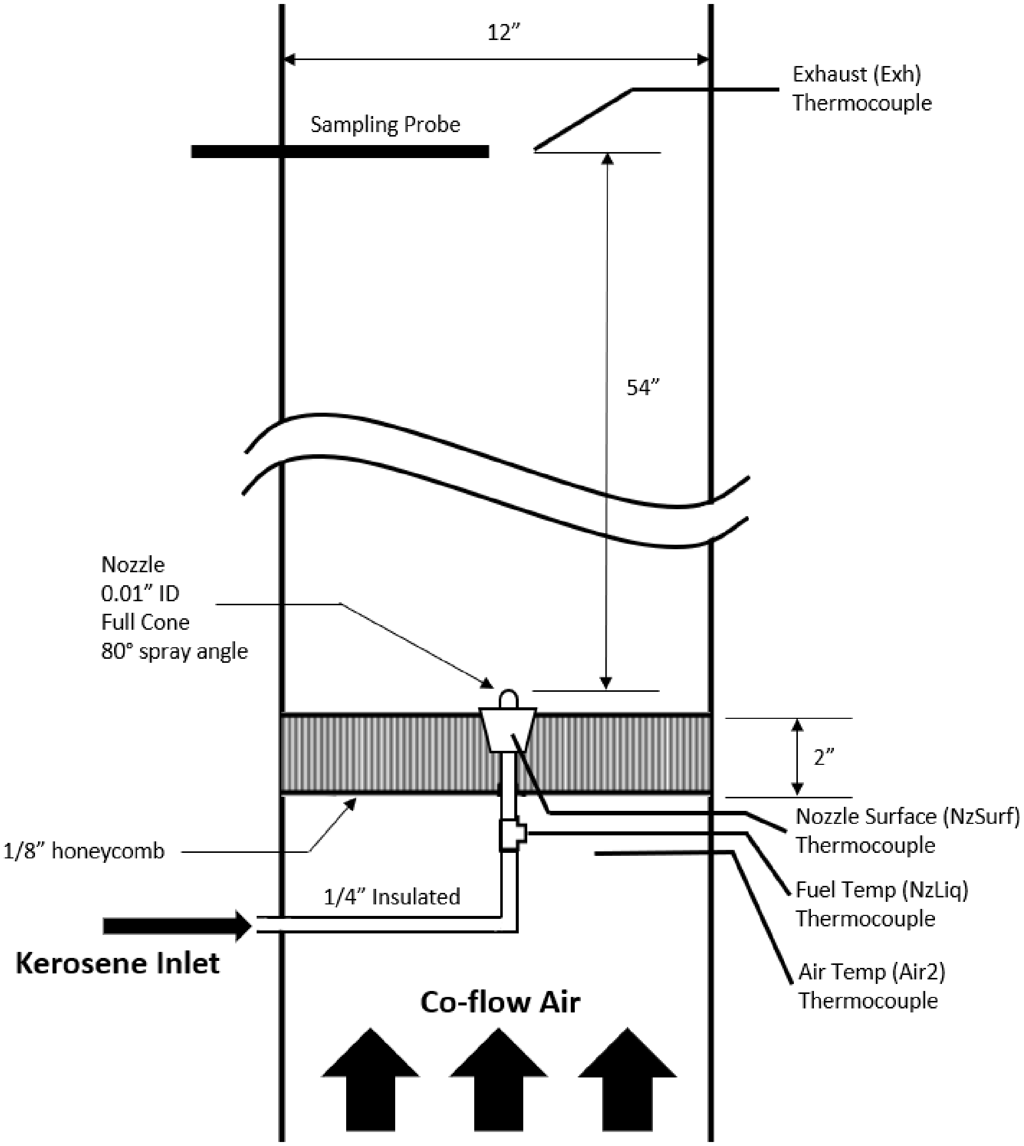

Figure 5.5: Schematic of combustion chamber

5.4 Experimental Procedure for Combustion Experiments

First, the controls and data acquisition subsystems were turned on, along with the emissions analyzers and MFCs. The Horiba emissions analyzer was calibrated after a 10-minute warmup time per the manufacturer’s operating manual. The California Analytical gas analyzer was allowed to warmup for one hour as recommended in the operating manual before calibration was conducted. The compressed air line was opened, and one MFC was set to 500 SLPM, while the other was set at 100 SLPM. The control voltage to both gas heaters was increased until the air temperature before the nozzle was at roughly 105°C. The system was then allowed to warmup for 15 minutes.

A 1000 mL Erlenmeyer flask was filled with kerosene before a rubber stopper with a fitted tube connected to the pump was put into place. The pump was turned on and once the fuel reached the nozzle, a propane torch was used to ignite the flame through the 1” diameter hole in the side of the combustion chamber. This opening was closed after ignition.

The air mass flow rate was adjusted according to the experimental configuration being tested and the control voltages to the fuel heaters were increased to attain the elevated fuel temperature before the nozzle when necessary. When the temperatures seemed to stabilize after about four or five minutes, the exhaust was sampled alternatingly by the Horiba and California Analytical for one to two minutes each, and values were manually recorded. The thermocouple temperature values were automatically written to an excel file every 0.5 seconds for post processing.

The pump was turned off after the trials were done or if a “low” level fuel temperature configuration was to be conducted after a “high” level configuration, as it took a substantial amount of time for the entire fuel line to cool back down.

As discussed previously, four configurations were tested with one set of replications using a factorial design of experiments. The run order for the configurations were randomized to reduce the potential effect of process drift on the results and this order is shown in Table 5.4.

Table 5.4: Experimental run order for combustion experiments

	Coded Levels		Experimental Values		Run Order
Config.	Fuel Temp (X_1)	Air Flow (X_2)	Fuel Temp (°C)	Air Flow (SLPM)	Runs
1	+	+	80	1000	2, 7
2	+	−	80	600	6, 8
3	−	+	25	1000	4, 5
4	−	−	25	600	1, 3

5.5 Combustion Results and Discussion

Unfortunately, there were a few significant issues that were encountered with these experiments that need to be discussed. The most impactful to the emissions results was the large amount of particulate matter generated by the flame, that ultimately led to unusable results. This was attempted to be resolved in a few ways. The first was to decrease the fuel flow in an attempt to reduce the fuel-rich pockets that were expected to be contributing to this and burn more fuel-lean, which succeeded to an extent. However, the pump could not produce high enough pressure to sufficiently atomize the fuel and avoid sputtering at the lower flow rates. Therefore, the air mass flow rate was increased.

Instead of the original configuration using only one MFC, the second MFC was added to provide additional air, allowing for an even higher air-to-fuel ratio at maximum flow conditions. This also increased the maximum co-flow air Reynolds number ($Re_{D_h,h}$) from 1580 to 3150, which is above the critical Reynolds number for internal flows (2300). (This value was calculated using the hydraulic diameter of the combustion chamber as the characteristic length and air properties evaluated at 1 bar and 105°C.) The resulting turbulent conditions were expected to enhance the local mixing of the fuel and air. Unfortunately, these changes in the global stoichiometry and flow conditions did not sufficiently mitigate the problem causing the significant particulate generation. This blocked the filters and flow to the gas analyzers, leading to near-zero values.

It was concluded that the nozzle either did not atomize the fuel sufficiently or that the surrounding air could not penetrate into the middle of the spray, as the “inner” flame structure in the images taken during the experiments may indicate. This was a possibility since the nozzle used produces a full cone spray pattern. Therefore, a hollow cone spray nozzle could have potentially been more effective, or ideally one of the more complex fuel injectors discussed in Section 2.1.3.

Nevertheless, the resulting exhaust temperatures under the different experimental conditions were collected, and the results are shown in Table 5.5. Temperatures were averaged over a 20 second period in post processing when the values seemed to stabilize. However, the relatively short run times of approximately 10 minutes likely resulted in values not entirely at steady state conditions contributing to the experimental error and large temperature differences observed between runs with the same configuration. This could have been furthered by changes in the radiative heat transfer to the thermocouple from the flame itself.

The effects and interactions of the fuel temperature and air mass flow rate were calculated, and the results are shown in Table 5.6. Their statistical significance was checked by comparing the signal-to-noise (SNR) t-ratio to the critical t-value using the two-tail Student's t-distribution as described in Section 3.1. This required the calculation of the pooled standard deviation, the total degrees of freedom, and the standard error, which are tabulated in Table 5.7. In these experiments, the total degrees of freedom was 4, and the 95% confidence interval was chosen, which results in a critical t-value of 2.776. Thus, the effects or interaction with SNR t-ratios greater than this critical t-value could be considered significant. From this analysis, as shown in Table 5.8, it could not be concluded that either the fuel temperature or the air mass flow rate had a statistically significant effect on the exhaust temperature.

Table 5.5: Exhaust temperature results in °C for each run of each configuration

	Coded Levels		Experimental Values				
Config.	Fuel Temp (X_1)	Air Flow (X_2)	Fuel Temp (°C)	Air Flow (SLPM)	Y [°C]		Average
1	+	+	80	1000	433.0	442.6	437.8
2	+	−	80	600	459.0	484.3	471.6
3	−	+	25	1000	418.6	416.9	417.7
4	−	−	25	600	441.0	472.5	456.7
					Pooled Average		446.0

Table 5.6: Calculated effects and interactions of the two independent variables on the exhaust temperature

	X_1	X_2	X_1X_2
$E_i\ or\ I_{ij}$	17.489	-36.422	2.595

Table 5.7: Statistical values from the exhaust temperature results

Pooled Standard Deviation (σ_P)	Total Degrees of Freedom (ν_P)	Standard Error (S_E)
14.681	4	10.381

Table 5.8: SNR t-ratios of the effects and interactions and their statistical significance on the exhaust temperature

	X_1	X_2	X_1X_2
SNR t-ratio	1.191	-2.481	0.177
Statistically significant at 95%?	NO	NO	NO

Figure 5.6 and Figure 5.7 show images of the lifted spray flame in Configuration #1 and Configuration #2, respectively. The large yellow portions of the flames indicate the presence of soot, while the smaller blue regions at the base of the flame suggest the lack of soot production. The “high” level air mass flow rate of Configuration #1 resulted in an air Reynolds number of 3150 as stated previously, suggesting turbulent conditions, which was qualitatively supported by the more unrestrained behavior and wide flame shape observed. The air Reynolds number of Configuration #2 was 1890, suggesting laminar air flow at the nozzle, which also was qualitatively supported by the more vertical and steady flame shape observed. These observations held true for Configuration #3 and Configuration #4, respectively. Additionally, there were no discernible differences between the flame shape, lifted distance, or lengths of the blue and yellow regions of the thermally enhanced fuel configurations and their counterparts as shown in Figure 5.8 and Figure 5.9. One common feature between all the configurations was the presence of what resembled an “inner” tubular structure in the middle of the flame that was more apparent in Configurations #2 and #4, but still visible in Configurations #1 and #3. As mentioned previously, this was attributed to the spray pattern of the nozzle and potentially an inadequate amount of air that diffused towards the center of the flame.

Figure 5.6: Flame images of Configuration #1

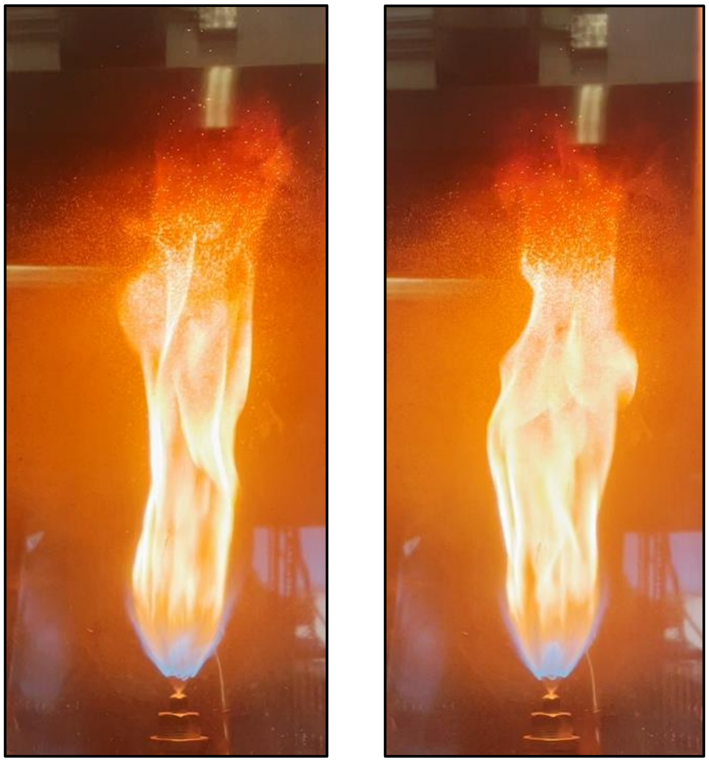

Figure 5.7: Flame images of Configuration #2

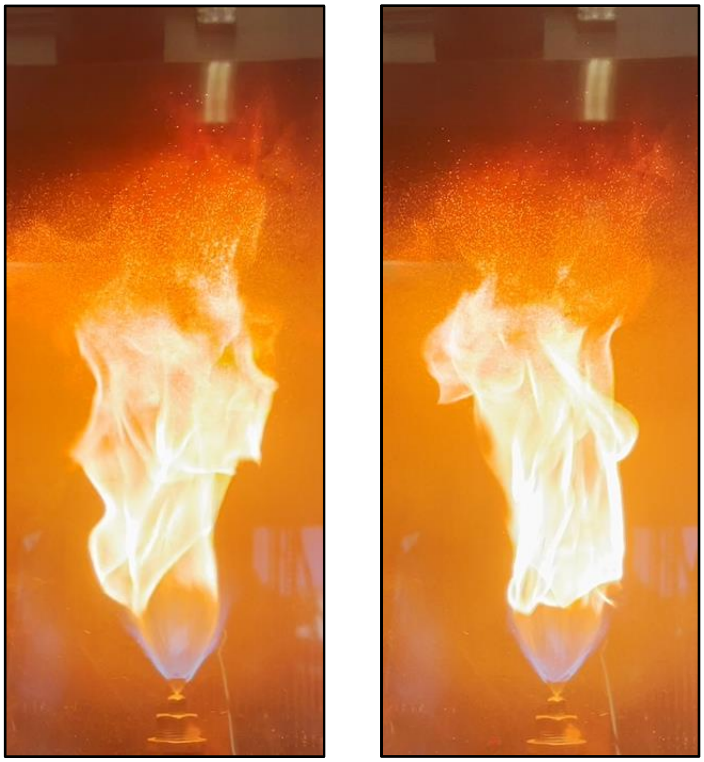

Figure 5.8: Flame images of Configuration #3

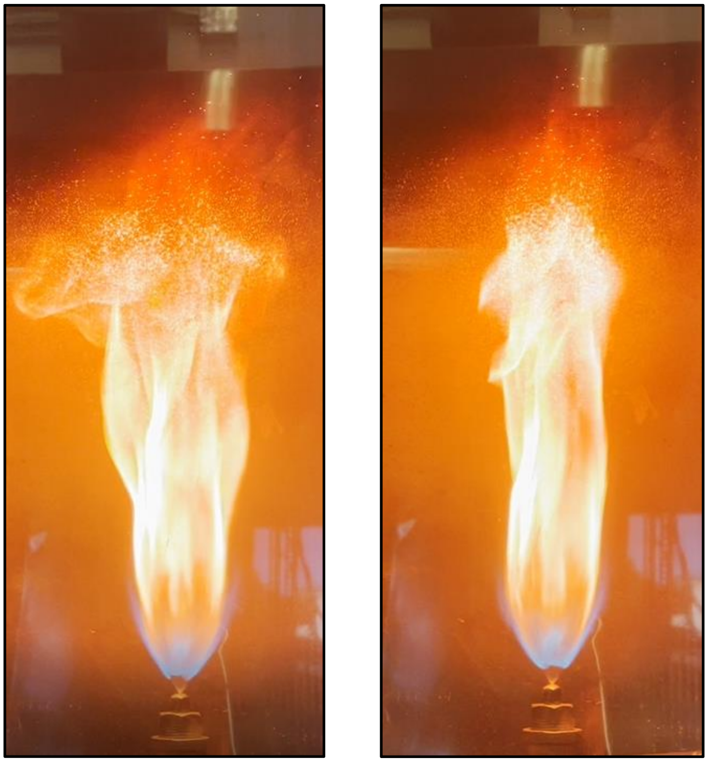

Figure 5.9: Flame images of Configuration #4

Chapter 6

Conclusions and Recommendations

6.1 Stator Heat Exchanger Experiments

A stator heat exchanger setup was investigated using a factorial design of experiments to determine the effects and interactions of three variables on the average air and average overall heat transfer coefficient. These were calculated using an energy balance and LMTD approach, respectively. It was shown that both the air flow rate and water flow rate have a statistically significant impact on the average air heat transfer coefficient. This suggests that the common Nusselt number correlations based strictly on the properties of one fluid may not be adequate to accurately predict the air heat transfer coefficient over an airfoil heat exchanger. This was likely due to the surface temperature variations caused by the change in coolant flow as noted by other researchers.

On the other hand, only the water flow rate was found to have a statistically significant effect on the average overall heat transfer coefficient, though the effect of the air flow rate, and the interaction between the two variables, were both close to being considered statistically significant at the 95% confidence interval. Nevertheless, an average overall heat transfer coefficient from all the trials was found to be 105 W/m^2-K. An effectiveness-NTU method could also have been used instead of the LMTD approach, which may have mitigated some of the errors in the system.

6.2 Stator Heat Exchanger Model

Three heat exchanger models of full-scale, multistage, fuel-intercooled, axial compressors were investigated to determine the air and fuel exit temperatures using the effectiveness-NTU method. These models used the stators in each stage of the high pressure compressor as crossflow heat exchangers with fuel as the coolant, in order to provide the benefits of the FIERA engine.

HX Model #1 used the experimentally obtained overall heat transfer coefficient in each stage as a baseline, which resulted in very low values of effectiveness, a 0.9°C decrease in compressor air exit temperature, and a 28.2°C increase in fuel exit temperature. HX Model #2 used values of overall heat transfer coefficients to achieve approximately 50% effectiveness in every compressor stage to approach a more ideal heat exchanger. This resulted in a 15.7°C decrease in compressor air exit temperature, and a 386.3°C increase in fuel exit temperature. HX Model #3 utilized Nusselt number correlations based on the fluid properties and flow conditions in the compressor to calculate the overall heat transfer coefficient for every stage. The outputs of this model resulted in a 1.8°C decrease in the compressor air exit temperature, and a 54.7°C increase in the fuel temperature, similar to HX Model #1.

These results suggest that there is not enough surface area provided by the stators to provide worthwhile intercooling. This would likely hold true for additional repurposing of components in the exhaust sections of the engine for heat recuperation. Furthermore, the low levels of heat capacity ratios found, suggest that there is insufficient fuel flow (at cruise at least) to dramatically decrease the compressor air temperature, even at the relatively high levels of effectiveness, as was shown by HX Model #2. Therefore, even if overall heat transfer coefficients of the magnitude of those used in HX Model #2 were experimentally demonstrated, the total amount of compressor intercooling still may not warrant a system redesign.

6.3 Thermally Enhanced Kerosene Combustion Experiments

The effect thermally enhanced kerosene has on combustion products and combustion characteristics was investigated using a factorial design of experiments. Results were found to be inconclusive and largely affected by the short run times and the prolific production of soot. Steps were taken to mitigate the latter with some success, such as increasing the global air-to-fuel ratio. However, this issue was considered to mainly be a local problem due to inadequate fuel atomization, suboptimal spray pattern, and insufficient air and fuel mixing. Additional air injected circumferentially towards the flame may have also enhanced mixing comparable to RQL combustors. The highly variable exhaust temperatures found could have been mitigated by longer run times, and more replications could have reduced the standard deviation and increased the signal-to-noise t-ratios for more conclusive results.

6.4 General Conclusions

This work has identified a few insights, as well as a few failings of the FIERA engine. First, it is likely that the fuel consumption at cruise is not sufficient to provide adequate heat sink potential to provide substantial compressor intercooling even if high values of heat exchanger effectiveness are achieved. Secondly, the area provided by compressor stators alone appear to be insufficient to realistically approach high effectiveness values. Lastly, cracking of the fuel would likely not take place in a solely intercooled engine unless an engine with an even higher overall pressure ratio (>60:1), or an intercooled recuperative engine was used. However, as discussed, intercooled recuperative engines perform more optimally at lower pressure ratios, so modeling the intercooling in such a configuration would have to change accordingly.

Incorporating fuel into the blades also brings to attention additional safety concerns, namely if a blade breaks from wear or engine ingestion of a foreign object, fuel flow to the combustor could be interrupted causing engine failure. Although unlikely due to the high air speeds in the compressor, this fuel could also auto ignite at “dead zones” in the elevated compressor environment causing additional damage. For all the above reasons, it is of the author’s opinion that using the fuel in a commercial turbofan engine to create a more complex thermodynamic cycle is not worthwhile.

6.5 Recommendations for Future Work

Although fuel-integrated stator heat exchangers appear to have limitations, more research can be conducted on stator heat exchangers with other coolants, which could be used in configurations similar to those investigated in the NEWAC program. [45] This would permit higher mass flow rates, which would increase the heat transfer coefficients and heat capacity rates, and ultimately increase the heat extracted from the air. The effect that multiple airfoil heat exchangers have on each other in a multiblade cascade could also be investigated. Although it should also be noted here that statistical DOE may not be the most optimal approach for further heat transfer research as discussed by Coleman and Steele [77] due to its limitations.

Another way to circumvent the small surface area available using only the stators, would be to use a fin and tube heat exchanger between two of the compressor stages using a chosen coolant. This could be similar to Reaction Engine’s precooler that has been tested for use in its hypersonic-capable Synergetic Air Breathing Rocket Engine (SABRE) concept, which uses thousands of tubes flowing cooled helium, and has been shown to cool 1,000°C air, to ambient, in a fraction of a second. [78] Such a system in a commercial turbofan engine would not need to be nearly as complex, but the same approach would hold.

Additionally, unlike a commercial turbofan engine that would like to use the heat sink capacity of the fuel only to improve engine performance, hypersonic aircraft engines require the heat sink capacity of the fuel in order to reach higher Mach numbers. Therefore, further research into the most optimal fuels to provide this capacity is still essential.

While there is a reasonably substantial amount of research on the combustion of cracked hydrocarbon fuels, there seems to be a lack of emissions research. Also due to the many fuel types and complexities of the fuel composition, both before and after thermal or catalytic cracking, a great deal more research is still needed to make better predictions about the endothermic heat sink capacity and combustion characteristics of fuels subjected to certain environmental conditions.

References

[1] StrategyR, "Commercial Aircraft - Global Market Trajectory & Analytics," Global Industry Analysts Inc., San Jose, CA, USA, 2021.

[2] Environmental Protection Agency, "Control of Air Pollution From Airplanes and Airplane Engines: GHG Emission Standards and Test Procedures," The National Archives and Records Administration, Washington, D.C., USA, 2021.

[3] R. Oxner, "U.S. Implementing 1st-Ever Airplane Emission Rules; Critics Say They're Ineffective," npr, 28 December 2020. [Online]. Available: https://www.npr.org/2020/12/28/950863508/u-s-implementing-1st-ever-airplane-emission-rules-critics-say-theyre-ineffective. [Accessed 2 October 2021].

[4] J. D. Mattingly, Elements of Propulsion: Gas Turbines and Rockets, Reston, VA, USA: American Institute of Aeronautics and Astronautics, 2006.

[5] M. P. Boyce, Gas Turbine Engineering Handbook, 4th ed., Waltham, MA, USA: Elsevier, 2012.

[6] M. J. Moran, H. N. Shapiro, D. D. Boettner and M. B. Bailey, Fundamentals of Engineering Thermodynamics, 8th ed., Hoboken, NJ, USA: Wiley, 2014.

[7] CFM International, "THE CFM56 ENGINE," Candyspace, [Online]. Available: https://www.cfmaeroengines.com/engines/cfm56/. [Accessed 25 October 2021].

[8] Pratt & Whitney, "JT8D ENGINE," Raytheon Technologies, [Online]. Available: https://prattwhitney.com/products-and-services/products/commercial-engines/jt8d. [Accessed 23 October 2021].

[9] A. F. E. Sayed, Aircraft Propulsion and Gas Turbine Engines, Boca Raton, FL, USA: Taylor and Francis Group, 2017.

[10] CFM International SA, "Type Certifiacte Data Sheet for CFM56-5B and CFM56-5C series engines," European Union Aviation Safety Agency, Paris, France, 2019.

[11] General Electric Company, "Type-Certificate Data Sheet for GE-90 Series Engines," European Union Aviation Safety Agency, Cincinnati, OH, USA, 2019.

[12] General Electric Company, "Type Certificate Data Sheet E00095EN," Federal Aviation Administration, Washington, D.C., USA, 2020.

[13] Aviation Week & Space Technology, "Gas Turbine Engines," Aviation Week Network, New York, NY, USA, 2008.

[14] S. Naik, "Basic Aspects of Gas Turbine Heat Transfer," in *Heat Exchangers - Design, Experiment and Simulation*, Rijeka, Croatia, InTech, 2017, pp. 111-144.

[15] J. R. McCusker and K. Danai, "Selection of Outputs for Gas-Turbine Engines by Parameter Signatures," in *ASME 2010 Dynamic Systems and Control Conf.*, Cambridge, MA, USA, 2010.

[16] National Academies of Sciences, Engineering, and Medicine, "Commercial Aircraft Propulsion and Energy Systems Research Reducing Global Carbon Emissions," The National Acadamies Press, Washigton, D.C., USA, 2016.

[17] R. D. Flack, Fundamentals of Jet Propulsion with Applications, New York, NY, USA: Cambridge University Press, 2005.

[18] T. P. Gabb, T. M. Smith, J. A. Nesbitt, J. Telesman, C. A. Kantzos, I. E. Locci, L. J. Evans and L. J. Ghosn, "Fatigue Failures at Defective Grains in a Single Crystal Nickel-Base Superalloy," NASA STI Program, Hampton, VA, USA, 2020.

[19] N. K. Arakere and G. R. Swanson, "Effect of Crystal Orientation on Fatigue Failure of Single Crystal Nickel Base Turbine Blade Superalloys," in *The 45th ASME Int. Gas Turbine & Aeroengine Technical Congr., Expo. and Users Symp.*, Munich, Germany, 2000.

[20] Rolls-Royce plc, The Jet Engine, 5th ed., Derby, UK: The Technical Publications Department Rolls-Royce, 1996.

[21] D. R. Clarke, M. Oechsner and a. N. P. Padture, "Thermal-barrier coatings for more efficient gas-turbine engines," *MRS Bulletin*, vol. 37, no. 10, pp. 891-898, 2012.

[22] N. P. Padture, "Advanced structural ceramics in aerospace proplusion," *Nature Materials,* vol. 15, pp. 804-809, 2016.

[23] E. Bakana, D. E. Mack, G. Mauer, R. Vaßen, J. Lamon and N. P. Padture, "High-temperature materials for power generation in gas turbines," in *Advanced Ceramics for Energy Conversion and Storage*, Amsterdam, Netherlands, Elsevier, 2020, pp. 3-62.

[24] D. Zhu, "Aerospace Ceramic Materials: Thermal, Environmental Barrier Coatings and SiC/SiC Ceramic Matrix Composites For Turbine Engine Applications," NASA STI Program, Hampton, VA, USA, 2018.

[25] J. Steibel, "Ceramic matrix composites taking flight at GE Aviation," *American Ceramic Society Bulletin,* vol. 98, no. 3, pp. 30-33, 2019.

[26] S. M. Yahya, Turbines Compressors and Fans, 4th ed., New Delhi, India: McGraw Hill, 2011.

[27] A. Mills, "Turbine Cooling," NASA Glenn Research Center, 23 July 2021. [Online]. Available: https://www1.grc.nasa.gov/historic-facilities/special-projects-laboratory/materials-research/. [Accessed 3 November 2021].

[28] D. Japikse, "The Prospects of Liquid Cooling for Turbines," in *1977 Int. Automotive Engineering Congr. and Expo.*, Detroit, MI, USA, 1977.

[29] J. G. James Van Fossen and F. S. Stepka, "Review and Status of Liquid-Cooling Technology for Gas Turbines," NASA STI Program, Cleveland, OH, USA, 1979.

[30] A. P. Fraas, "Summary of Research and Development Effort on Air and Water Cooling of Gas Turbine Blades," National Technical Information Service, Springfield, VA, USA, 1980.

[31] I. Glassman, R. A. Yetter and N. G. Glumac, Combustion, 5th ed., Waltham, MA, USA: Elsevier, 2015.

[32] Y. Liu, X. Sun, V. Sethi, D. Nalianda, Y.-G. Li and L. Wang, "Review of modern low emissions combustion technologies for aero gas turbine engines," *Process in Aerospace Sciences,* vol. 94, pp. 12-45, 2017.

[33] General Electric, "TAPS II Combustor Final Report," Federal Aviation Administration, Washington, D.C., USA, 2014.

[34] K. Ranasinghe, K. Guan, A. Gardi and R. Sabatini, "Review of advanced low-emission technologies for sustainable aviation," *Energy,* vol. 188, 2019.

[35] F. S. Shariatmadar, S. Ghanbari Pakdehi and M. A. Zarei, "An Empirical Correlation to Predict the Ignition Delay Time for Some Hydrocarbon Fuels," *Iranian Journal of Chemical Engineering,* vol. 13, no. 1, pp. 84-97, 2016.

[36] H. C. Mongia, "Engineering Aspects of Complex Gas Turbine Combustion Mixers Part V: 40 OPR," in *9th Annual Int. Energy Conversion Engineering Conf.*, San Diego, CA, USA, 2011.

[37] K. M. Tacina, "Swirl-Venturi Lean Direct Injection Combustion Technology for Low-NOx Aero Gas Turbine Engines," in *Spring Technical Meeting of the Central States Section of the Combustion Instutite*, Minneapolis, MN, USA, 2018.

[38] D. S. Crocker, D. A. Nickolaus and C. E. Smith, "Piloted airblast lean direct fuel injector". US Patent US 6,272,840 B1, 29 August 2000.

[39] R. N. Dahms and J. C. Oefelein, "Liquid jet breakup regimes at supercritical pressures," *Combustion and Flame,* vol. 162, no. 10, pp. 3648-3657, 2015.

[40] H. Müller, M. Pfitzner, J. Matheis and S. Hickel, "Large-Eddy Simulation of Coaxial LN2/GH2 Injection at Trans- and Supercritical Conditions," *Journal of Propulsion and Power,* vol. 32, no. 1, pp. 46-56, 2016.

[41] J.-P. Hickey and M. Ihme, "Supercritical mixing and combustion in rocket propulsion," *Center for Turbulence Research Annual Research Briefs 2013,* pp. 21-36, December 2013.

[42] C. Lettieri, G. Subashki and Z. Spakovszky, "Modeling Near Critical and Supercritical Fuel Injection and Mixing in Gas Turbine Applications," in *Proc. of ASME Turbomachinery Technical Conf. and Expo. 2018* , Oslo, Norway, 2018.

[43] A. W. Johnson, T. J. Held, H. C. Mongia and M. L. Vermeersch, "Combustor mixer having plasma generating nozzle". US Patent US 6,453,660 B1, 24 September 2002.

[44] K. Kyprianidis, T. Grönstedt, S. Ogaji, P. Pilidis and R. Singh, "Assessment of Future Aero-engine Designs With Intercooled and Intercooled Recuperated Cores," *Journal of engineering for gas turbines and power,* vol. 133, no. 1, pp. 01170101-01170110, 2011.

[45] ARTTIC, "NEWAC Publishable Final Activity Report," CORDIS, 2011.

[46] Z. Vlahostergios, D. Missirlis, M. Flouros, S. Donnerhack and K. Yakinthos, "Efforts to improve aero engine performance through the optimal design of heat recuperation systems targeting fuel consumption and pollutant emissions reduction," in *Proc. of 12th European Conf. on Turbomachinery Fluid dynamics & Thermodynamics*, Stockholm, Sweden, 2017.

[47] G. Hao and W. Zhan-xue, "Effects of Intercooling and Recuperation on Turbofan Engine Performance," in *Proc. of 2011 Int. Conf. on Electronic & Mechanical Engineering and Information Technology*, Harbin, China, 2011.

[48] A. Rolt and K. Kyprianidis, "Assessment of New Aero Engine Core Concepts and Technologies in the EU Framework 6 NEWAC Programme," in *ICAS 2010 Congress Proceedings, Paper No. 408,* Nice, France, 2010.

[49] Y. Ito, N. Inokura and T. Nagasaki, "Conjugate Heat Transfer in Air-to-Refrigerant Airfoil Heat Exchangers," *Journal of Heat Transfer,* vol. 136, no. 8, pp. 0817031-08170312, 2014.

[50] L.-G. Liu, X.-S. Li, X.-D. Ren, Gu and Chun-Wei, "Investigation of Cooling Effect on the Aerodynamic Performance in the Intercooled Compressor," *Journal of Propulsion and Power,* vol. 34, no. 4, pp. 920-932, 2018.

[51] S. Wong, "Conceptual Design and Preliminary Analysis of a Fuel-Integrated Energy Recuperating Aircraft Engine," M.S. Thesis, Dept. Mech. and Aero. Eng., Univ. California, Davis, 2018.

[52] G. D. Herrera, "Cycle Analysis and Heat Transfer Estimation of a Thermochemical Recuperative Turbofan Engine with Multistage Blade Intercooling," M.S. Thesis, Dept. Mech. and Aero. Eng., Univ. California, Davis, 2019.

[53] National Research Council, Evaluation of the National Aerospace Initiative, Washington, D.C.: The National Academies Press, 2004.

[54] F. Zhong, X. Fan, Y. Gong, J. Li and C.-J. Sung, "Thermal Cracking and Heat Sink Capacity of Aviation Kerosene Under Supercritical Conditions," *Journal of Thermophysics and Heat Transfer,* vol. 25, no. 3, pp. 450-456, 2011.

[55] T. Edwards, "Cracking and Deposition Behavior of Supercritical Hydrocarbon Aviation Fuels," *Combustion Science and Technology,* vol. 178, no. 1, pp. 307-334, 2006.

[56] H. Lander and A. Nixon, "Endothermic Fuels for Hypersonic Vehicles," *Journal of Aircraft,* vol. 8, no. 4, pp. 200-207, 1971.

[57] Y.-H. Yeh, C.-E. Tsai, C. Wang and R. J. Gorte, "Heat-Flow Measurements for n-Hexane Reactions on H-ZSM-5 and H(Zn)-ZSM-5: Implications for Endothermic Reforming in Hypersonic Aircraft," *Industrial Engineering Chemical Research,* vol. 56, no. 21, p. 6198–6203, 2017.

[58] S. Dinda, K. Vuchuru, S. Konda and A. N. Uttaravalli, "Heat Management in Supersonic/Hypersonic Vehicles Using Endothermic Fuel: Perspective and Challenges," *ACS Omega,* vol. 6, no. 40, pp. 26741-26755, 2021.

[59] T. Edwards and J. V. Atria, "Thermal Stability of High Temperature Fuels," in *ASME 1997 Int. Gas Turbine and Aeroengine Congr. and Exhibition*, Orlando, FL, USA, 1997.

[60] R. W. Stickles, W. J. Dodds, T. R. Koblish, J. Sager and S. Clouser, "Innovative High Temperature Aircraft Engine Fuel Nozzle Design," *Journal of Engineering for Gas Turbines and Power,* vol. 115, no. 3, p. 439–446, 1993.

[61] S. Tang, X. Luo, C. Cai, J. Wang and A. Tang, "Relationship between Coking Behavior in Hydrocarbon Fuel Pyrolysis and Surface Roughness," *Energy & Fuels,* vol. 32, no. 2, pp. 1223-1229, 2018.

[62] S. P. Heneghan, S. Zabarnick, D. R. Ballal and W. E. Harrison, "JP-8+100: The Development of High-Thermal-Stability Jet Fue," *Journal of Energy Resources Technology,* vol. 118, no. 3, pp. 170-179, 1996.

[63] M. Gao, L. Hou, X. Zhang and D. Zhang, "Coke Deposition Inhibition for Endothermic Hydrocarbon Fuels in a Reforming Catalyst-Coated Reactor," *Energy & Fuels,* vol. 33, no. 7, pp. 6126-6133, 2019.

[64] Y. Pan, H. Zhang, C. Zhang, H. Wang, K. Jing, L. Wang, X. Zhang and G. Liu, "Supercritical Pyrolysis and Coking of JP-10 in Regenerative Cooling Channels," *Energy & Fuels,* vol. 34, no. 2, pp. 1627-1638, 2020.

[65] Y. Tian, Y. Qiu, X. Hou, L. Wang and G. Liu, "Catalytic Cracking of JP-10 over HZSM-5 Nanosheets," *Energy & Fuels,* vol. 31, no. 11, pp. 11987-11994, 2017.

[66] B.-J. Zhong and H.-S. Peng, "Experimental Study on the Combustion of Thermally Cracked Endothermic Hydrocarbon Fuel," *Combustion Science and Technology,* vol. 192, no. 2, pp. 213-228, 2020.

[67] M. Colket and L. Spadaccini, "Scramjet Fuels Autoignition Study," *Journal of Propulsion and Power,* vol. 17, no. 2, p. 315–323, 2012.

[68] M. Castaldi, J. Leylegian, W. Chinitz and D. Modroukas, "Development of an Effective Endothermic Fuel Platform for Regeneratively-Cooled Hypersonic Vehicles," in *42nd AIAA/ASME/SAE/ASEE Joint Propulsion Confr. & Exhibit,* Sacremento, CA, USA, 2012.

[69] P. Puri, F. Ma, J.-Y. Choi and V. Yang, "Ignition characteristics of cracked JP-7 fuel," *Combustion and Flame,* vol. 142, no. 4, pp. 454-457, 2005.

[70] H. S. Sim, R. A. Yetter, T. L. Connell, D. M. Dabbs and I. A. Aksay, "Multifunctional Graphene-Based Additives for Enhanced Combustion of Cracked Hydrocarbon Fuels under Supercritical Conditions," *Combustion Science and Technology,* vol. 192, no. 7, pp. 1420-1435, 2020.

[71] J. S. Lawson and J. Erjavec, Modern Statistics for Engineering and Quality Improvement, Salt Lake City, UT, USA: Brooks/Cole, 2001.

[72] T. L. Bergman and A. S. Lavine, Fundamentals of Heat and Mass Transfer, 8th ed., Hoboken, NJ, USA: Wiley, 2017.

[73] M. Zielinska, M. Yavorska, M. Poreba and J. Sieniawski, "Thermal properties of cast nickel based superalloys," *Archives of Materials Science and Engineering,* vol. 44, no. 1, pp. 35-38, 2010.

[74] "Airfoil Tools," [Online]. Available: http://airfoiltools.com/plotter/index. [Accessed 5 December 2021].

[75] B. J. Cantwell, "The GE90 - An Introduction," 2 February 2010. [Online]. Available: https://web.archive.org/web/20170930084057/https://web.stanford.edu/~cantwell/AA283_Course_Material/GE90_Engine_Data.pdf. [Accessed 3 December 2021].

[76] J. Hwang, "Blowout and Emissions Characteristics Evaluation of Methane Steam Remormate Gas," Ph.D. Diss., Dept. Mech. and Aero. Eng., Univ. California, Davis, 2017.

[77] H. W. Coleman and W. G. Steele, Experimentation, Validation, and Uncertainty Analysis for Engineers, 3rd ed, Hoboken, NJ, USA: John Wiley & Sons, Inc., 2009.

[78] H. Ferguson, "Air-breathing Rocket Engine," Ingenia, September 2020. [Online]. Available: https://www.ingenia.org.uk/ingenia/issue-84/air-breathing-rocket-engine. [Accessed 28 Jan. 2022].